Evaluating the Effects of Microvia Vertical Geometry and Staggering on Signal Integrity

YIMIN WANG
MASTER´S THESIS
DEPARTMENT OF ELECTRICAL AND INFORMATION TECHNOLOGY
FACULTY OF ENGINEERING | LTH | LUND UNIVERSITY

Evaluating the Effects of Microvia Vertical Geometry and Staggering on Signal Integrity

Yimin Wang
yi0538wa-s@student.lu.se

Department of Electrical and Information Technology
Lund University

Supervisor: Daniel Sjöberg (LTH)
Muhammad Waqar Hussain (Ericsson)

Examiner: Ove Edfors

June 11, 2026

Printed in Sweden
Tryckeriet i E-huset, Lund

Abstract

Microvias are key enablers of next-generation high-speed and high-density electronic products. However, their signal-integrity performance can be affected by manufacturing-induced non-idealities, including tapered sidewalls caused by laser drilling and positional staggering caused by fabrication tolerances. This thesis investigates the impact of microvia vertical geometry and manufacturing-induced staggering on interconnects performance in multilayer Printed Circuit Board (PCB) structures.

Full-wave electromagnetic simulations are performed to compare conventional polygonal cylindrical microvia models with more realistic conical microvia models. For different transition lengths, the antipad size is first optimized in the cylindrical model to define a matched baseline design. The cylindrical and conical geometries are then compared using mixed-mode S-parameters, Time-Domain Reflectometry (TDR), Maximum Available Transmission (MAT), impedance, and isolation. In addition, manufacturing-induced microvia staggering is investigated by considering both hole misalignment and layer misalignment. Representative special cases are used to examine the effects of offset direction for hole misalignment, and the combined effects of offset direction and fan-out direction for layer misalignment. Monte Carlo simulations are then performed with Gaussian-distributed misalignment offsets to evaluate the statistical robustness of the transition.

The results show that longer and higher-frequency transitions are more sensitive to the microvia vertical geometry. The conical model leads to noticeable differences in return loss, mode conversion, TDR, impedance, and isolation prediction. For manufacturing-induced staggering, the differential-mode reflection and transmission remain relatively stable in both the representative special cases and the Monte Carlo simulations, whereas the differential-to-common-mode conversion is more sensitive to geometrical asymmetry and exhibits a wider statistical spread under Gaussian-distributed misalignment offsets.

Overall, this work provides useful guidance for microvia modeling, manufacturing-tolerance evaluation, and robust Signal Integrity (SI) design in high-speed High-Density Interconnect (HDI) PCB applications.

Keywords: Stacked microvia, differential interconnects, vertical microvia geometry, conical microvia, staggering, hole misalignment, layer misalignment, Monte Carlo analysis, SI.

Declaration

I hereby affirm that this Master thesis was composed by myself, that the work herein is my own except where explicitly stated otherwise in the text. This work has not been submitted for any other degree or professional qualification except as specified; nor has it been published. Where other peoples work has been used (either from a printed source, internet, or any other source), this has been carefully acknowledged and referenced.

AI tools, specifically ChatGPT-5, have provided assistance in making minor refinements to figures. In addition, I have used it to enhance the text by improving grammar, spelling, and style.

Acknowledgments

I would like to express my sincere gratitude to my supervisor at Lund University, Daniel Sjöberg, for his guidance, support, and valuable discussions throughout this project. I am also deeply grateful to Professor Ove Edfors for his insightful feedback in his role as examiner. Their expertise and constructive comments have been fundamental to the development of this work.

I would particularly like to thank my supervisor at Ericsson, Muhammad Waqar Hussain, whose continuous support and expert guidance were essential to the success of this project. His strong sense of responsibility, kindness, and patience were were highly valued throughout the project.

I would further like to extend my appreciation to all the teachers and teaching assistants in the LTH Wireless Communications Department. Their profound expertise, academic enthusiasm, and rigorous and meticulous approach to research and teaching have had a significant impact on me.

Finally, I would like to thank my family and friends for their unconditional love, encouragement, and support throughout my studies.

Popular Science Summary

Modern electronic products, such as computers, mobile phones, 5G devices, and AI hardware, are becoming smaller, faster, and more powerful. To make this possible, printed circuit boards need to contain many dense and high-speed electrical connections. One important structure used for this purpose is the microvia, which is a very small hole that connects different layers inside a circuit board.

Although microvias are very small, their shape and position can strongly affect how well high-speed signals travel through the board. In real manufacturing, microvias are not always perfectly shaped or perfectly aligned. For example, a microvia may have a tapered shape due to laser drilling, or its position may be slightly shifted because of manufacturing tolerances. These small imperfections can cause signal reflection, signal loss, and unwanted conversion of the useful signal into noise-like components.

This thesis studies how these manufacturing-related imperfections influence signal quality in high-speed interconnects. Computer simulations are used to compare ideal cylindrical microvias with more realistic conical microvias. The thesis also investigates two types of misalignment: hole misalignment, where the microvia position shifts, and layer misalignment, where an entire circuit-board layer is slightly displaced.

The results show that simplified microvia models can be acceptable for short connections, but more realistic models become important for long and high-frequency connections. The study also shows that some signal-quality measures remain relatively stable under small manufacturing errors, while mode conversion is more sensitive to geometrical asymmetry. These findings can help engineers build more accurate simulation models and design more reliable high-speed circuit boards.

Table of Contents

1 Introduction **1**
- 1.1 Background . . . 2
- 1.2 Objectives . . . 5
- 1.3 Thesis Outline . . . 5

2 Theoretical Framework **7**
- 2.1 Introduction . . . 7
- 2.2 Definition of Microvia . . . 7
- 2.3 Signal Propagation in Via Structures . . . 9
  - 2.3.1 Transmission-Line Model and Characteristic Impedance 9
  - 2.3.2 Differential and Common-Mode Impedance 10
- 2.4 Performance Metrics . . . 12
  - 2.4.1 Mixed-Mode S-Parameters 12
  - 2.4.2 Time-Domain Reflectometry 13
  - 2.4.3 Coupling and Isolation 15
  - 2.4.4 Maximum Available Transmission 16
  - 2.4.5 Power Balance and Loss Mechanisms 17

3 Impact of Microvia Vertical Geometry on Signal Integrity **21**
- 3.1 Introduction . . . 21
- 3.2 Simulation Structure and Key Parameters . . . 21
  - 3.2.1 Stackup Configuration 21
  - 3.2.2 Geometrical Parameters 22
  - 3.2.3 Simulation Setup and Convergence Criteria 23
  - 3.2.4 3D Model Overview 25
- 3.3 Baseline Design Optimization of the Cylindrical Microvia Transition . 26
  - 3.3.1 S-Parameter Analysis (S_{dd11}) 26
  - 3.3.2 S-Parameter Analysis (S_{dd21}) 29
  - 3.3.3 Time-Domain Reflectometry (TDR) Response 31
  - 3.3.4 Optimized Antipad Sizes for the Baseline Cylindrical Models 33
- 3.4 SI Comparison of Microvia Structures . . . 34
  - 3.4.1 Geometrical Modeling of Cylindrical and Conical Microvias 34
  - 3.4.2 Comparison of SI Performance and Simulation Efficiency 36

3.5 Impact of Microvia Geometry on Impedance 41
3.6 Impact of Microvia Geometry on Isolation 47
3.6.1 Geometric Models of Cylindrical and Conical Microvias 47
3.6.2 S-Parameter Comparison of Isolation Performance 48
3.6.3 Electric-Field Distribution and Coupling Visualization 49
3.6.4 Discussion on Geometry-Dependent Coupling Mechanisms 50
3.7 Summary 53

4 Impact of Manufacturing-Induced Staggering on Signal Integrity 55
4.1 Introduction 55
4.2 Hole Misalignment 56
4.2.1 Special Case Analysis 56
4.2.2 Monte Carlo Analysis 66
4.3 Layer Misalignment 67
4.3.1 Special case analysis 68
4.3.2 Monte Carlo Analysis 73
4.4 Summary 75

5 Conclusion and Future Work 77
5.1 Conclusions 77
5.2 Future Work 79

A Monte Carlo Results for Staggering 81

List of Acronyms

3D three-dimensional

AI Artificial Intelligence

BGA Ball Grid Array

BW Bandwidth

E-field Electric Field

HDI High-Density Interconnect

HFSS High Frequency Structure Simulator

MAG Maximum Available Gain

MAT Maximum Available Transmission

MATLAB Matrix Laboratory

PAM4 Four-Level Pulse-Amplitude Modulation

PCB Printed Circuit Board

RF Radio Frequency

S-Parameter Scattering Parameter

SI Signal Integrity

TDR Time-Domain Reflectometry

List of Figures

1.1 Cross-sectional optical microscope images of fabricated microvias reported in [13], showing representative tapered via profiles after electroplating. 3

2.1 Typical via and microvia configurations in multilayer Printed Circuit Board (PCB) structures, including through-hole vias, blind vias, buried vias, single microvias, stacked vias, and staggered vias [21]. 8

3.1 Representative 6-layer PCB stackup used for Signal Integrity (SI) analysis. 22

3.2 Key geometrical dimensions of the differential pair. 22

3.3 Illustrative possible range of S_{cd21} under different $\Delta S_{\max}$ criteria. The colored regions are obtained by applying $|S| \pm \Delta S$ in linear magnitude and then converting the results to dB, Figure layout based on HFSS help documentation [33]. 24

3.4 Differential microvia transition structures with different layer spans. . 25

3.5 The return-loss responses of the transition structures from Layer 3 to different target layers are shown for different antipad sizes. 27

3.6 The differential insertion-loss responses of the transition structures from Layer 3 to different target layers are shown for different antipad sizes. 30

3.7 The TDR impedance responses of the transition structures from Layer 3 to different target layers are shown for different antipad sizes. . . . 32

3.8 Geometric approximation of cylindrical and conical microvia structures. The microvias are modeled with 12 sides in the simulations, but are shown as hexagonal shapes here for clarity. 35

3.9 Vertical cross-sectional and three-dimensional illustrations of conical microvias with sidewall angles of $\theta = 65°$, $75°$, and $85°$. A smaller angle indicates a stronger tapering effect, while a larger angle approaches the cylindrical-via limit. 35

3.10 Three microvia geometric models used in the differential interconnect simulation from Layer 3 to Layer 15. 37

3.11 Comparison of cylindrical and conical microvia models for the L3–L15 and L3–L7 transitions. The left column shows the L3–L15 results for different conical-via configurations, while the right column shows the L3–L7 results for different cone angles. 39
3.12 Microvia transition structure and its equivalent impedance-matching model. 43
3.13 Normalized impedance Z_x on the Smith chart for the L3, L7, and L15 transitions. The solid lines denote the conical microvia models, whereas the dotted lines denote the corresponding cylindrical reference models. 44
3.14 Return loss of the transition structures from TOP Layer to different target layers: (a) Layer 3, (b) Layer 7, and (c) Layer 15. 46
3.15 Simulation model with two differential pairs for evaluating coupling between the same layer and different layers. 47
3.16 Comparison of three microvia geometry models: large cylindrical microvia, conical microvia, and small cylindrical microvia. 48
3.17 Comparison of the differential coupling for the L3–L15 transition structure using different microvia geometry models. 48
3.18 Electric-field distribution on Layer 3 when Port 3 (at Layer 3) is excited. The figure is used to evaluate the same-layer coupling from Port 3 to Port 2, corresponding to S_{32}. 51
3.19 Electric-field distribution on Layer 15 when Port 3 (at Layer 3) is excited. The figure is used to evaluate the different-layer coupling from Port 3 to Port 1, corresponding to S_{31}. 52
3.20 Estimated radiation-related loss percentage for the L3–L15 transition structure using different microvia geometry models. 53

4.1 Front-view cross sections of the x-direction hole misalignment cases. The ground layers are hidden for clarity.The dark-blue dashed lines indicate the original center positions of the stacked signal microvias from layer 3 to layer 15. The red arrows mark the hole offsets along the x-direction. 57
4.2 Top-view illustration of the x-direction hole misalignment cases on Layer 3. The red arrows indicate the hole-offset directions on this Layer, while the blue dashed arrows indicate the routing direction of the differential transmission lines that fan in to the signal microvias. . 57
4.3 Three-dimensional dimetric views of the y-direction hole misalignment cases. The ground vias and ground layers are hidden for clarity. The dark-blue solid lines show the fan-in and fan-out directions on layers 3 and 15. The green arrows mark the hole offsets along the y-direction. 60
4.4 Top-view illustration of the y-direction hole misalignment cases on Layer 3. The red arrows indicate the hole-offset directions on this Layer, while the blue dashed arrows indicate the routing direction of the differential transmission lines that fan in to the signal microvias. . 60
4.5 Simulated signal-integrity responses of the special hole-misalignment cases in the x- and y-directions. 63

4.6 Comparison of two routing configurations after the microvia layer transition. Left: opposite fan-out transition. Right: same-direction fan-out transition. 68
4.7 Three-dimensional geometrical models of the investigated layer-misalignment cases, where Same and Opp denote same-direction and opposite-direction fan-out transitions, respectively. Case 1 includes only signal-layer misalignment, while Case 2 includes staggered misalignment of both signal and ground layers, forming a zigzag-like transition. 69
4.8 Simulated signal-integrity responses of the special hole-misalignment cases in the x- and y-directions. 71

A.1 Monte Carlo distribution of the differential return loss S_{dd11} at 5, 25, and 60 GHz under hole misalignment. 82
A.2 Monte Carlo distribution of the differential insertion loss S_{dd21} at 5, 25, and 60 GHz under hole misalignment. 83
A.3 Monte Carlo distribution of the maximum achievable transmission (MAT) at 5, 25, and 60 GHz under hole misalignment. 84
A.4 Monte Carlo distribution of the differential-to-common-mode conversion coefficient S_{cd21} at 5, 25, and 60 GHz under hole misalignment. 85
A.5 Monte Carlo distribution of the differential-mode reflection coefficient S_{dd11} at 5, 25, and 60 GHz under layer misalignment for different fan-out directions. 86
A.6 Monte Carlo distribution of the differential-mode transmission coefficient S_{dd21} at 5, 25, and 60 GHz under layer misalignment for different fan-out directions. 87
A.7 Monte Carlo distribution of the maximum achievable transmission (MAT) at 5, 25, and 60 GHz under layer misalignment for different fan-out directions. 88
A.8 Monte Carlo distribution of the differential-to-common-mode conversion coefficient S_{cd21} at 5, 25, and 60 GHz under layer misalignment for different fan-out directions. 89

List of Tables

3.1 Key geometrical dimensions of the simulated structure. 23
3.2 HFSS computational cost for different microvia models. 41
3.3 Marker Information 44

Chapter 1
Introduction

With the rapid development of high-speed digital systems, signal integrity has become a critical issue in modern PCB and package design. In applications such as high-performance computing (HPC), 5G communication systems, and artificial intelligence (AI) hardware, continuously increasing data rates impose stricter requirements on interconnect performance. As signal frequencies rise, geometrical discontinuities in transmission paths may introduce impedance mismatch, signal reflection, insertion loss, and return loss, thereby degrading the overall channel quality.

To achieve compact and high-density interconnects, microvias are widely used in High-Density Interconnect (HDI) PCB technologies. Compared with conventional through-hole vias, microvias provide shorter transition paths, reduced parasitic effects, and greater routing flexibility in multilayer structures. However, due to their small dimensions and complex manufacturing processes, the electrical performance of microvias is highly sensitive to geometrical variations. Therefore, accurate modeling of microvia structures is essential for reliable signal integrity analysis.

In practical PCB manufacturing, microvias are often not perfectly cylindrical. Instead, their sidewalls may exhibit a tapered or conical profile due to laser drilling and plating processes. Nevertheless, simplified cylindrical via models are still commonly used in electromagnetic simulation to reduce modeling complexity. Such simplifications may introduce discrepancies between simulated and realistic high-frequency behavior, especially when operating at high data rates. Therefore, it is necessary to investigate whether a more realistic conical polygonal microvia model provides different signal integrity results compared with a traditional polygonal cylindrical model.

In addition to the via shape itself, manufacturing tolerances such as hole offset and layer misalignment can further affect the electrical performance of microvia-based interconnects. Misalignment between stacked or staggered microvias may change the current return path, alter the local electromagnetic field distribution, and introduce additional impedance discontinuities. These effects can become more significant at higher frequencies, where even small geometrical deviations may influence channel behavior.

This thesis investigates the impact of microvia geometrical modeling and misalignment on signal integrity performance in high-speed transmission channels.

The study focuses on comparing conical polygonal microvia models with traditional polygonal cylindrical models, and further analyzes the effects of hole offset and layer misalignment.

The analysis is conducted using full-wave electromagnetic simulation in HFSS, supported by MATLAB-based post-processing and data analysis. This combined approach enables accurate characterization of complex microvia geometries and systematic evaluation of their high-frequency characteristics. The results aim to provide useful guidance for microvia modeling, tolerance evaluation, and signal integrity optimization in high-speed HDI PCB design.

1.1 Background

With the increasing demand for high-speed and high-density electronic systems, signal integrity has become an important consideration in modern PCB and package design. Applications such as high-performance computing, 5G communication systems, artificial intelligence hardware, and mobile devices require compact interconnects that can support high data rates. In this context, HDI technology is widely used to increase routing density and reduce interconnect length [1].

Microvias are key structures in HDI PCB technology because they provide compact vertical connections between adjacent conductive layers [2]. Compared with conventional through-hole vias, microvias have smaller dimensions and shorter electrical paths, which makes them suitable for dense multilayer routing. However, their small size also makes their electrical behavior sensitive to geometrical details and fabrication tolerances [3]. At high frequencies, a microvia can no longer be regarded as an ideal vertical conductor. Instead, its diameter, pad size, antipad opening, transition length, surrounding reference planes, and nearby ground structures all contribute to the local electromagnetic field distribution and equivalent impedance [4].

For high-speed links, differential signaling is widely used because of its good noise immunity and reduced sensitivity to common external disturbances [5]. In a differential pair, the information is carried by the voltage difference between two conductors rather than by the absolute voltage of a single conductor with respect to the reference plane. Ideally, the two conductors carry signals with equal amplitude and opposite phase. Therefore, disturbances that couple similarly to both conductors mainly appear as common-mode components and can be rejected by the differential receiver. However, this advantage strongly relies on the geometrical and electrical symmetry of the differential structure. Any imbalance between the two signal paths, such as asymmetric pads, unequal via positions, nonuniform return paths, or layer-to-layer offset, may convert part of the differential-mode signal into common-mode noise [6].

Mixed-mode S-parameters are commonly used to characterize the behavior of differential interconnects [7]. In this representation, the single-ended port responses are transformed into differential-mode and common-mode quantities. The differential-mode reflection coefficient S_{dd11} describes the impedance matching of the input differential port, while the differential-mode transmission coefficient

S_{dd21} describes the desired signal transfer from the input differential port to the output differential port. In addition, the mode-conversion term S_{cd21} represents the conversion from the input differential mode to the output common mode. A larger S_{cd21} generally indicates stronger imbalance in the interconnect structure and may lead to increased common-mode radiation, electromagnetic interference, or degradation of the differential signal quality [8]. Therefore, mixed-mode S-parameters provide an effective way to evaluate both the differential-mode performance and the structural symmetry of microvia transitions.

The signal-integrity behavior of via and microvia transitions is strongly affected by their geometrical parameters [9]. For example, the vertical transition length influences the inductive behavior and the overall discontinuity of the interconnect. The pad and antipad dimensions affect the local capacitance around the via. The placement of nearby ground vias and reference-plane openings influences the return-current path and the coupling between adjacent structures. In differential via transitions, the relative position between the two signal vias is also important because it determines the balance of the differential pair and the degree of electromagnetic coupling. As a result, even small geometrical changes may cause variations in return loss, insertion loss, time-domain impedance, and mode conversion [10].

In many electromagnetic simulations, microvias are simplified as cylindrical structures. This approximation can reduce modeling complexity and simulation cost. However, practical laser-drilled microvias are often not perfectly cylindrical. Due to the laser drilling and plating processes, the microvia sidewall may exhibit a tapered profile, and the actual structure is closer to a truncated cone [11, 12]. Such fabricated microvia profiles have been observed in cross-sectional measurements reported in previous studies [13], as shown in Fig. 1.1.

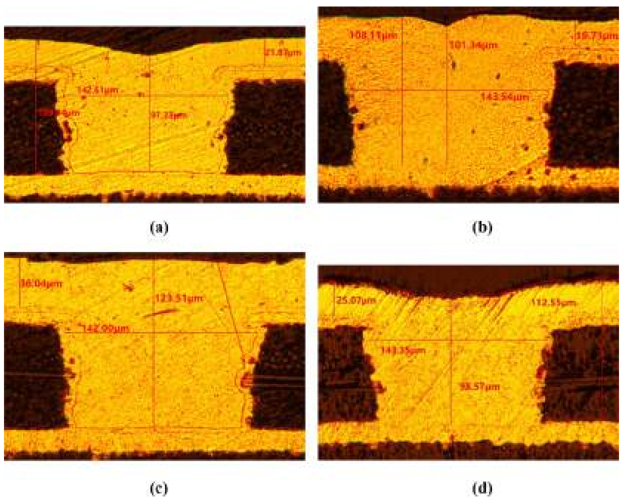

Figure 1.1: Cross-sectional optical microscope images of fabricated microvias reported in [13], showing representative tapered via profiles after electroplating.

The difference between a cylindrical and a conical microvia changes the metal distribution along the vertical direction and may modify the equivalent capacitance, inductance, and local impedance of the transition. Therefore, it is necessary to evaluate whether the simplified cylindrical model can accurately represent the high-frequency behavior of practical microvia transitions [3].

In addition to the vertical geometry of the microvia, manufacturing tolerances may also introduce positional errors [14]. Hole misalignment can occur when the drilled microvia position deviates from its nominal location. In a differential microvia transition, such hole-position errors may change the spacing between the two signal vias and disturb the symmetry of the differential pair. If the two signal vias are shifted in different directions or by different amounts, the two conductors may experience different parasitic capacitances and inductances. This imbalance can introduce impedance discontinuity and increase differential-to-common mode conversion. Therefore, hole misalignment is an important fabrication non-ideality to consider when evaluating the robustness of high-speed differential microvia transitions [15].

Layer misalignment is another important source of geometrical deviation in multilayer HDI PCB. Unlike hole misalignment, which mainly describes the deviation of the drilled microvia hole, layer misalignment refers to the relative displacement between different PCB layers during fabrication or lamination. When a layer is shifted from its nominal position, the signal pads, traces, ground structures, antipads, and reference-plane openings on that layer may also be displaced. Therefore, layer misalignment can change not only the electrical connection of the stacked microvias, but also the surrounding copper distribution and return-current path. In stacked microvia transitions, such layer-to-layer offsets may produce staggered structures, which can further modify the local electromagnetic field distribution and increase the imbalance of the differential transition [16].

Compared with deterministic geometry variations, manufacturing-induced misalignment in practical fabrication often contains statistical uncertainty [17]. One single worst-case or single-direction offset may not fully represent the overall behavior of the structure. Therefore, Monte Carlo analysis is useful for evaluating the sensitivity and robustness of microvia transitions under fabrication tolerances. By sampling possible hole or layer offsets according to a prescribed distribution, the distribution, mean value, and variation range of signal-integrity metrics can be obtained. This makes it possible to determine whether the structure is highly sensitive to fabrication errors and whether certain geometrical configurations provide better tolerance to misalignment [18].

Previous studies and design guidelines have discussed the importance of microvias in HDI PCB design [1, 2, 3], the fabrication characteristics of laser-drilled microvias [12, 11, 13], and the signal-integrity issues associated with via transitions [4, 10, 18]. However, a systematic comparison between cylindrical and conical microvia models, together with a statistical evaluation of hole and layer misalignment, is still needed for high-frequency differential microvia transitions. In particular, the combined influence of realistic vertical microvia profiles and manufacturing-induced staggering on mixed-mode S-parameters, TDR, and differential-to-common mode conversion has not been fully quantified. Therefore, this thesis investigates the impact of microvia vertical geometry and manufacturing-induced staggering on signal integrity using full-wave electromagnetic simulation and Monte Carlo analysis.

1.2 Objectives

The main objective of this thesis is to investigate how microvia vertical geometry and manufacturing-induced staggering affect the signal integrity and high-frequency electrical performance of microvia transitions. The specific objectives are:

- to establish full-wave simulation models for differential microvia transitions in multilayer PCB structures;
- to compare conventional polygonal cylindrical microvia models with more realistic conical microvia models;
- to evaluate the influence of transition length and microvia geometry on return loss, insertion loss, TDR, impedance, mode conversion and isolation;
- to analyze the impact of hole misalignment and layer misalignment on differential microvia transitions;
- to use Monte Carlo analysis to evaluate the tatistical influence of random manufacturing tolerances;
- to provide practical guidance for microvia modeling and robust signal-integrity design in high-speed HDI PCB interconnects.

1.3 Thesis Outline

This thesis is organized as follows:

Chapter 2 introduces the theoretical background of vias, microvias, transmission-line behavior, and the signal-integrity metrics used throughout this thesis, including mixed-mode S-parameters, TDR, isolation, MAT, and power-balance-based loss estimation.

Chapter 3 investigates the impact of microvia vertical geometry on signal integrity. After introducing the simulation model and key parameters, the conventional cylindrical microvia model is first analyzed under different antipad sizes and transition lengths, in order to identify suitable baseline dimensions for the subsequent comparisons. The chapter then compares the conventional cylindrical model with the more realistic conical microvia model in terms of return loss, insertion loss, mode conversion, TDR, impedance, and isolation performance.

Chapter 4 analyzes the influence of manufacturing-induced staggering on the signal integrity of differential microvia transitions. Two types of misalignment are considered: hole misalignment and layer misalignment. For each type, special cases are first studied to explain the physical effects of specific offset directions and geometrical asymmetries. Monte Carlo analysis is then used to evaluate the statistical influence of random manufacturing tolerances on the signal-integrity performance.

Chapter 5 concludes the thesis by summarizing the main findings and outlining future research directions, including experimental validation and more detailed modeling of manufacturing-induced microvia variations.

Appendix A provides additional Monte Carlo results for hole misalignment and layer misalignment. These results support the statistical analysis presented in Chapter 4.

Chapter 2

Theoretical Framework

2.1 Introduction

This chapter introduces the theoretical background required for analyzing the signal-integrity behavior of microvia-based differential interconnects. Since the main focus of this thesis is the influence of microvia vertical geometry and manufacturing-induced staggering, the chapter first reviews the basic concept, classification, and key geometrical parameters of microvias. These definitions provide the basis for understanding why practical microvia structures may deviate from ideal cylindrical models and why stacked microvia transitions are sensitive to fabrication tolerances.

The chapter then reviews the transmission-line representation of high-speed interconnects and introduces the characteristic impedance concept, which is used to interpret impedance mismatch and reflection in via-transition structures. Based on this framework, several signal-integrity metrics are defined, including S-parameters, mixed-mode S-parameters, TDR impedance, coupling and isolation, maximum available transmission (MAT), and power-balance-based loss estimation. These quantities are used throughout the following chapters to evaluate and compare the effects of microvia geometry, transition length, hole misalignment, and layer misalignment.

2.2 Definition of Microvia

A microvia is a small via structure used in HDI PCB to provide electrical interconnection between conductive layers, enabling compact routing and high interconnect density [19, 20]. Compared with conventional mechanically drilled through-holes, microvias have a much smaller diameter and are typically fabricated using laser drilling followed by copper plating or copper filling processes. Due to their reduced size and shorter electrical path, microvias enable higher routing density, improved signal transmission performance, and more compact electronic packaging. As a result, they are widely adopted in advanced electronic products such as smartphones, wearable devices, automotive electronics, and high-speed computing systems.

Based on different classification criteria, via structures in multilayer PCB can

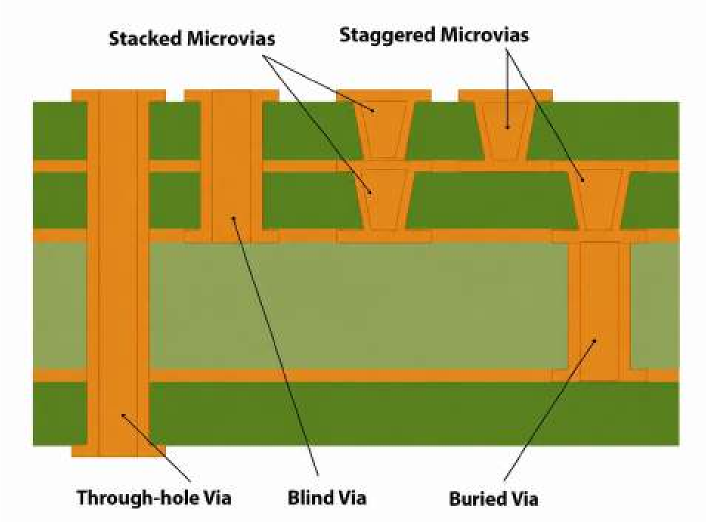

Figure 2.1: Typical via and microvia configurations in multilayer PCB structures, including through-hole vias, blind vias, buried vias, single microvias, stacked vias, and staggered vias [21].

be divided into several categories. From the perspective of vertical interconnection configuration, common types include through-hole vias, blind vias, buried vias, single microvias, stacked vias, and staggered vias, as illustrated in Fig. 2.1.

- **Through-hole via** refers to a via that passes through the entire PCB stackup and connects the top layer to the bottom layer. It is commonly formed by mechanical drilling and is widely used in conventional multilayer PCB designs.
- **Blind via** connects an outer layer to one or more inner layers without passing through the entire PCB. Since a microvia is usually a laser-drilled blind via, blind vias are particularly important in HDI interconnect structures.
- **Buried via** connects two or more inner layers and is not visible from the outer surfaces of the PCB. It can improve routing density, but it usually increases fabrication complexity and cost.
- **Single microvia** refers to a single microvia connecting two adjacent layers only. It is the simplest microvia structure and is commonly used for short vertical interconnections in HDI PCB.
- **Stacked microvia** consists of two or more microvias vertically aligned on top of each other to connect multiple layers in a compact area. This structure is highly effective for increasing interconnection density.
- **Staggered microvia** is formed by offsetting adjacent microvias rather than placing them directly above one another. This arrangement can reduce stress concentration and often improves reliability.

In practical fabrication, the geometry of a microvia is not always an ideal cylinder. Laser drilling and subsequent copper plating may produce a tapered sidewall profile, so that the diameter near the entrance of the microvia differs from that near the bottom. As a result, the fabricated microvia can often be better approximated by a truncated-conical shape rather than by a perfect cylindrical shape. This geometrical difference changes the local distribution of capacitance and inductance around the via transition and may therefore affect impedance matching, reflection, and coupling at high frequencies.

Among these structures, the stacked microvia is widely used in practical HDI PCB designs where multi-layer interconnection must be achieved within limited board space. Its vertically aligned configuration enables compact routing and efficient layer transitions, making it a common solution in advanced industrial products. However, the vertical arrangement of stacked microvias may also introduce electrical discontinuities and parasitic effects that influence impedance continuity, signal reflection, insertion loss, and crosstalk, particularly at high frequencies.

In this thesis, the stacked microvia structure is selected as the main object of study because it is used in the considered industrial interconnect design. The purpose is therefore not to compare different microvia categories, but to examine how the selected stacked transition is affected by two practical non-idealities: the vertical geometry of the microvia and manufacturing-induced positional staggering. In particular, the later chapters compare cylindrical and conical microvia models and investigate the effects of hole misalignment and layer misalignment on the signal-integrity performance of the differential transition.

2.3 Signal Propagation in Via Structures

2.3.1 Transmission-Line Model and Characteristic Impedance

High-speed interconnects in PCB can be described using a transmission-line model when the signal wavelength becomes comparable to the physical length of the interconnect structure [22]. In this model, the electrical behavior of the line is characterized by its per-unit-length resistance R, inductance L, conductance G, and capacitance C. These distributed parameters determine how voltage and current waves propagate along the interconnect and provide a useful basis for analyzing impedance discontinuities, reflections, and signal degradation.

For a uniform transmission line, the voltage and current can be expressed as the superposition of forward- and backward-propagating waves. Considering the forward-propagating components, the phasor-domain voltage and current are given by

$$V(z) = V_0^+ e^{-\gamma z}, \tag{2.1}$$

$$I(z) = I_0^+ e^{-\gamma z}, \tag{2.2}$$

where $V(z)$ and $I(z)$ denote the voltage and current phasors at position z, respectively. The quantities V_0^+ and I_0^+ are the amplitudes of the forward-propagating voltage and current waves at the reference position $z = 0$.

The superscript "+" indicates propagation in the positive z-direction. The complex propagation constant is denoted by γ, and can be written as

$$\gamma = \alpha + \mathrm{j}\beta, \tag{2.3}$$

where α is the attenuation constant, β is the phase constant, and j is the imaginary unit.

Substituting these expressions into the telegrapher's equations gives the characteristic impedance of the line as

$$Z_0 = \frac{V_0^+}{I_0^+} = \sqrt{\frac{R + \mathrm{j}\omega L}{G + \mathrm{j}\omega C}}. \tag{2.4}$$

For a lossless transmission line, where $R = 0$ and $G = 0$, the characteristic impedance reduces to

$$Z_0 = \sqrt{\frac{L}{C}}. \tag{2.5}$$

This shows that the characteristic impedance is mainly determined by the inductive and capacitive properties of the interconnect geometry [22].

In practical PCB interconnects, discontinuities such as vias, microvias, pads, anti-pads, and layer transitions locally change the effective inductance and capacitance of the signal path. As a result, the local characteristic impedance deviates from the nominal value of the transmission line. This impedance mismatch causes part of the incident signal to be reflected, which degrades the return loss and may also affect insertion loss and crosstalk. Therefore, maintaining a smooth impedance transition is essential for high-speed SI performance. In this thesis, the characteristic impedance concept provides the theoretical basis for analyzing how microvia geometry, vertical transition length, and manufacturing misalignment influence the electromagnetic response of multilayer interconnect structures.

2.3.2 Differential and Common-Mode Impedance

Differential and common-mode quantities are commonly used to describe balanced interconnects and mixed-mode S-parameters [23, 24].

The simplest case of a differential pair is obtained when the two signal lines are sufficiently separated so that the coupling between them can be neglected. In this case, each line can be treated as an independent single-ended transmission line with characteristic impedance Z_0.

For one signal line, the current I_{one} flowing into the signal conductor and returning through the reference path is

$$I_{\mathrm{one}} = \frac{V_{\mathrm{one}}}{Z_0}, \tag{2.6}$$

where V_{one} is the voltage between one signal line and its reference path.

For an ideal differential signal, the two conductors carry equal-amplitude and opposite-polarity voltages V_{p} and V_{n}. Therefore, the differential voltage between the two signal lines is

$$V_{\text{diff}} = V_{\text{p}} - V_{\text{n}} = 2V_{\text{one}}. \tag{2.7}$$

The differential impedance is defined as the impedance seen by the differential signal:

$$Z_{\text{diff}} = \frac{V_{\text{diff}}}{I_{\text{one}}} = \frac{2V_{\text{one}}}{I_{\text{one}}} = 2Z_0. \tag{2.8}$$

Thus, for an uncoupled differential pair, the differential impedance is twice the single-ended characteristic impedance of either line.

In addition to the differential mode, the same pair of conductors can also support a common-mode signal. In the common mode, the two conductors carry equal-amplitude and same-polarity voltages with respect to the reference path. The common-mode voltage can be defined as

$$V_{\text{comm}} = \frac{V_{\text{p}} + V_{\text{n}}}{2}. \tag{2.9}$$

For a pure common-mode signal, the two line voltages are equal:

$$V_{\text{p}} = V_{\text{n}} = V_{\text{comm}}. \tag{2.10}$$

Since the two lines are uncoupled in this simplified case, each line carries the same single-ended current

$$I_{\text{one}} = \frac{V_{\text{comm}}}{Z_0}. \tag{2.11}$$

The total common-mode current is the sum of the currents on the two conductors:

$$I_{\text{comm}} = I_{\text{p}} + I_{\text{n}} = 2I_{\text{one}}. \tag{2.12}$$

Therefore, the common-mode impedance seen by the pair is

$$Z_{\text{comm}} = \frac{V_{\text{comm}}}{I_{\text{comm}}} = \frac{V_{\text{comm}}}{2I_{\text{one}}} = \frac{Z_0}{2}. \tag{2.13}$$

Thus, in the uncoupled case, the differential and common-mode impedances are

$$Z_{\text{diff}} = 2Z_0, \qquad Z_{\text{comm}} = \frac{Z_0}{2}. \tag{2.14}$$

In practical differential pairs, however, the two conductors are usually close enough to introduce electromagnetic coupling. In that case, the differential mode is related to the odd-mode impedance, while the common mode is related to the even-mode impedance [24]:

$$Z_{\text{diff}} = 2Z_{\text{odd}}, \qquad Z_{\text{comm}} = \frac{Z_{\text{even}}}{2}. \tag{2.15}$$

The uncoupled results are recovered when the coupling between the two conductors is negligible, for which

$$Z_{\text{odd}} = Z_{\text{even}} = Z_0. \tag{2.16}$$

These impedance definitions are important for understanding the signal-integrity behavior of differential microvia transitions. Ideally, a differential interconnect should maintain a stable differential impedance along the signal path. Any discontinuity caused by the microvia geometry, transition length, antipad structure, or manufacturing misalignment may introduce local impedance deviations. These deviations can lead to reflections and degrade the differential signal transmission. In addition, structural asymmetry can convert part of the differential-mode signal into common-mode energy, which may increase radiation and unwanted coupling to nearby structures [6].

2.4 Performance Metrics

2.4.1 Mixed-Mode S-Parameters

The mixed-mode S-parameter formulation introduced in this section is mainly based on the standard single-ended to mixed-mode conversion reported in [23, 24, 25].

For a differential interconnect, the electromagnetic response can be described either in terms of conventional single-ended ports or in terms of differential- and common-mode ports. The single-ended four-port scattering relation is first written as

$$\begin{bmatrix} b_1 \\ b_2 \\ b_3 \\ b_4 \end{bmatrix} = \underbrace{\begin{bmatrix} S_{11} & S_{12} & S_{13} & S_{14} \\ S_{21} & S_{22} & S_{23} & S_{24} \\ S_{31} & S_{32} & S_{33} & S_{34} \\ S_{41} & S_{42} & S_{43} & S_{44} \end{bmatrix}}_{[S_{se}]} \begin{bmatrix} a_1 \\ a_2 \\ a_3 \\ a_4 \end{bmatrix}, \tag{2.17}$$

where a_i and b_i denote the incident and reflected power waves at the i-th single-ended port, respectively. Although this representation is directly related to the physical ports of the structure, it does not explicitly separate the differential and common-mode responses of a differential pair.

To describe the behavior of the structure under differential excitation more directly, the single-ended port quantities can be transformed into mixed-mode quantities. The corresponding mixed-mode scattering relation is expressed as

$$\begin{bmatrix} b_{d1} \\ b_{d2} \\ b_{c1} \\ b_{c2} \end{bmatrix} = \underbrace{\left[\begin{array}{cc:cc} S_{dd11} & S_{dd12} & S_{dc11} & S_{dc12} \\ S_{dd21} & S_{dd22} & S_{dc21} & S_{dc22} \\ \hdashline S_{cd11} & S_{cd12} & S_{cc11} & S_{cc12} \\ S_{cd21} & S_{cd22} & S_{cc21} & S_{cc22} \end{array}\right]}_{[S_{mm}]} \begin{bmatrix} a_{d1} \\ a_{d2} \\ a_{c1} \\ a_{c2} \end{bmatrix}. \tag{2.18}$$

Here, the subscripts d and c denote differential mode and common mode, respectively. The sub-matrices S_{dd} and S_{cc} describe the pure differential-mode and pure common-mode responses, while S_{dc} and S_{cd} describe the mode-conversion behavior between the two modes. For example, S_{dd21} represents the differential-mode transmission coefficient, whereas S_{cd21} represents the conversion from differential-mode excitation to common-mode output.

Under the ideal mixed-mode transformation, the single-ended and mixed-mode S-parameter matrices are related by

$$[S_{mm}] = [M]\,[S_{se}]\,[M]^{-1}\,, \tag{2.19}$$

where $[S_{se}]$ and $[S_{mm}]$ are the single-ended and mixed-mode scattering matrices, respectively. The transformation matrix $[M]$ is given by

$$[M] = \frac{1}{\sqrt{2}}\begin{bmatrix} 1 & -1 & 0 & 0 \\ 0 & 0 & 1 & -1 \\ 1 & 1 & 0 & 0 \\ 0 & 0 & 1 & 1 \end{bmatrix}. \tag{2.20}$$

This matrix combines the two conductors of each differential pair into their odd-mode and even-mode components, which correspond to differential-mode and common-mode quantities, respectively [25].

2.4.2 Time-Domain Reflectometry

The theoretical background of Time-Domain Reflectometry (TDR) presented in this section, including the basic operating principle, its connection to frequency-domain S-parameters, and the resolution limitation caused by finite rise time and bandwidth, is summarized based on [26, 27, 28, 29, 30].

TDR is commonly used to evaluate the impedance profile of high-speed interconnects. In a TDR analysis, a fast step signal is launched into the interconnect, and the reflected waveform is observed in the time domain. The time-domain TDR excitation and its frequency-domain representation form a Fourier transform pair,

$$u_r(t) \iff U_r(\omega),$$

where $u_r(t)$ denotes the incident step waveform in the time domain, and $U_r(\omega)$ denotes its corresponding frequency spectrum.

Since impedance discontinuities generate reflected waves, the TDR response can be used to identify local impedance variations along the signal path. The time-domain reflection coefficient is defined as

$$\rho(t) = \frac{V^-(t)}{V^+(t)}, \tag{2.21}$$

where $V^+(t)$ and $V^-(t)$ denote the incident and reflected voltage waves, respectively. The corresponding TDR impedance is given by

$$Z_{\mathrm{TDR}}(t) = Z_0\frac{1+\rho(t)}{1-\rho(t)}, \tag{2.22}$$

where Z_0 is the reference impedance of the transmission line [28].

Based on the reflection coefficient

$$\rho(t) = \frac{Z_{\mathrm{TDR}}(t) - Z_0}{Z_{\mathrm{TDR}}(t) + Z_0}, \tag{2.23}$$

the sign of $\rho(t)$ indicates whether the local impedance is higher or lower than the reference impedance Z_0. A negative reflection coefficient, $\rho(t) < 0$, corresponds to $Z_{\mathrm{TDR}}(t) < Z_0$, which is usually associated with a capacitive discontinuity. In contrast, a positive reflection coefficient, $\rho(t) > 0$, corresponds to $Z_{\mathrm{TDR}}(t) > Z_0$, which is usually associated with an inductive discontinuity [30].

In the HFSS post-processing used in this work, the TDR response is obtained from the frequency-domain S-parameters through an inverse Fourier-transform operation. For the differential-mode response, the frequency-domain reflection coefficient is given by

$$\Gamma_{\mathrm{d}}(\omega) = S_{\mathrm{dd11}}(\omega). \tag{2.24}$$

The corresponding time-domain reflection response can be expressed as

$$h_{\Gamma,\mathrm{d}}(t) = \mathcal{F}^{-1}\left\{S_{\mathrm{dd11}}(\omega)\right\}. \tag{2.25}$$

For a step-like TDR excitation with finite rise time, the differential time-domain reflection coefficient can be written as

$$\rho_{\mathrm{d}}(t) = \mathcal{F}^{-1}\left\{S_{\mathrm{dd11}}(\omega) U_{\mathrm{r}}(\omega)\right\}, \tag{2.26}$$

where $U_{\mathrm{r}}(\omega)$ denotes the spectrum of the band-limited step signal used in the TDR calculation.

The differential TDR impedance is then expressed as

$$Z_{\mathrm{diff,TDR}}(t) = Z_{\mathrm{diff},0} \frac{1 + \rho_{\mathrm{d}}(t)}{1 - \rho_{\mathrm{d}}(t)}, \tag{2.27}$$

where $Z_{\mathrm{diff},0}$ is the differential reference impedance and $\rho_{\mathrm{d}}(t)$ is the differential-mode reflection coefficient in the time domain. In this thesis, the target differential impedance of the interconnect is 85 Ω, and the differential TDR response is evaluated using $Z_{\mathrm{diff},0} = 85\ \Omega$ as the reference impedance.

For a transmission line with propagation velocity v_{p}, the distance corresponding to a measured round-trip time delay t is

$$d = \frac{v_{\mathrm{p}} t}{2}, \tag{2.28}$$

where the factor of two accounts for the forward and reflected propagation paths. The propagation velocity can be approximated as

$$v_{\mathrm{p}} = \frac{c}{\sqrt{\varepsilon_{\mathrm{eff}}}}, \tag{2.29}$$

where c is the speed of light in vacuum and $\varepsilon_{\mathrm{eff}}$ is the effective dielectric constant. Therefore, the spatial resolution of the TDR response can be estimated as [26]

$$\Delta d \approx \frac{v_{\mathrm{p}} t_{\mathrm{r}}}{2} = \frac{c t_{\mathrm{r}}}{2\sqrt{\varepsilon_{\mathrm{eff}}}}, \tag{2.30}$$

where t_r is the rise time of the TDR step signal.

The spatial resolution of the TDR response is limited by the signal rise time and the available frequency bandwidth. A shorter rise time improves the time-domain resolution, but it also requires a sufficiently large bandwidth in the frequency-domain simulation. For a single-pole or approximately Gaussian system response, the 10–90% rise time is commonly approximated by

$$t_\mathrm{r} \approx \frac{0.35}{BW}, \tag{2.31}$$

where t_r is the signal rise time and BW denotes the available bandwidth [29]. Therefore, specifying an unrealistically short rise time without extending the frequency sweep to provide the corresponding bandwidth may introduce unreliable time-domain details or ringing artifacts.

The HFSS frequency sweep and TDR post-processing settings used in this work are as follows. The frequency sweep is performed from 0 to 60 GHz with 1201 points, and the TDR calculation uses a signal rise time of 16.667 ps.

For a typical PCB dielectric with relative permittivity $D_k \approx 3.5$, the effective dielectric constant of the transmission-line mode is approximated as $\varepsilon_\mathrm{eff} \approx D_k$. Therefore, the propagation velocity is approximately

$$v_\mathrm{p} = \frac{c}{\sqrt{D_k}} \approx 1.6 \times 10^8 \ \mathrm{m/s}. \tag{2.32}$$

With $t_\mathrm{r} = 16.667$ ps, this gives

$$\Delta d \approx \frac{1.6 \times 10^8 \times 16.667 \times 10^{-12}}{2} \approx 1.33 \ \mathrm{mm}. \tag{2.33}$$

This length scale is comparable to the stack thickness and is much larger than the dimensions of individual microvia features. Therefore, the TDR time-domain features in this work should not be assigned to a specific pad, layer, or microvia section. Instead, they should be interpreted as the combined response of the local transition region within the effective TDR resolution. In addition, the time origin depends on the port reference plane or de-embedding setting, and the effective propagation velocity may vary in different parts of the interconnect. Consequently, the TDR response in this thesis is used mainly as a qualitative and comparative metric.

2.4.3 Coupling and Isolation

In high-speed interconnects, electromagnetic coupling between adjacent signal paths is an important signal-integrity concern. When a signal propagates along one channel, part of its electromagnetic field may couple to a neighboring channel. This unwanted signal leakage is commonly referred to as crosstalk or coupling.

In the frequency domain, coupling between two ports can be described using the corresponding transmission S-parameter. For example, if port j is excited and the coupled response is observed at port i, the coupling coefficient is given by

$$S_{ij} = \left. \frac{b_i}{a_j} \right|_{a_k=0,\ k\neq j}. \tag{2.34}$$

When expressed in decibels, the coupling level is

$$S_{ij,\mathrm{dB}} = 20\log_{10}|S_{ij}|. \tag{2.35}$$

A smaller magnitude, or a more negative value in dB, indicates weaker coupling between the two ports.

Isolation describes how well two channels are separated from each other. It is often defined as the negative of the coupling level in decibels:

$$\mathrm{Isolation}_{ij} = -20\log_{10}|S_{ij}|. \tag{2.36}$$

Therefore, a larger isolation value corresponds to weaker coupling and better electromagnetic separation between channels.

2.4.4 Maximum Available Transmission

Based on the mixed-mode S-parameter formulation introduced above, a derived figure of merit, denoted as maximum available transmission (MAT), is used in this thesis to evaluate the overall transmission capability of the differential interconnect. The definition is inspired by the maximum available gain (MAG) used in two-port amplifier analysis [31]. However, since the structures investigated in this work are passive interconnects rather than active devices, the metric is interpreted as a transmission-oriented quantity rather than an actual power gain.

For the differential-mode two-port network, the determinant of the differential-mode scattering matrix is defined as

$$\Delta_\mathrm{D} = S_{\mathrm{dd}11}S_{\mathrm{dd}22} - S_{\mathrm{dd}12}S_{\mathrm{dd}21}. \tag{2.37}$$

The corresponding stability-like factor is written as

$$K_\mathrm{D} = \frac{1 - |S_{\mathrm{dd}11}|^2 - |S_{\mathrm{dd}22}|^2 + |\Delta_\mathrm{D}|^2}{2\,|S_{\mathrm{dd}12}S_{\mathrm{dd}21}|}. \tag{2.38}$$

Following the form of MAG, the maximum available transmission is then defined as

$$\mathrm{MAT} = \left|\frac{S_{\mathrm{dd}21}}{S_{\mathrm{dd}12}}\right|\left(K_\mathrm{D} - \sqrt{K_\mathrm{D}^2 - 1}\right). \tag{2.39}$$

The MAT is a dimensionless quantity. In this thesis, it is expressed in decibels as

$$\mathrm{MAT}_\mathrm{dB} = 10\log_{10}(\mathrm{MAT}). \tag{2.40}$$

Compared with directly observing $S_{\mathrm{dd}21}$, MAT reduces the influence of input and output mismatch by evaluating the maximum available transmission under conjugate matching conditions. Therefore, it provides a useful metric for examining the insertion-loss behavior of the differential signal path with the mismatch contribution separated from the measured transmission coefficient. In this work, MAT is mainly used to compare different microvia geometries and manufacturing misalignment cases. A higher MAT value indicates lower mismatch-corrected insertion loss, while a lower MAT value suggests stronger intrinsic degradation of the differential transmission path.

2.4.5 Power Balance and Loss Mechanisms

For a differential via transition, the incident differential-mode power is not only transmitted to the output differential port, but can also be reflected, converted into common-mode power, dissipated in the conductors and dielectrics, or leaked into the surrounding PCB cavity. Therefore, the reduction of the differential transmission coefficient S_{dd21} cannot be interpreted solely as material loss. A power-balance description based on mixed-mode S-parameters is needed to separate the different physical mechanisms contributing to the degradation of the differential signal [25].

When a differential-mode wave is incident at port 1, the input power can be divided into the reflected differential-mode power, the transmitted differential-mode power, the mode-converted common-mode power, and the remaining loss. This relationship can be written as

$$P_{\text{in},dd} = P^{(1)}_{\text{ref},dd} + P^{(2)}_{\text{out},dd} + P^{(1)}_{\text{ref},cd} + P^{(2)}_{\text{out},cd} + P_{\text{loss}}, \tag{2.41}$$

where $P_{\text{in},dd}$ is the incident differential-mode power. The terms $P^{(1)}_{\text{ref},dd}$ and $P^{(2)}_{\text{out},dd}$ denote the differential-mode reflected power at port 1 and the differential-mode transmitted power at port 2, respectively. The terms $P^{(1)}_{\text{ref},cd}$ and $P^{(2)}_{\text{out},cd}$ represent the common-mode power generated at port 1 and port 2 due to differential-mode excitation. The remaining term P_{loss} accounts for the power that is not captured by the differential- and common-mode port responses.

Using mixed-mode S-parameters, and assuming that only the differential-mode incident wave at port 1 is excited, the outgoing mixed-mode waves are given by

$$\begin{aligned} b_{d1} &= S_{dd11} a_{d1}, \qquad & b_{d2} &= S_{dd21} a_{d1}, \\ b_{c1} &= S_{cd11} a_{d1}, \qquad & b_{c2} &= S_{cd21} a_{d1}. \end{aligned} \tag{2.42}$$

Here, a_{d1} is the incident differential-mode power wave at port 1. The quantities b_{d1} and b_{d2} are the reflected and transmitted differential-mode waves, while b_{c1} and b_{c2} are the corresponding common-mode waves generated by differential-to-common mode conversion.

The corresponding power balance can therefore be expressed in terms of the mixed-mode S-parameters as

$$P_{\text{in},dd} = |S_{dd11}|^2 P_{\text{in},dd} + |S_{dd21}|^2 P_{\text{in},dd} + |S_{cd11}|^2 P_{\text{in},dd} + |S_{cd21}|^2 P_{\text{in},dd} + P_{\text{loss}}. \tag{2.43}$$

In this expression, $|S_{dd11}|^2 P_{\text{in},dd}$ is the reflected differential-mode power, and $|S_{dd21}|^2 P_{\text{in},dd}$ is the transmitted differential-mode power. Similarly, $|S_{cd11}|^2 P_{\text{in},dd}$ and $|S_{cd21}|^2 P_{\text{in},dd}$ describe the common-mode power generated at the input and output sides, respectively.

After normalizing all terms by the incident differential-mode power $P_{\text{in},dd}$, the power balance becomes

$$1 = |S_{dd11}|^2 + |S_{dd21}|^2 + |S_{cd11}|^2 + |S_{cd21}|^2 + \eta_{\text{loss}}, \tag{2.44}$$

where the normalized residual loss is defined as

$$\eta_{\text{loss}} = \frac{P_{\text{loss}}}{P_{\text{in},dd}}. \tag{2.45}$$

This residual loss represents the portion of the incident differential-mode power that is not observed as reflected or transmitted differential/common-mode power at the defined ports.

For convenience, the differential-to-common mode conversion contribution can be grouped into a single term:

$$\eta_{\mathrm{mc}} = |S_{cd11}|^2 + |S_{cd21}|^2, \tag{2.46}$$

where η_{mc} represents the total normalized common-mode power generated by differential-mode excitation. With this definition, (2.44) can be rewritten as

$$1 = |S_{dd11}|^2 + |S_{dd21}|^2 + \eta_{\mathrm{mc}} + \eta_{\mathrm{loss}}. \tag{2.47}$$

For a geometrically balanced differential structure, the differential-to-common mode conversion is usually small. In this case,

$$|S_{cd11}|^2 + |S_{cd21}|^2 \ll 1, \tag{2.48}$$

and the mode-conversion term can be neglected. The residual loss can then be approximated as

$$\eta_{\mathrm{loss}} \approx 1 - |S_{dd11}|^2 - |S_{dd21}|^2. \tag{2.49}$$

This equation shows that the reduction of S_{dd21} is not necessarily equal to dissipative material loss. Part of the missing differential-mode power may be caused by reflection, while the remaining residual term may include conductor loss, dielectric loss, radiation loss, and leakage into the surrounding PCB cavity.

The total loss term in (2.49) can be further divided into conductor loss, dielectric loss, and radiation loss:

$$\eta_{\mathrm{loss}} = \eta_{\mathrm{c}} + \eta_{\mathrm{d}} + \eta_{\mathrm{rad}}, \tag{2.50}$$

where η_{c} denotes conductor loss, including copper loss and surface roughness effects, η_{d} denotes dielectric loss caused by the finite loss tangent of the substrate material, and η_{rad} denotes radiation loss into the PCB cavity. The quantity η_{loss} is dimensionless; when multiplied by 100, it represents the percentage of the input differential-mode power that is dissipated as loss.

Among these mechanisms, radiation loss is particularly important for via transitions at high frequencies. When current flows through a vertical via, the via behaves as a three-dimensional discontinuity and can excite electromagnetic fields between adjacent reference planes. Part of the signal energy may then propagate laterally in the plane cavity instead of remaining confined around the intended differential transition. This mechanism is often referred to as via leakage or cavity radiation.

In a lossless simulation model, the conductor and dielectric losses can be removed by using perfect electric conductors and setting the dielectric loss tangent to zero. If absorbing boundaries are applied around the simulation domain, the remaining loss extracted from the S-parameters can be interpreted mainly as radiation loss. Under this condition,

$$\eta_{\mathrm{loss}} \approx \eta_{\mathrm{rad}} \approx 1 - |S_{dd11}|^2 - |S_{dd21}|^2, \tag{2.51}$$

assuming that mode conversion is negligible. This provides a useful way to evaluate how much differential-mode energy leaks from the via transition into the surrounding PCB cavity. In this work, the extracted radiation-loss term is then used in Section 3.6 to compare the cylindrical and conical microvia models. As will be shown, the vertical geometry of microvia is important for accurately capturing the radiation behavior of the fabricated microvia transition.

Chapter 3

Impact of Microvia Vertical Geometry on Signal Integrity

3.1 Introduction

In electromagnetic simulations of microvias, cylindrical via models are commonly used as an idealized representation of the actual structure. Such models provide a convenient and computationally efficient approximation for analyzing the electrical behavior of vertical interconnects in multilayer PCB designs. However, in practical PCB manufacturing, microvias are typically formed through laser drilling processes, which produce vias with tapered sidewalls rather than perfectly vertical cylindrical walls. As a result, the actual microvia geometry is more accurately represented by a tapered conical structure with a certain taper angle.

In this chapter, the impact of via geometry is further investigated under different vertical transition configurations, specifically L3/L7, L3/L9, and L3/L15 structures with varying transition lengths. Here, Lx/Ly denotes a vertical transition where Lx represents the fan-in layer and Ly represents the fan-out layer. A comparative analysis is performed between two geometric representations: the polygonal cylindrical approximation used in the baseline model and the more realistic tapered conical microvia structure. The objective is to evaluate how the vertical geometric differences between these two microvia models influence the simulated SI performance. The analysis focuses on key SI metrics, including return loss, insertion loss, Maximum Available Transmission (MAT), TDR, differential-to-common mode conversion, impedance variation, and coupling effects between 2 adjacent interconnect structures.

3.2 Simulation Structure and Key Parameters

3.2.1 Stackup Configuration

The PCB stackup used in this study follows a standard high-speed multilayer configuration commonly adopted in industrial designs. Due to confidentiality constraints, the exact layer arrangement and material specifications are not disclosed. The stackup shown in Fig 3.1 is representative and does not reflect the exact design due to confidentiality constraints. However, the stackup can be generally described as a symmetric multilayer structure consisting of a core layer with copper layers, followed by alternating prepreg and copper layers symmetrically arranged above and below the core.

Layer ID	
TOP	Copper
	Prepreg
2	Copper
	Prepreg
...	Copper
	Core
	Copper
	Prepreg
N-1	Copper
	Prepreg
BOTTOM	Copper

Figure 3.1: Representative 6-layer PCB stackup used for SI analysis.

3.2.2 Geometrical Parameters

The Fig 3.2 illustrates the key geometrical parameters used in the differential-pair microvia transition model. These geometrical dimensions are the main parameters used to construct the HFSS simulation model.

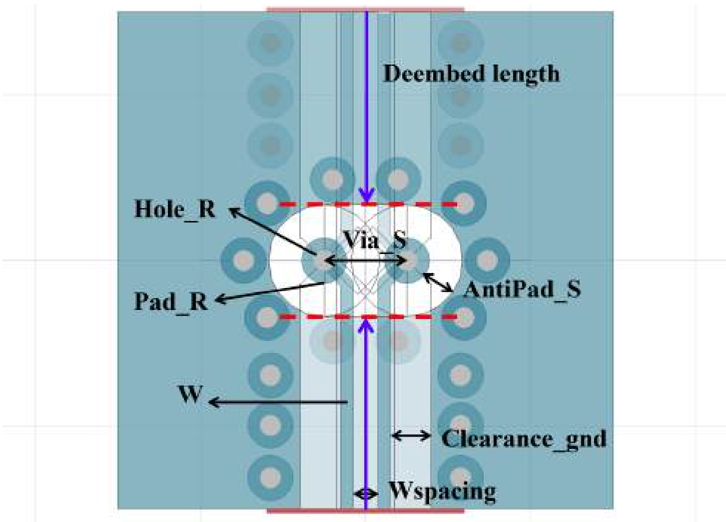

Figure 3.2: Key geometrical dimensions of the differential pair.

The parameter `Via_S` denotes the center-to-center spacing between the two signal vias, while Hole_R and Pad_R represent the radius of the drilled via hole and the surrounding capture pad, respectively. The dashed circular regions indicate the antipad openings in the reference plane, and AntiPad_S defines the size of the clearance region around each signal via. The trace width and differential trace spacing are denoted by W and Wspacing, respectively. In addition, Clearance_gnd describes the distance between the signal trace and the nearby ground clearance boundary. Except for the antipad size, the other geometrical parameters are fixed to the values listed in Table 3.1, which are selected according to typical industrial design values.

In the following study, the antipad size of the cylindrical microvia model is first swept to determine the optimized antipad dimensions for the three transition models, namely L3–L7, L3–L9, and L3–L15. After the optimized antipad dimensions are determined, all geometrical parameters are fixed, and the conical and cylindrical microvia models are compared under the same design conditions.

Table 3.1: Key geometrical dimensions of the simulated structure.

Symbol	Parameter	Value
Via_S	Signal-via spacing	500 μm
Hole_R	Hole radius	62.5 μm
Pad_R	Pad radius	137.5 μm
AntiPad_S	Antipad size	150–500 μm
W	Trace width	75 μm
Wspacing	Trace spacing	150 μm
Clearance_gnd	Ground clearance	250 μm

3.2.3 Simulation Setup and Convergence Criteria

In HFSS, this convergence is commonly controlled by the $\Delta S_{\max}$. According to the HFSS help documentation [32, 33], ΔS is defined as the magnitude of the change in the S-parameters between two consecutive passes, and the analysis stops when the changes of all monitored S-parameters are smaller than the specified threshold. Otherwise, the simulation proceeds until the specified number of passes has been completed.

For an S-parameter S_{ij}, the change between two consecutive adaptive passes can be written as

$$\Delta S_{ij}^{(n)} = \left| S_{ij}^{(n)} - S_{ij}^{(n-1)} \right|, \tag{3.1}$$

where i and j cover all matrix entries, and n represents the pass number. The solution is considered converged when

$$\max_{i,j} \Delta S_{ij}^{(n)} < \Delta S_{\max}, \tag{3.2}$$

where $\Delta S_{\max}$ denotes the user-defined Maximum Delta S threshold. This criterion therefore represents an absolute convergence tolerance for the S-parameter variation in linear scale.

This convergence criterion is particularly important when interpreting very small S-parameter components or when comparing two simulation results with only a small difference. The dominant differential-mode responses, such as S_{dd11} and S_{dd21}, usually have much larger magnitudes than the mode-conversion terms. In contrast, S_{cd} and S_{dc} may be several tens of decibels lower. When the absolute value of an S-parameter is very small, or when the difference between two simulated S-parameters is comparable to the convergence tolerance, the observed variation may be influenced by the numerical convergence limit rather than by a physically significant change in the structure. Therefore, small differences in low-level S-parameter quantities should be interpreted with caution, especially after conversion to the dB scale.

This effect can be illustrated by considering a nominal magnitude $|S|$ and a finite tolerance ΔS. A simple magnitude-based range is given by

$$|S|_{\mathrm{lower}} = |S| - \Delta S, \qquad |S|_{\mathrm{upper}} = |S| + \Delta S. \tag{3.3}$$

The corresponding values in dB are

$$S_{\mathrm{lower,dB}} = 20\log_{10}\left(|S| - \Delta S\right), \qquad S_{\mathrm{upper,dB}} = 20\log_{10}\left(|S| + \Delta S\right). \tag{3.4}$$

The lower bound is meaningful only when $|S| > \Delta S$. When $|S| \leq \Delta S$,the lower bound cannot be converted into a valid dB value, which indicates that the corresponding very small S-parameter value is close to the numerical convergence level.

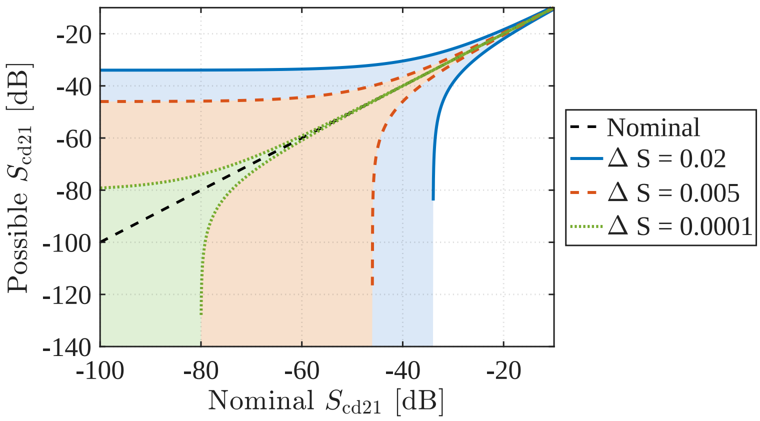

Figure 3.3: Illustrative possible range of S_{cd21} under different ΔS_{max} criteria. The colored regions are obtained by applying $|S| \pm \Delta S$ in linear magnitude and then converting the results to dB, Figure layout based on HFSS help documentation [33].

Fig. 3.3 illustrates this behavior for S_{cd21} under different ΔS_{max} criteria. The figure is not intended to provide a rigorous error bound, but rather to show

how a finite convergence tolerance can affect the interpretation of very small mode-conversion values. Therefore, in this thesis, very small S_{cd} and S_{dc} results are mainly used to identify relative trends between different microvia geometries or misalignment cases, rather than to draw conclusions from minor absolute differences.

3.2.4 3D Model Overview

Fig. 3.4 shows the 3D models of differential-line microvia transition structures. Each model includes a pair of differential traces, cascaded signal microvias for vertical layer transition, and surrounding ground microvias. The ground vias surrounding the differential signal vias provide return-current paths during layer transition. They also help reduce parasitic inductance, suppress electromagnetic leakage, and improve SI performance. The stacked dielectric and metal layers of the PCB are also illustrated to indicate the multilayer routing environment.

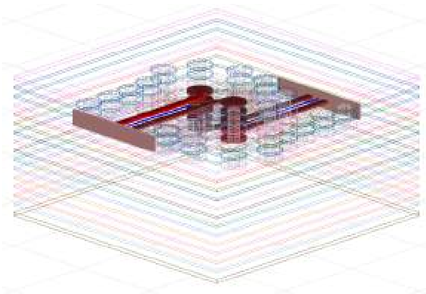

(a) Differential microvia transition from L3 to L7

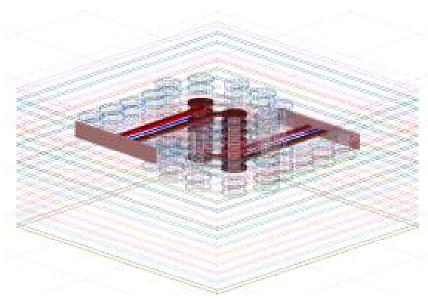

(b) Differential microvia transition from L3 to L9

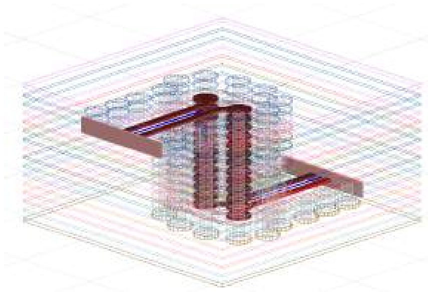

(c) Differential microvia transition from L3 to L15

Figure 3.4: Differential microvia transition structures with different layer spans.

The difference among the three subfigures lies in the transition depth of the differential pair. In Fig. 3.4a, the differential signals transition from Layer 3 to Layer 7. Stacked microvias are vertically aligned on adjacent layers. In Fig. 3.4b, the transition extends from Layer 3 to Layer 9. In Fig. 3.4c, the transition further extends from Layer 3 to Layer 15 composed of 4 individual microvias. Since each microvia connects only two adjacent layers, a deeper transition requires more cascaded microvias. Therefore, from (a) to (c), the vertical transition length gradually increases, and the number of cascaded microvias also increases.

3.3 Baseline Design Optimization of the Cylindrical Microvia Transition

Before comparing the cylindrical and conical microvia models, the cylindrical model is first optimized to establish a baseline via-transition design. The overall height of the via transition is constrained by the PCB stackup thickness, but it can be varied by connecting the signal path to different target layers. In contrast, the microvia diameter and pad diameter are usually limited by fabrication capability, reliability requirements, and practical cost considerations. Therefore, these parameters are kept fixed in this study so that the influence of other geometrical factors can be analyzed more clearly [34]. Under these constraints, the antipad size becomes the main adjustable design parameter for optimizing the impedance matching and signal-integrity performance of the microvia transition. Moreover, the antipad size is selected as the swept parameter because it directly affects the local impedance profile and the discontinuity around the microvia transition. The optimization is evaluated using several signal-integrity metrics, including S_{dd11}, S_{dd21} and TDR result. The optimized cylindrical models are then used as reference cases for the subsequent comparison with the corresponding conical microvia models.

3.3.1 S-Parameter Analysis (S_{dd11})

Layer 3 to Layer 7 transition Fig. 3.5a shows the differential return loss S_{dd11} of the Layer 3 to Layer 7 transition with different antipad sizes. Since this transition has the shortest vertical length among the investigated cases, the accumulated discontinuity introduced by the stacked microvias is relatively weak. Therefore, the S_{dd11} responses vary smoothly over the whole frequency range, and no pronounced narrowband resonance is observed.

In the low-frequency range, approximately below 25 GHz, increasing the antipad size leads to a clear reduction in S_{dd11}. This indicates that a larger antipad helps reduce the capacitive loading around the via transition and improves the local impedance matching. However, as the frequency increases, the curves gradually converge. In the range of about 25–55 GHz, different antipad sizes give similar S_{dd11} levels, clustered around approximately -10 dB. This suggests that the antipad size is no longer the dominant factor limiting the return-loss performance in this frequency band.

Overall, the Layer 3 to Layer 7 transition exhibits a relatively stable broadband reflection response. The antipad size mainly affects the lower frequency range, while its influence becomes weaker at higher frequencies.

Layer 3 to Layer 9 transition Fig. 3.5b shows the differential return loss S_{dd11} of the Layer 3 to Layer 9 transition with different antipad sizes. Similar

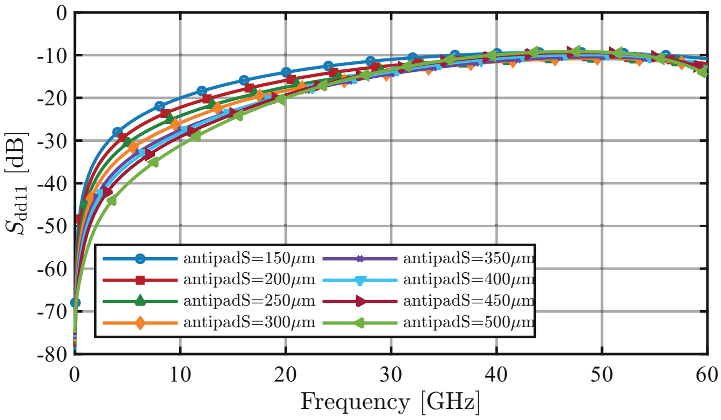

(a) Layer 3 to Layer 7 transition;

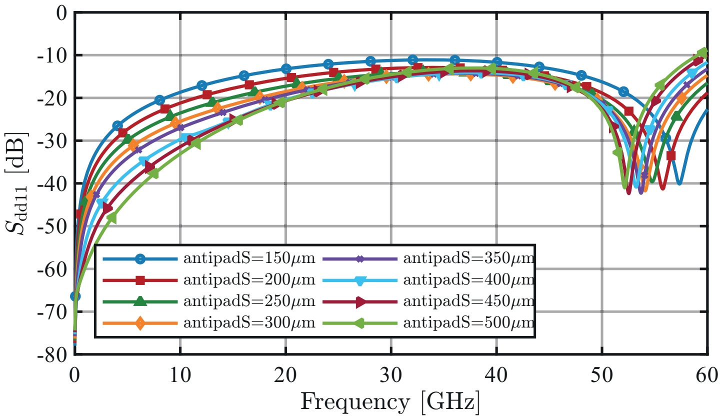

(b) Layer 3 to Layer 9 transition;

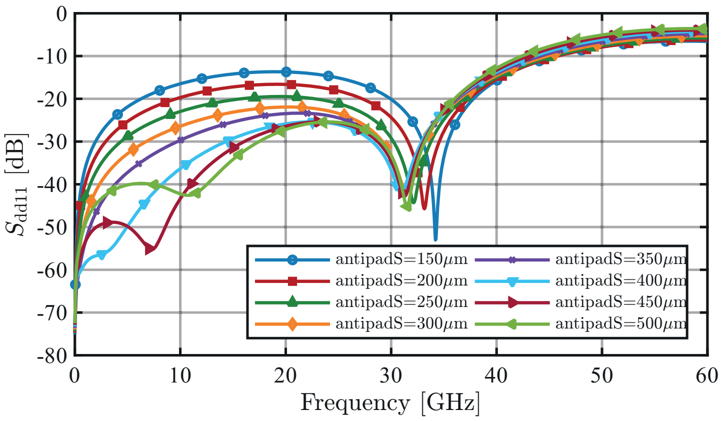

(c) Layer 3 to Layer 15 transition;

Figure 3.5: The return-loss responses of the transition structures from Layer 3 to different target layers are shown for different antipad sizes.

to the Layer 3 to Layer 7 transition, increasing the antipad size mainly improves S_{dd11} in the low-frequency range below approximately 25 GHz, while the curves gradually converge in the middle-frequency range from about 25 to 45 GHz.

A distinct feature of the Layer 3 to Layer 9 transition is the pronounced resonance-like dip observed around 52–56 GHz. As the antipad size increases from 150 μm to 500 μm, the dip shifts to lower frequency. This trend can be qualitatively interpreted using the equivalent LC resonance relation

$$f_0 \approx \frac{1}{2\pi\sqrt{L_{\mathrm{eq}}C_{\mathrm{eq}}}}. \tag{3.5}$$

A larger antipad opening generally reduces the parasitic capacitance between the via pad and the surrounding reference planes. However, when the antipad size increases, the reference-plane metal is removed over a larger area and the nearby ground vias are placed farther away from the signal vias. This enlarges the effective return-current loop and spreads the magnetic field over a larger dielectric region, leading to an increase in the stored magnetic energy and hence a larger effective inductance. Since the observed resonance-like dip moves toward a lower frequency, the overall product $L_{\mathrm{eq}}C_{\mathrm{eq}}$ is likely to increase. This suggests that the increase in effective inductance dominates over the reduction in capacitance in this high-frequency range.

Overall, the antipad size mainly affects the low-frequency impedance matching and the high-frequency resonance behavior of the Layer 3 to Layer 9 transition. The response is more sensitive to geometrical variation than that of the shorter Layer 3 to Layer 7 transition due to the increased transition length.

Layer 3 to Layer 15 transition Fig. 3.5c shows the differential return loss S_{dd11} of the Layer 3 to Layer 15 transition with different antipad sizes. The low-frequency behavior is generally similar to the Layer 3 to Layer 7 and Layer 3 to Layer 9 cases, where a larger antipad size tends to reduce S_{dd11}. However, unlike the shorter transitions, the response no longer decreases monotonically and smoothly with increasing antipad size. When the antipad size is increased to 400, 450, and 500 μm, additional fluctuations appear in the low-frequency range, suggesting more complex resonance-like behavior. This indicates that, for a longer transition, the antipad size affects not only the local impedance discontinuity, but also the distribution of multiple parasitic resonant modes.

A pronounced resonance-like dip is observed around 31–35 GHz, where S_{dd11} reaches approximately -40 to -55 dB. The dip position does not shift monotonically toward lower frequencies as in the Layer 3 to Layer 9 case. Instead, for larger antipad sizes, especially 400–500 μm, the dip tends to move back toward higher frequencies. This indicates that the resonance condition is no longer governed by a single capacitance effect, but by the combined variation of equivalent capacitance, inductance, and coupling between different microvia sections. Above approximately 40 GHz, the curves gradually converge and remain around -5 to -15 dB.

Overall, the Layer 3 to Layer 15 transition exhibits the most complex frequency response and the highest sensitivity to antipad variation among the three investigated structures. This is mainly due to its longer vertical path, stronger accumulated discontinuity, more significant return-current detour, and stronger coupling between multiple via sections.

3.3.2 S-Parameter Analysis (S_{dd21})

As shown in Fig. 3.2, the blue solid arrows indicate the de-embedding length applied to the wave ports. After de-embedding, the transmission-line sections outside the red dashed lines are removed from the simulation results, and the remaining structure mainly consists of the microvia transition and its nearby discontinuities. Therefore, S_{dd21} mainly characterizes the differential-mode transmission through the via transition, rather than the insertion loss of the entire transmission-line path.

Layer 3 to Layer 7 transition As shown in Fig. 3.6a, for the L3–L7 transition, S_{dd21} remains between approximately 0 and -0.75 dB over the entire investigated frequency range. This relatively small transmission degradation indicates that the differential-mode signal is generally well transmitted through the via transition. The degradation in S_{dd21} is mainly attributed to impedance mismatch in the transition region rather than conductor loss, as indicated by the non-monotonic frequency response.

As the antipad size increases, the S_{dd21} curves show more noticeable differences above approximately 30 GHz. The small-antipad cases, especially 150 μm and 200 μm, deviate more clearly from the other curves due to stronger capacitive coupling between the signal pads and the surrounding reference planes.

A transmission dip appears around 45–50 GHz, and its depth varies with antipad size. This behavior is consistent with the corresponding S_{dd11} response, where stronger reflection leads to larger mismatch loss and lower transmitted differential-mode power. Therefore, the S_{dd21} results indicate that the antipad size mainly affects the high-frequency transmission by modifying the local impedance environment, return-current path, and ground-via distribution around the transition.

Layer 3 to Layer 9 transition As shown in Fig. 3.6b, for the L3–L9 transition, S_{dd21} remains between approximately 0 and -0.9 dB over the entire investigated frequency range. The influence of antipad size becomes more pronounced at higher frequencies. Below approximately 30 GHz, the S_{dd21} curves are relatively close to each other, indicating that the transition is less sensitive to antipad variation in this frequency range. Between 20 and 40 GHz, the 150 μm case shows a larger transmission reduction than the other cases. This can be attributed to the stronger capacitive coupling between the signal pads and the surrounding reference planes for smaller antipad openings, which changes the local impedance condition around the via transition.

At higher frequencies, especially near 55–60 GHz, the larger antipad cases show a more significant transmission degradation. This behavior is consistent with the corresponding S_{dd11} response, where stronger reflection leads to larger mismatch loss and lower transmitted differential-mode power. For larger antipad openings, the reference-plane clearance becomes larger and the surrounding ground vias are

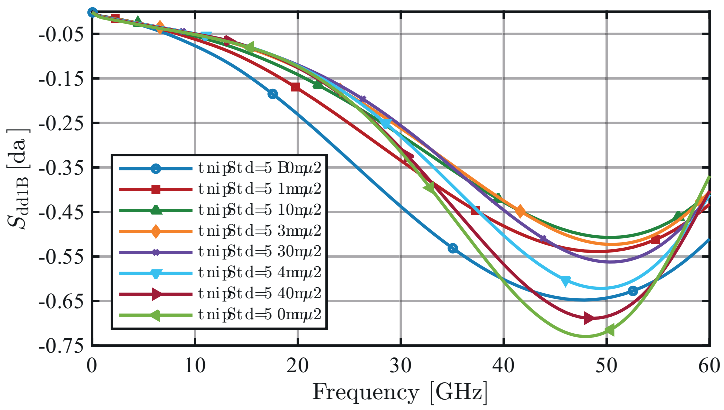

(a) Layer 3 to Layer 7 transition;

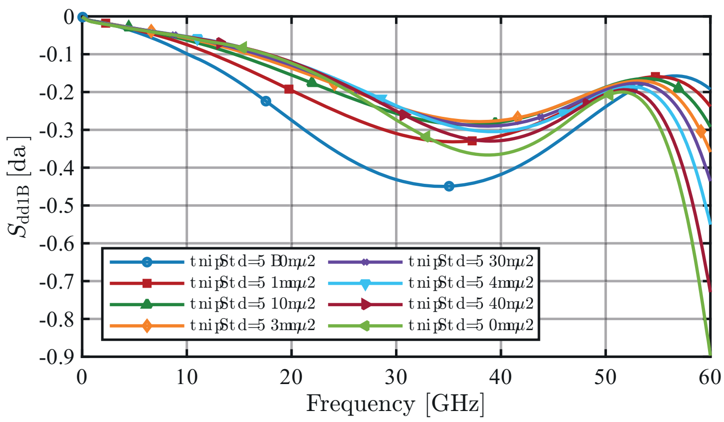

(b) Layer 3 to Layer 9 transition;

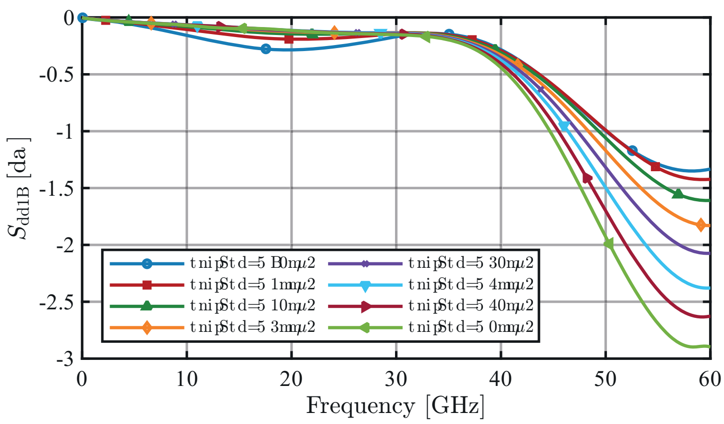

(c) Layer 3 to Layer 15 transition;

Figure 3.6: The differential insertion-loss responses of the transition structures from Layer 3 to different target layers are shown for different antipad sizes.

pushed farther away from the signal vias. As a result, the return-current path becomes less compact and the ground-via confinement around the transition is weakened, leading to stronger high-frequency mismatch.

Overall, the S_{dd21} results for the L3–L9 transition show that the antipad size mainly affects the high-frequency transmission behavior. The observed transmission degradation is strongly correlated with the corresponding S_{dd11} response, confirming that mismatch loss is the dominant mechanism in this transition.

Layer 3 to Layer 15 transition For the L3–L15 transition, the overall transmission degradation is more pronounced than that of the L3–L7 and L3–L9 transitions. As shown in Fig. 3.6c, all curves remain close to 0 dB below approximately 35 GHz, indicating that the differential-mode signal can still be well transmitted through the transition at low and middle frequencies. However, S_{dd21} starts to decrease rapidly from around 40 GHz, and the separation between different antipad sizes becomes much more significant. At 60 GHz, S_{dd21} varies from approximately -1.3 dB to nearly -3 dB. Compared with the L3–L9 transition, this larger degradation indicates that the longer via transition accumulates stronger discontinuities and high-frequency mismatch.

The influence of antipad size is particularly evident in the high-frequency range. For frequencies below approximately 40 GHz, the differences among different antipad sizes are relatively small. In contrast, above 40 GHz, larger antipad openings generally lead to more severe transmission degradation, especially for the 400–500 μm cases. This is because increasing the antipad size enlarges the reference-plane clearance and pushes the surrounding ground vias farther away from the signal vias. As a result, the return-current path becomes less compact, the ground-via confinement around the transition is weakened, and the high-frequency impedance mismatch becomes more pronounced.

This behavior is consistent with the corresponding S_{dd11} response in Fig. 3.5c. In the frequency range where S_{dd11} increases, more differential-mode power is reflected back to the input port, leading to a lower S_{dd21}. Therefore, the transmission degradation of the L3–L15 transition is mainly caused by reflection-induced mismatch loss rather than conductor loss. Overall, the L3–L15 transition is the most sensitive case among the three transitions, because its longer vertical path accumulates stronger discontinuities and is more affected by the antipad-dependent return-current path and ground-via distribution.

3.3.3 Time-Domain Reflectometry (TDR) Response

The TDR impedance responses of the three transition structures are shown in Fig 3.7. For all three cases, the impedance first drops below the nominal differential impedance of 85 Ω, then rises above 85 Ω, and finally gradually returns to a stable platform close to 85 Ω. This indicates that the local transition region first exhibits a capacitive discontinuity, followed by an inductive recovery or compensation effect.

It should be noted that the time positions in the TDR response are not assigned to a single specific pad, layer, or microvia section. As discussed in Section 2.4.2,

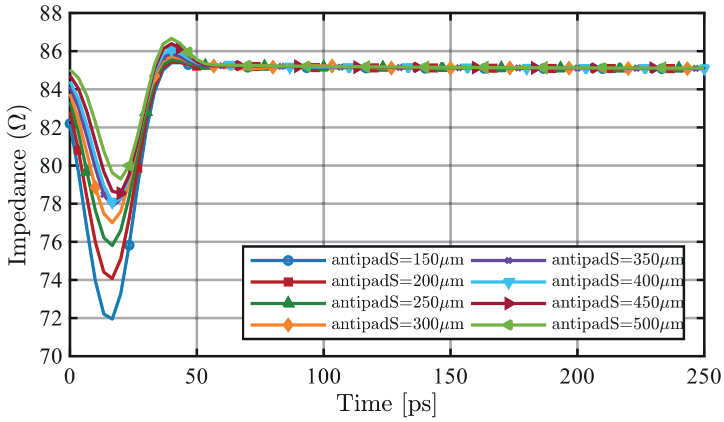

(a) Layer 3 to Layer 7 transition;

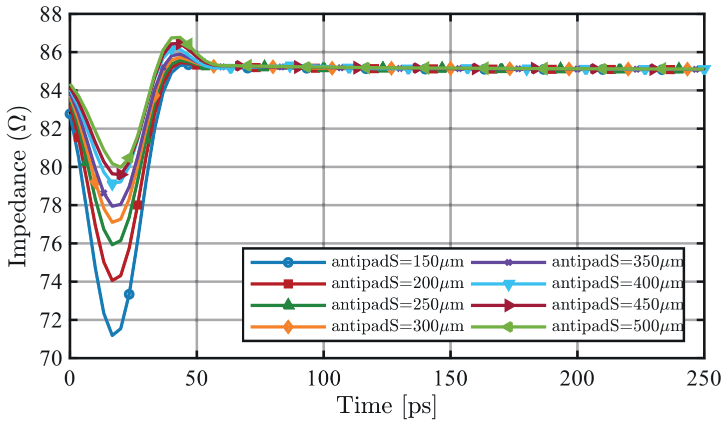

(b) Layer 3 to Layer 9 transition;

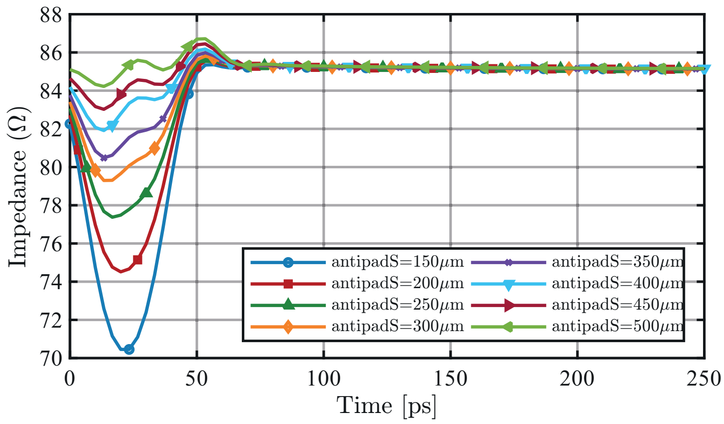

(c) Layer 3 to Layer 15 transition;

Figure 3.7: The TDR impedance responses of the transition structures from Layer 3 to different target layers are shown for different antipad sizes.

the time-to-distance conversion is limited by the rise time and the simulation bandwidth. In addition, the multilayer transition contains several closely spaced discontinuities, including pads, antipads and vertical microvia sections. Therefore, the impedance dip and overshoot are interpreted as the combined response of the local microvia transition region rather than the response of an individual geometrical feature.

Layer 3 to Layer 7 transition For the Layer 3 to Layer 7 transition shown in Fig. 3.7a, the impedance dip is relatively narrow and the curves return quickly to the stable impedance level. This is consistent with the shorter vertical transition length, which introduces a weaker discontinuity compared with the longer transition cases. As the antipad size increases, the minimum impedance of the dip gradually increases. This means that the low-impedance capacitive loading becomes weaker, because a larger antipad reduces the effective capacitive coupling between the microvia pad and the nearby reference plane.

Layer 3 to Layer 9 transition A similar trend can be observed for the Layer 3 to Layer 9 transition in Fig. 3.7b. The impedance dip becomes shallower when the antipad size is increased, indicating reduced capacitive discontinuity. A small impedance overshoot appears after the initial dip. This suggests that, as the capacitive discontinuity is reduced by increasing the antipad size, the inductive contribution of the overall transition region becomes more visible. This contribution may come not only from the vertical microvia path, but also from the transmission-line sections above or below the antipad openings, where the return-current path is disturbed by the enlarged reference-plane cutout.

Layer 3 to Layer 15 transition For the longest transition, from Layer 3 to Layer 15, shown in Fig. 3.7c, the TDR response becomes more distributed. The impedance dip extends over a wider time range, and the difference between different antipad sizes becomes more pronounced. This indicates that the longer vertical transition accumulates stronger parasitic effects and is more sensitive to the local geometry around the microvia and reference-plane openings. Compared with the Layer 3 to Layer 7 and Layer 3 to Layer 9 structures, the Layer 3 to Layer 15 transition exhibits a more pronounced sensitivity to antipad size when the antipad size is larger than 300 μm.

Overall, the TDR results confirm that increasing the antipad size weakens the capacitive loading of the transition, as reflected by the rising bottom of the impedance dip. The following impedance overshoot represents the corresponding inductive recovery of the transition region. Therefore, the TDR response provides a time-domain explanation for the local impedance mismatch and supports the interpretation of the frequency-domain S-parameter results, especially the differential reflection coefficient S_{dd11}.

3.3.4 Optimized Antipad Sizes for the Baseline Cylindrical Models

Based on the preceding S_{dd11}, S_{dd21}, and TDR analyses, suitable antipad sizes are selected for the three cylindrical baseline via-transition structures. The selection is not based on a single metric only, but on the overall signal-integrity performance, including impedance matching, transmission loss, and the TDR result.

For the L3–L7 transition, an antipad size of 300 μm is selected. This value provides a good compromise between reflection reduction and stable transmission performance. A similar antipad size of 300 μm is also selected for the L3–L9 transition, where the structure still maintains acceptable impedance matching and insertion-loss behavior over the frequency range of interest. For the longer L3–L15 transition, the response is more sensitive to the antipad size due to the increased vertical transition length and the accumulated discontinuities. In this case, a smaller antipad size of 200 μm is selected to avoid stronger high-frequency mismatch.

The selected baseline antipad sizes are therefore summarized as follows:

$$\begin{aligned} \text{L3}-\text{L7}: &\quad 300\ \mu\text{m}, \\ \text{L3}-\text{L9}: &\quad 300\ \mu\text{m}, \\ \text{L3}-\text{L15}: &\quad 200\ \mu\text{m}. \end{aligned} \tag{3.6}$$

These optimized cylindrical models are used as the reference structures in the following section, where the signal-integrity performance of cylindrical and conical microvia transitions is compared under the same layer-transition configurations.

3.4 SI Comparison of Microvia Structures

3.4.1 Geometrical Modeling of Cylindrical and Conical Microvias

As illustrated in Fig. 3.8, two different microvia geometries are considered in this work. The upper part of the figure shows the polygonal cylindrical microvia model, including its cross-section and 3D view. The lower part shows the tapered conical microvia model, including the vertical cut and 3D view, where θ denotes the sidewall angle. Compared with the idealized cylindrical geometry, the tapered conical geometry provides a more realistic representation of practical fabricated microvias in PCB manufacturing.

In electromagnetic simulations, curved metal surfaces are discretized into polygonal faces for numerical solution. Therefore, the cylindrical microvia is modeled using a polygonal approximation rather than a perfectly smooth circular surface [35]. A smaller number of polygon sides can reduce the geometric complexity, mesh density, matrix size, and simulation time. In this work, all cylindrical microvias are modeled using a 12-sided polygonal approximation to balance geometrical accuracy and computational cost. The conical microvias were also modeled using 12-sided polygonal cross sections, consistent with the cylindrical microvia model. The hexagonal shape in Fig. 3.8 is only used for visual clarity and does not represent the actual number of polygon sides used in the simulations.

Layer 3 to Layer 7 transition Fig. 3.9 illustrates the geometrical definition of the conical microvia angle used in this work. The upper row shows the vertical cross-sectional view of the tapered via for three different sidewall angles, $\theta = 65°$,

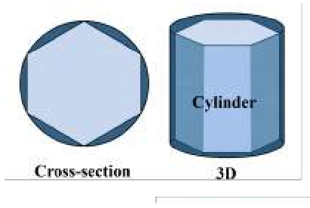

(a) Polygonal cylindrical microvias;

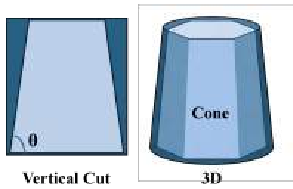

(b) Polygonal tapered conical microvias;

Figure 3.8: Geometric approximation of cylindrical and conical microvia structures. The microvias are modeled with 12 sides in the simulations, but are shown as hexagonal shapes here for clarity.

75°, and 85°. A smaller angle corresponds to a more strongly tapered microvia, whereas an angle close to 90° approaches the cylindrical-via limit. The lower row shows the corresponding three-dimensional geometries, where the bottom opening is kept larger than the top opening due to the conical sidewall profile.

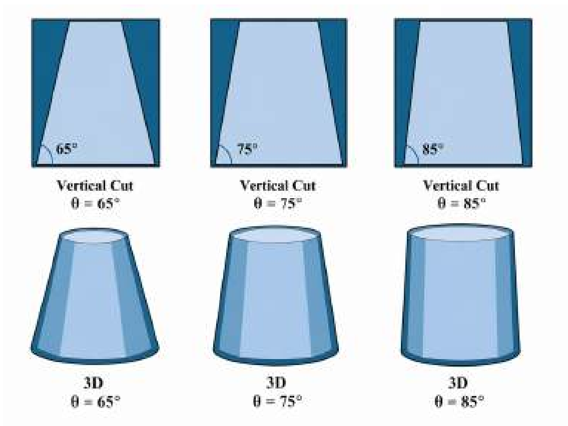

Figure 3.9: Vertical cross-sectional and three-dimensional illustrations of conical microvias with sidewall angles of $\theta = 65°$, $75°$, and $85°$. A smaller angle indicates a stronger tapering effect, while a larger angle approaches the cylindrical-via limit.

Based on this geometrical description, the influence of the conical microvia shape is further investigated for the L3–L7 transition. The cylindrical model is first used as the reference case. It is then compared with conical signal-via models using sidewall angles of 65°, 75°, and 85°. In these conical cases, only the signal microvias are modeled as tapered conical vias, while the ground vias remain cylindrical. This comparison is used to evaluate how the cone angle of the signal microvia affects the signal-integrity performance of the L3–L7 transition.

Layer 3 to Layer 15 transition As shown in Fig. 3.10, three differential microvia interconnect simulation models are established in this work. All three models describe the differential signal transition from Layer 3 to Layer 15 through a multistage microvia structure. The main difference among these models lies in the geometric representation of the microvias.

According to their electrical net in the simulated structure, the microvias are divided into signal microvias and ground microvias. The signal microvias form the vertical part of the differential signal path, while the ground microvias are connected to the reference planes and provide local return-current paths around the transition.

In the model shown in Fig. 3.10(a), all microvias are modeled using the default polygonal cylindrical geometry in HFSS. In the model shown in Fig. 3.10(b), only the differential signal microvias are modeled with a conical geometry, while the surrounding ground microvias remain as the default polygonal cylindrical structures. In the model shown in Fig. 3.10(c), both the signal microvias and the ground microvias are modeled using conical geometries.

By comparing these three models, the influence of different microvia geometric representations on the SI performance of the differential interconnect can be investigated.

3.4.2 Comparison of SI Performance and Simulation Efficiency

Layer 3 to Layer 7 transition The comparison results for the cylindrical and conical microvia models are shown in Fig. 3.11. The first column presents the L3–L7 transition results, where the cylindrical reference model is compared with conical signal-via models using cone angles of 65°, 75°, and 85°.

As shown in Fig. 3.11a, the differential return loss S_{dd11} of the four models remains very close over most of the frequency range. This indicates that the cone angle of the signal microvia has only a limited influence on the impedance matching of the relatively short L3–L7 transition. Small differences appear mainly at high frequencies, but the overall reflection behavior is similar for all cases.

Compared with S_{dd11}, the differential insertion loss S_{dd21} in Fig. 3.11c shows a more visible separation among the curves above approximately 30 GHz. However, this separation should not be over-emphasized because the absolute magnitude of S_{dd21} is still very small. Over the entire frequency range, the insertion loss remains within approximately 0.6 dB. Even near 50 GHz, where the largest difference is observed among the 65°, 75°, and 85° conical cases, the difference is only about 0.1 dB. At other frequencies, the difference is even smaller. Therefore, although the

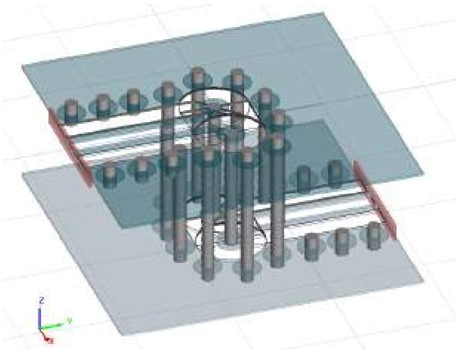

(a) All microvias with the default polygonal cylindrical geometry in HFSS.

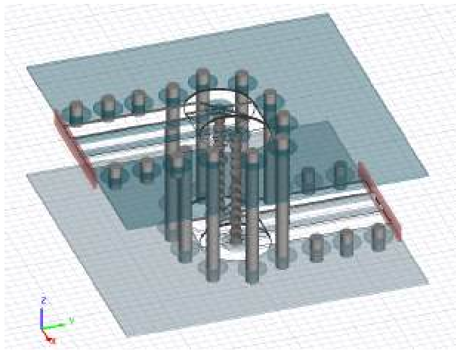

(b) Conical signal microvias with polygonal cylindrical ground microvias.

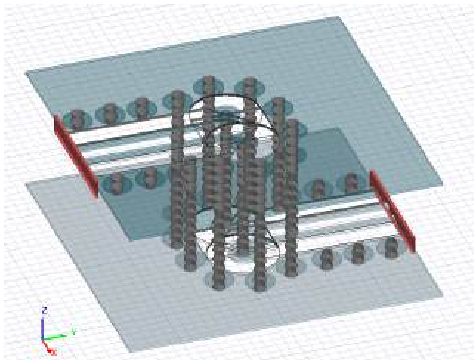

(c) Conical signal and ground microvias.

Figure 3.10: Three microvia geometric models used in the differential interconnect simulation from Layer 3 to Layer 15.

conical angle slightly affects the high-frequency transmission response, the overall impact on the L3–L7 insertion loss remains limited.

The mode-conversion response S_{cd21} for the L3–L7 transition is shown in Fig. 3.11e. For all investigated models, S_{cd21} remains at a very low level over the entire frequency range. Most values are below approximately -80 dB, indicating that the differential-to-common mode conversion is negligible. Although some differences can be observed among the curves at high frequencies, these differences should not be over-interpreted because the absolute magnitude of S_{cd21} is extremely small. In addition, since these values are far below the accuracy level implied by the selected $\Delta S_{\max} = 0.001$ criterion, the curves are mainly used to confirm the negligible level of mode conversion rather than to provide a precise quantitative comparison.

The TDR results are shown in Fig. 3.11g. Overall, the cylindrical reference model and the conical signal microvia models exhibit very similar profiles, indicating that the cone angle has only a weak influence on the TDR response of the L3–L7 transition. In particular, the cylindrical reference model and the 85° conical model are almost overlapped over the entire time range. This is expected because the 85° conical microvia is geometrically close to the cylindrical microvia.

Although the difference is small, a clear trend can still be observed around the initial capacitive dip. As the cone angle decreases from 85° to 75° and 65°, the depth of the capacitive dip becomes slightly smaller. The minimum impedance increases only slightly, from about 77 Ω to 78 Ω and then to 79 Ω, but the trend suggests that the effective capacitive discontinuity is reduced when the conical microvia becomes more tapered. This can be understood by analogy with a parallel-plate capacitance. When one of the conducting surfaces becomes inclined, the effective overlapping area between the metal regions is reduced, leading to a weaker local capacitance and therefore a shallower TDR dip.

Layer 3 to Layer 15 transition Fig. 3.11 compares the simulated SI performance of the three microvia geometric models shown in Fig. 3.10. The right column presents the L3–L15 transition, where the cylindrical reference model is compared with the conical signal microvia model and the conical all microvia model. The red curves correspond to the reference model in which all microvias are modeled using the default polygonal cylindrical geometry in HFSS. The cyan curves represent the model with conical signal microvias and polygonal cylindrical ground microvias, while the blue curves correspond to the model in which both the signal and ground microvias are modeled as conical structures. The comparison includes the differential return loss S_{dd11}, differential insertion loss S_{dd21}, mode conversion S_{cd21}, and the TDR result.

As shown in Fig. 3.11b, the three models exhibit similar overall trends in S_{dd11}, but noticeable differences appear around the resonance region near 30–35 GHz. The cylindrical reference model shows a deeper return-loss notch of approximately −45 dB around 33 GHz, whereas the conical signal-via and conical all-via models show shallower notches of about −38 dB, shifted slightly toward lower frequency. This behavior indicates that the tapered microvia geometry changes the local parasitic parameters of the transition. Physically, tapering narrows the via barrel, which can reduce the local capacitance between the via pad and the surrounding reference-plane opening. At the same time, the reduced conductor cross-section and modified current path can increase the effective inductance. The observed shift of the resonance toward lower frequency suggests that the increase in effective inductance is more dominant than the reduction in capacitance for this L3–L15 transition.

The differential insertion loss S_{dd21} is shown in Fig. 3.11d. The three curves are very close below approximately 35–40 GHz, with differences generally below 0.05 dB. At higher frequencies, the separation becomes more visible. Near 60 GHz, the cylindrical reference model reaches about −1.4 dB, while the conical signal-via and conical all-via models are approximately −1.25 dB. Since the transmission lines are de-embedded and the via transition has relatively small conductor loss, this difference is mainly associated with mismatch loss rather than dissipative loss. This is also consistent with the changes observed in S_{dd11} around the resonance region. The conical signal-via and conical all-via models show very similar S_{dd21} responses, which suggests that the dominant discontinuity is mainly controlled

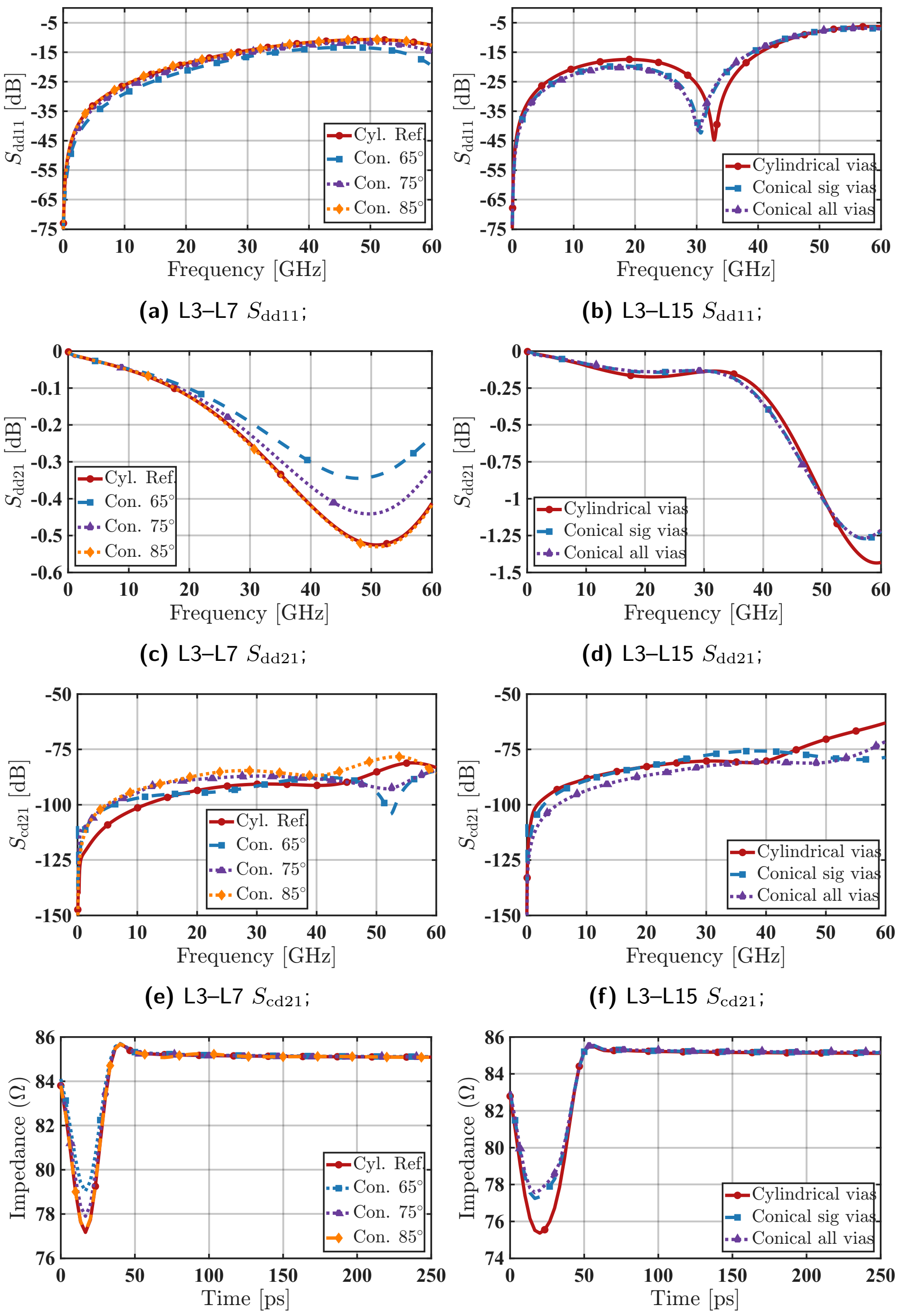

(a) L3–L7 S_{dd11}; **(b)** L3–L15 S_{dd11};

(c) L3–L7 S_{dd21}; **(d)** L3–L15 S_{dd21};

(e) L3–L7 S_{cd21}; **(f)** L3–L15 S_{cd21};

(g) L3–L7 TDR; **(h)** L3–L15 TDR;

Figure 3.11: Comparison of cylindrical and conical microvia models for the L3–L15 and L3–L7 transitions. The left column shows the L3–L15 results for different conical-via configurations, while the right column shows the L3–L7 results for different cone angles.

by the signal microvia geometry and its local coupling to the pad and antipad region. The additional tapering of the ground microvias has only a secondary effect because the ground vias mainly provide the return-current path and are less directly involved in the signal-via capacitive discontinuity.

Fig. 3.11f shows the mode-conversion response S_{cd21}. For all three models, S_{cd21} remains at a very low level, mostly below approximately -75 dB over the frequency range of interest. Therefore, the differential-to-common mode conversion is negligible compared with the differential reflection and transmission terms. Although the curves are not identical, the differences should not be over-interpreted quantitatively because the selected convergence criterion is $\Delta S_{\mathrm{max}} = 0.001$, corresponding to approximately -60 dB. Most of the S_{cd21} values are well below this level. Qualitatively, the conical all-via model gives the lowest or one of the lowest mode-conversion levels over a large part of the band. A plausible explanation is that applying the same tapered geometry to both signal and ground microvias preserves a more consistent local field and return-current distribution around the differential transition, whereas changing only the signal vias slightly modifies the local balance between the signal and return paths. Nevertheless, the absolute magnitude of S_{cd21} is extremely small, so mode conversion is not the main mechanism responsible for the observed insertion-loss differences.

The TDR differential impedance profiles are shown in Fig. 3.11h. All three models converge to approximately 85 Ω after the transition region, but a clear difference appears in the initial capacitive dip. The cylindrical reference model shows the deepest dip, with a minimum impedance of about 75.5 Ω. In comparison, the conical signal-via model increases the minimum impedance to about 77.5 Ω, and the conical all-via model gives a similar minimum around 77.8 Ω. Thus, the conical models reduce the depth of the impedance dip by approximately 2 Ω. This shallower dip indicates a weaker local capacitive discontinuity. The reason is consistent with the tapered geometry: narrowing the via reduces the effective metal overlap area between the via structure and the surrounding reference-plane opening, which reduces the local capacitance. At the same time, the tapered current path can increase the effective inductance. The reduced capacitive dip and the lower-frequency shift observed in S_{dd11} together suggest that the conical geometry modifies both the capacitive and inductive parasitics, with the inductive effect becoming more important in the resonance behavior.

Overall, the L3–L15 transition is more sensitive to the microvia geometry than the shorter L3–L7 transition. The conical models slightly reduce the high-frequency insertion loss and make the TDR capacitive dip shallower, while the differences between the conical signal-via and conical all-via models remain small. This indicates that the signal microvia geometry is the dominant factor, whereas the additional tapering of the ground microvias only provides a minor secondary contribution.

Layer 3 to Layer 15 transition Simulation Efficiency These results indicate that the all-conical via model provides the most accurate representation, since it is closest to the actual microvia geometry. However, for a simplified simulation model, representing only the signal microvias with conical geometry may provide a faster way to obtain preliminary simulation results. This is because the geometry of the signal microvias has a stronger influence on the SI performance than that of the surrounding ground microvias.

Although modeling all microvias with conical geometries provides a more detailed physical representation, it also increases the computational burden, as shown in Table 3.2.

Table 3.2: HFSS computational cost for different microvia models.

Model	**Total time**	**Adaptive meshing time**	**Max. memory per process**	**Max. matrix size**
Model A	00:31:30	00:16:34	22.4 GB	230,398
Model B	01:14:30	00:34:13	52.9 GB	447,126
Model C	11:05:57	03:00:20	185 GB	1,728,501

Note: Model A: default polygonal cylindrical microvias; Model B: signal vias replaced by polygonal truncated-conical microvias; Model C: all vias replaced by polygonal truncated-conical microvias.

Table 3.2 compares the HFSS computational cost of the three microvia models. Model A, which uses the default polygonal cylindrical microvias, has the lowest computational cost, with a total simulation time of 31.5 minutes and a maximum memory usage of 22.4 GB per process. When the signal microvias are replaced by polygonal truncated-conical microvias in Model B, the computational cost increases noticeably. The total simulation time increases to 1 hour and 14 minutes, while the maximum matrix size nearly doubles compared with Model A. Model C shows the highest computational cost because both the signal and ground microvias are modeled using polygonal truncated-conical geometries. In this case, the total simulation time reaches more than 11 hours, the maximum memory usage increases to 185 GB, and the maximum matrix size exceeds 1.7 million. This significant increase is mainly caused by the more complicated three-dimensional geometry and the finer mesh required to accurately represent the tapered viaside walls. Therefore, although the fully conical model provides a more realistic description of the fabricated microvia profile, it also introduces a much higher computational burden than the conventional cylindrical approximation. Therefore, a practical trade-off can be made by applying the conical geometry only to the signal microvias. This approach preserves the main influence of the realistic microvia profile on the differential signal path while avoiding unnecessary computational cost introduced by modeling all ground microvias with the same level of geometric detail.

3.5 Impact of Microvia Geometry on Impedance

This section studies the influence of microvia geometry on the impedance behavior of the package-to-routing-layer transition. In the considered structure, the package ball is located on the top layer, and the signal is routed from the package side to the target routing layer through a microvia transition structure. The target routing layer can be L3, L7, or L15. After the signal passes through the microvia transition and reaches the target routing layer, an impedance transformer is designed to connect the transition to the following fixed-impedance microstrip line. However, the geometry of the microvia transition can change the local parasitic capacitance and inductance. As a result, the extracted impedance point may shift from the designed value, which can also shift the S_{dd11} response and degrade the impedance matching. This mismatch may finally lead to additional reflection and power loss.

Fig. 3.12 illustrates the package ball to routing layer transition structure and its equivalent impedance-matching model. As shown in the left part of the figure, the signal is launched from the package ball and then transitions through the microvia structure from the top layer to a target routing layer. In this work, the target layer can be Layer 3, Layer 7, or Layer 15. The impedance Z_{s} is defined as the source-side impedance at the package ball.

The intermediate impedance Z_{x} is defined at the connection point between the pad edge of the microvia on the target layer and the impedance transformer. More specifically, Z_{x} represents the impedance looking toward the source side from this point. Since the vertical transition length of the microvia structure varies when the signal transitions from the top layer to Layer 3, Layer 7, and Layer 15, three different values of Z_{x} can be obtained for the three transition cases.

It should be noted that the structure considered in this section is different from the broadband differential-line structures analyzed in the other sections. The earlier differential interconnect models are intended for high-speed broadband applications. For a 224-Gbps PAM4 link, the corresponding symbol rate is 112 GBaud, resulting in a Nyquist frequency of 56 GHz. Therefore, to fully capture the channel behavior up to the Nyquist frequency while providing a small frequency margin, the broadband differential-line simulations are performed over the frequency range of 0–60 GHz. And therefore a 0–60 GHz frequency range is used throughout the broadband differential-line simulations [36, 37]. In contrast, the purpose of this section is to investigate how different microvia geometries influence the RF design of an impedance transformer and the resulting impedance-matching behavior. If the same broadband 0–60 GHz differential-line configuration were used for this impedance-transformer study, the required matching network would become significantly larger and would likely require a special or multi-section implementation. Therefore, a narrower-band application around 24–28 GHz is considered, and the frequency range is limited to 20–30 GHz in the corresponding S-parameter results. Hence, this section should be regarded as an additional case study showing the sensitivity of impedance matching to microvia geometry, rather than a direct comparison with the previous broadband differential-line structures.

Based on transmission-line theory and the impedance-matching principle, impedance transformers with different physical dimensions are designed for different target layers. The purpose of the impedance transformer is to match the intermediate impedance Z_{x} to the target load impedance Z_{L}. The matching design is performed at the center frequency of the target frequency band from 24.25 GHz to 27.5 GHz, namely 25.88 GHz. By introducing the impedance transformer, the impedance discontinuity between the microvia transition and the target transmission line can be reduced, thereby improving the signal transmission performance within the desired frequency band. Although the impedance transformer can be designed according to conventional transmission-line theory, the accuracy of the matching result strongly depends on the accuracy of the extracted intermediate impedance Z_{x}. If the microvia transition is not modeled accurately, the extracted impedance may deviate from the actual value, and the designed transformer may no longer provide the expected matching performance. For this reason, the influence of the microvia geometric model on Z_{x} is first evaluated using the Smith chart.

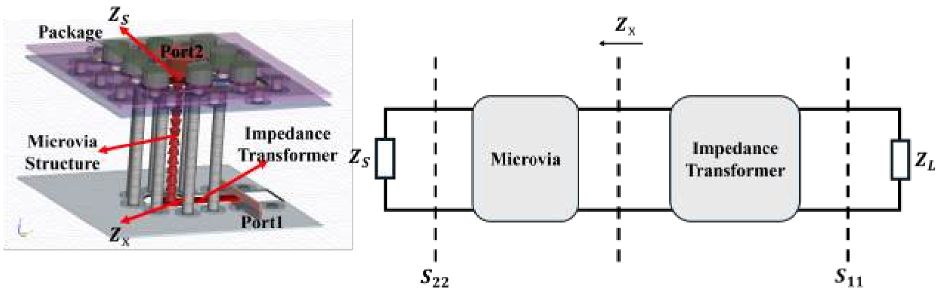

Figure 3.12: Microvia transition structure and its equivalent impedance-matching model.

After the general design procedure of the microvia transition and impedance transformer has been introduced, it is important to further examine the accuracy of the extracted intermediate impedance Z_{x}. In practical high-speed interconnect design, the layer transition structure is essential for routing signals from the package side to the target signal layer. However, even after the impedance transformer is designed, the final transmission performance may still be degraded in practical measurements or simulations. This degradation can be caused by impedance mismatch, parasitic discontinuities, additional reflection, mode conversion, or manufacturing-related geometric variations. Among these factors, the geometric representation of the microvia is particularly important, because it directly affects the local electromagnetic field distribution and the extracted impedance used for the impedance-matching design.

Therefore, before designing the impedance transformer, the influence of different microvia geometric models on the extracted intermediate impedance Z_{x} is investigated. Fig. 3.13 shows the simulated intermediate impedance Z_{x} on the Smith chart for three target-layer transition cases. The corresponding marker information on the Smith chart is summarized in Table 3.3. The impedance is extracted at the connection point between the microvia pad edge on the target layer and the impedance transformer, looking toward the source side. The comparison is performed over the target frequency range of 24.25–27.5 GHz, with the marker values shown at the center frequency of 25.88 GHz. In the Fig. 3.13, the green curves correspond to the transition from the top layer to Layer 3, the blue curves correspond to the transition from the top layer to Layer 7, and the red curves correspond to the transition from the top layer to Layer 15. For each target layer, the reference polygonal cylindrical microvia model and the conical microvia model are compared.

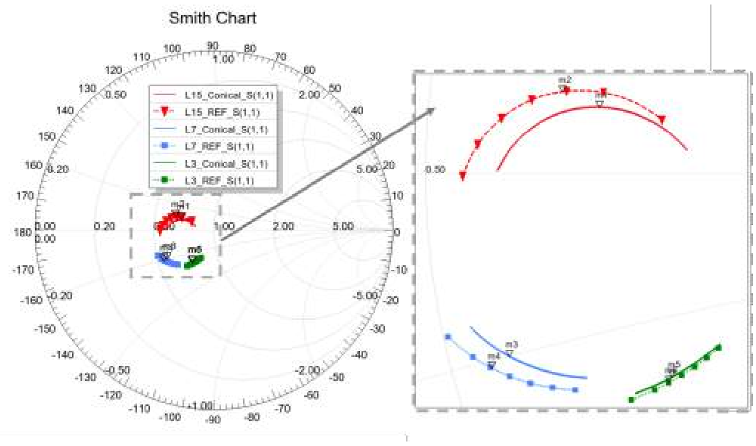

Figure 3.13: Normalized impedance Z_x on the Smith chart for the L3, L7, and L15 transitions. The solid lines denote the conical microvia models, whereas the dotted lines denote the corresponding cylindrical reference models.

Table 3.3: Marker Information

Name	Description	Freq. [GHz]	Ang.	Mag.	RX
m1	L15 Conical	25.88	161.8605	0.1882	$0.6924 + 0.0841i$
m2	L15 Ref.	25.88	161.0993	0.2236	$0.6449 + 0.0983i$
m3	L7 Conical	25.88	−147.9560	0.3049	$0.5634 - 0.2010i$
m4	L7 Ref.	25.88	−147.8781	0.3237	$0.5416 - 0.2082i$
m5	L3 Conical	25.88	−122.5013	0.2128	$0.7495 - 0.2817i$
m6	L3 Ref.	25.88	−122.3914	0.2183	$0.7431 - 0.2877i$

For the Layer 3 case, the vertical transition path is the shortest among the three cases. As a result, the impedance trajectories obtained from the cylindrical and conical microvia models are very close to each other on the Smith chart. This indicates that when the microvia transition length is relatively short, the influence of the microvia geometric representation on the extracted Z_x is limited. For the Layer 7 case, a more visible displacement between the two impedance trajectories can be observed. For the Layer 15 case, where the signal travels through the longest vertical microvia transition, the difference between the cylindrical and conical models becomes the most significant. This trend indicates that the influence of the microvia geometric model increases as the number of crossed layers and the total microvia transition length increase. In other words, for a short layer transition, the simplified polygonal cylindrical model can provide a similar impedance prediction to the conical model. However, for longer transitions, the accumulated effect of the microvia geometry becomes more pronounced, leading to a noticeable shift of Z_x on the Smith chart.

Such an impedance shift is important for the subsequent impedance transformer design. Since the transformer dimensions are determined based on the extracted intermediate impedance Z_x, any deviation in Z_x may result in a mismatch between the microvia transition and the output transmission line. This mismatch can further affect the output-port impedance, increase the return loss, and degrade the overall signal transmission performance. Therefore, for longer microvia transitions, using a more realistic conical microvia model is necessary to obtain a more accurate impedance extraction and a more reliable impedance-matching design.

The marker values at 25.88 GHz further confirm this difference. For the Layer 15 transition, the normalized impedance changes from approximately $0.6449+j0.0983$ in the reference model to $0.6924+j0.0841$ in the conical model. For the Layer 7 transition, the impedance changes from approximately $0.5416-j0.2082$ to $0.5634-j0.2010$. For the Layer 3 transition, the impedance changes from approximately $0.7431-j0.2877$ to $0.7495-j0.2817$. Although the difference is not extremely large, it is still significant for impedance-matching design at millimeter-wave frequencies, because the transformer dimensions are determined based on the extracted impedance point.

In summary, the Smith chart comparison demonstrates that the microvia geometric model can introduce a noticeable deviation in the extracted intermediate impedance Z_x. Since Z_x is the starting point for the subsequent impedance transformer design, an inaccurate microvia model may lead to a non-ideal matching result, increased reflection, and degraded transmission performance. Therefore, using a more realistic conical microvia geometry is important for improving the reliability of the simulation-based design flow, especially when the structure operates in the 24.25–27.5 GHz frequency band.

The return-loss results further confirm this trend, as shown in Fig. 3.14. For the Layer 3 transition, the conical and cylindrical models show very similar responses. For the Layer 7 transition, a visible difference appears around the impedance-sensitive frequency region near 25.875 GHz. For the Layer 15 transition, the difference becomes more pronounced, indicating that the longer vertical transition is more sensitive to the microvia geometry.

Therefore, the influence of the microvia vertical geometry is strongly dependent on the transition length. The cylindrical model can be used as a reasonable approximation for short transitions, but it may not accurately capture the impedance behavior of long microvia transitions. For deep-layer routing and high-frequency applications, the conical microvia model provides a more realistic representation of the physical structure and should be considered in the signal-integrity analysis.

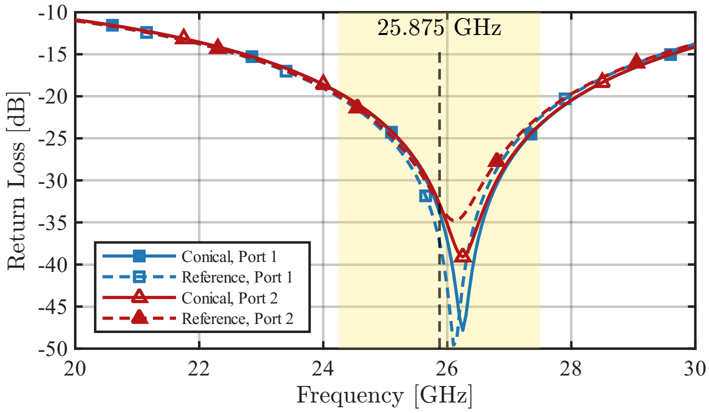

(a) TOP to Layer 3

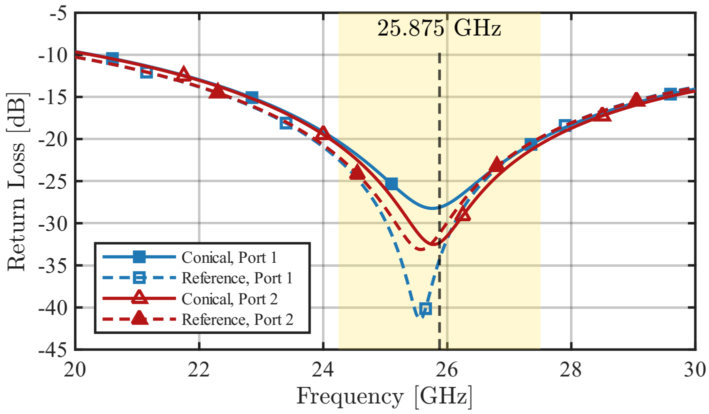

(b) TOP to Layer 7

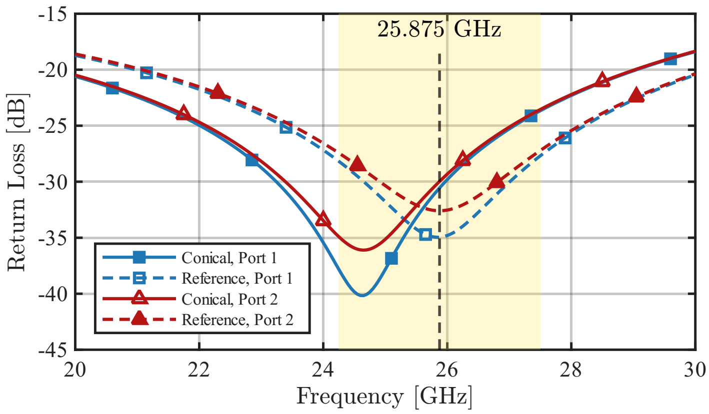

(c) TOP to Layer 15

Figure 3.14: Return loss of the transition structures from TOP Layer to different target layers: (a) Layer 3, (b) Layer 7, and (c) Layer 15.

3.6 Impact of Microvia Geometry on Isolation

3.6.1 Geometric Models of Cylindrical and Conical Microvias

To investigate the influence of microvia geometry on the isolation performance, a simulation model containing two differential pairs is established, as shown in Fig. 3.15. The first differential pair is defined as the aggressor channel, while the second differential pair is defined as the victim channel to evaluate the coupling level. In this structure, two types of differential isolation are considered. The first one is the coupling between different layers, represented by S_{dd31}, where the coupled signal is observed at the differential port located on a different layer from the driven port. The second one is the coupling at the same layer, represented by S_{dd32}, where the coupled signal is observed at the differential port located on the same layer. These two quantities are used to evaluate how the microvia transition affects the isolation between adjacent differential channels in both vertical and lateral directions. In this study, only the longest via transition, namely the L3–L15 transition, is considered, because it has the largest vertical discontinuity and is expected to show the strongest sensitivity to microvia geometry.

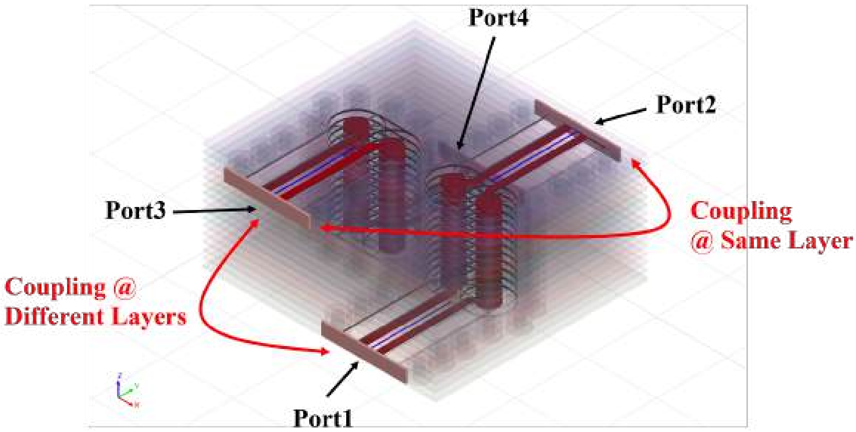

Figure 3.15: Simulation model with two differential pairs for evaluating coupling between the same layer and different layers.

For the same simulation structure, three different microvia geometry models are compared, as illustrated in Fig. 3.16: a large cylindrical model, a conical model, and a small cylindrical model. In the conical model, all signal and ground vias are modeled as conical structures. In the two cylindrical reference models, the diameters of both signal and ground vias are changed consistently. The large cylindrical diameter is equal to the larger diameter of the conical microvia, while the small cylindrical diameter is equal to the smaller diameter of the conical microvia. Therefore, the conical microvia model represents a tapered transition between the two cylindrical reference cases. The simulated S_{dd31} and S_{dd32} responses are then compared to evaluate the influence of vertical microvia geometry on the isolation performance.

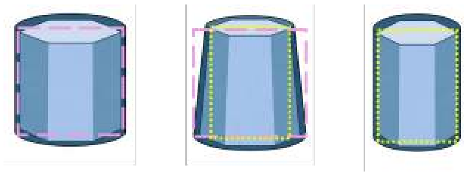

Figure 3.16: Comparison of three microvia geometry models: large cylindrical microvia, conical microvia, and small cylindrical microvia.

3.6.2 S-Parameter Comparison of Isolation Performance

Fig. 3.17 shows the differential coupling results of the L3–L15 transition structure with different microvia geometry models.

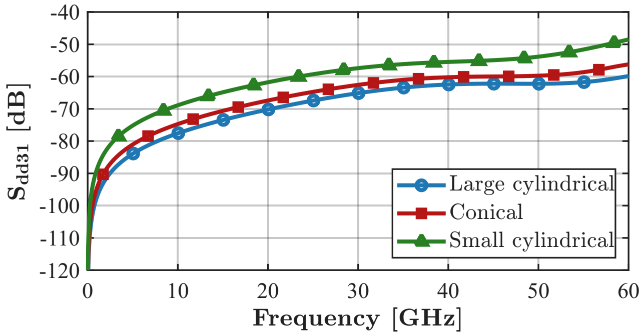

(a) Differential coupling between different layers, S_{dd31}.

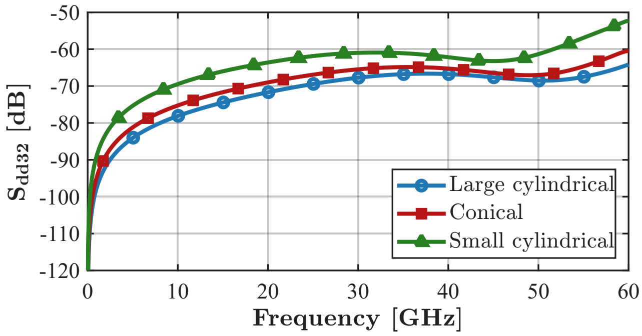

(b) Differential coupling at the same layer, S_{dd32}.

Figure 3.17: Comparison of the differential coupling for the L3–L15 transition structure using different microvia geometry models.

For the different-layer coupling S_{dd31}, all three models show an increasing coupling level as the frequency increases. The separation among the three curves can already be observed at very low frequencies and remains relatively consistent over most of the frequency range. The large cylindrical microvia gives the lowest coupling, corresponding to the best isolation, whereas the small cylindrical microvia produces the highest coupling. The conical microvia remains between these two cylindrical models, which is consistent with its geometrical relationship to the large and small cylindrical references.

The same-layer coupling S_{dd32} follows the same ordering as S_{dd31}: the large cylindrical model gives the lowest coupling, the small cylindrical model gives the highest coupling, and the conical model lies between them. This consistency indicates that the effective microvia diameter and vertical geometry influence both coupling paths in the L3–L15 transition.

3.6.3 Electric-Field Distribution and Coupling Visualization

Figure 3.18 shows the electric-field distribution on Layer 3 when Port 3 is excited. The field is mainly concentrated around the excited differential pair of Port 3, where strong red and orange regions can be observed near the signal traces and microvia pads. This indicates that most of the electromagnetic energy is initially confined around the driven port. However, part of the field also spreads laterally across Layer 3 toward the adjacent Port 2 region. Therefore, the field distribution provides a physical visualization of the same-layer coupling path from Port 3 to Port 2, corresponding to S_{dd32}.

The field response around Port 2 is especially important for evaluating the coupling level. Since Port 2 is not directly excited in this case, any visible electric-field concentration around the Port 2 traces or microvia region is caused by the coupled energy from Port 3. At low frequencies, the field around Port 2 is relatively weak, indicating limited same-layer coupling. As the frequency increases, especially at 55 GHz, the field becomes more distributed over the layer, and stronger field variations can be observed between the two differential ports. This suggests that the discontinuities associated with pads, antipads, reference-plane openings, and microvia transitions become more significant at high frequency, leading to increased field leakage and stronger same-layer coupling.

The comparison among the three microvia geometries also shows that the local field distribution is affected by the effective microvia shape and diameter. The large cylindrical model exhibits stronger field confinement around the excited port and relatively weaker field spreading toward Port 2, which is consistent with its lower coupling level. The small cylindrical model shows a more pronounced field extension over the layer, indicating stronger interaction between the two same-layer ports. The conical microvia model generally shows an intermediate behavior between the two cylindrical models. This is reasonable because the tapered geometry changes the local capacitance and field concentration around the microvia transition compared with a uniform cylindrical approximation.

Overall, Fig. 3.18 confirms that the same-layer coupling is not only determined by the spacing between the two ports, but also by the microvia geometry and the frequency-dependent field distribution on the signal layer. At higher frequencies, the field is less localized around the excited port and the coupling path toward the adjacent port becomes more visible. This explains why different microvia geometry models can lead to different predicted values of

S_{dd32} and highlights the importance of using an appropriate microvia model in high-frequency signal-integrity simulations.

Figure 3.19 shows the electric-field distribution on Layer 15 when Port 3 on Layer 3 is excited. In this view, the upper-left differential pair corresponds to Port 4, which is directly connected to the excited Port 3 through the vertical transition, while the lower-right differential pair corresponds to Port 1, which is connected to Port 2 in the adjacent transition. Therefore, this figure is used to visualize the different-layer coupling path from Port 3 to Port 1, corresponding to S_{dd31}.

The strongest electric field is mainly observed around the Port 4 region, indicating that most of the energy is transferred through the intended vertical transition connected to Port 3. The field appearing around the Port 1 region represents the coupled energy through the neighboring transition. At 0.1 GHz and 1 GHz, the field distribution is relatively weak and the response around Port 1 is limited. At 55 GHz, the field becomes more distributed over Layer 15, and the coupling path toward Port 1 becomes more visible, showing that high-frequency discontinuities and inter-via interactions increase the different-layer coupling.

The comparison among the large cylindrical, conical, and small cylindrical microvia models shows that the microvia geometry affects the field confinement around the intended transition and the leakage toward the adjacent transition. The large cylindrical model generally provides better field confinement, the small cylindrical model shows stronger field spreading, and the conical model exhibits an intermediate behavior. These results support that the predicted S_{dd31} is sensitive to the effective microvia geometry, especially at high frequencies.

3.6.4 Discussion on Geometry-Dependent Coupling Mechanisms

To further evaluate the field leakage mechanism, the radiation-related loss is estimated from the simulated S-parameters. Following the method discussed in [38], the total loss can be interpreted as the percentage of the input power that is not preserved in the desired differential transmission path. In general, this loss consists of conductor loss, dielectric loss, and radiation loss, which can be written as

$$\eta_{\mathrm{loss}} = \eta_{\mathrm{c}} + \eta_{\mathrm{D}} + \eta_{\mathrm{rad}}, \tag{3.7}$$

where η_{c}, η_{D}, and η_{rad} denote the percentages of the input power lost due to conductor loss, dielectric loss, and radiation into the surrounding cavity, respectively. The quantity of them are all dimensionless; when multiplied by 100, they represent the percentage of the input differential-mode power.

In this work, the radiation-related loss is estimated from the power balance of the mixed-mode S-parameters. For a differential excitation, the estimated loss percentage can be expressed as

$$\eta_{\mathrm{rad,est}} \approx 100\% \left[1 - \left(|S_{\mathrm{dd11}}|^2 + |S_{\mathrm{dd21}}|^2 + |S_{\mathrm{cd11}}|^2 + |S_{\mathrm{cd21}}|^2\right)\right]. \tag{3.8}$$

Here, S_{dd11} and S_{dd21} represent the differential-mode reflection and transmission coefficients, while S_{cd11} and S_{cd21} represent the differential-to-common-mode conversion terms. Since the differential-to-common-mode conversion terms are

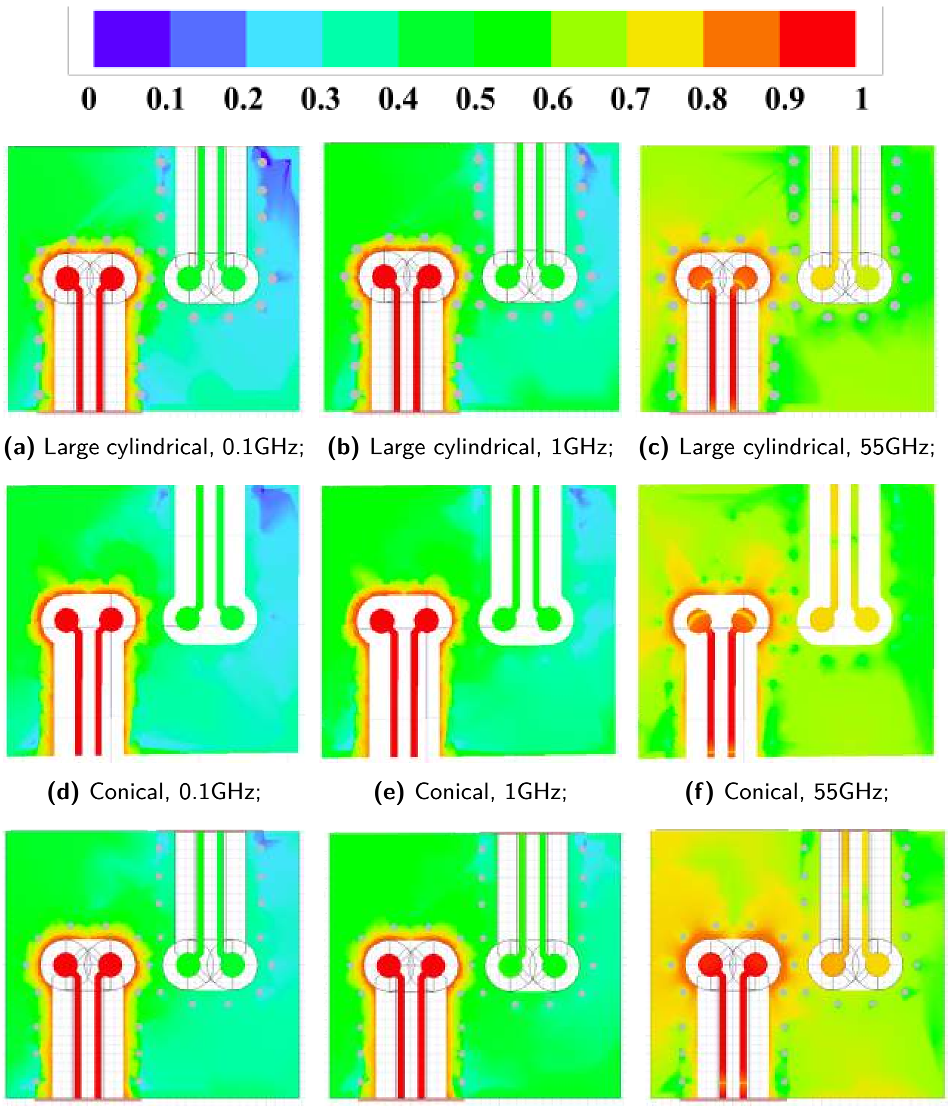

(a) Large cylindrical, 0.1GHz; **(b)** Large cylindrical, 1GHz; **(c)** Large cylindrical, 55GHz;

(d) Conical, 0.1GHz; **(e)** Conical, 1GHz; **(f)** Conical, 55GHz;

(g) Small cylindrical, 0.1GHz; **(h)** Small cylindrical, 1GHz; **(i)** Small cylindrical, 55GHz;

Figure 3.18: Electric-field distribution on Layer 3 when Port 3 (at Layer 3) is excited. The figure is used to evaluate the same-layer coupling from Port 3 to Port 2, corresponding to S_{32}.

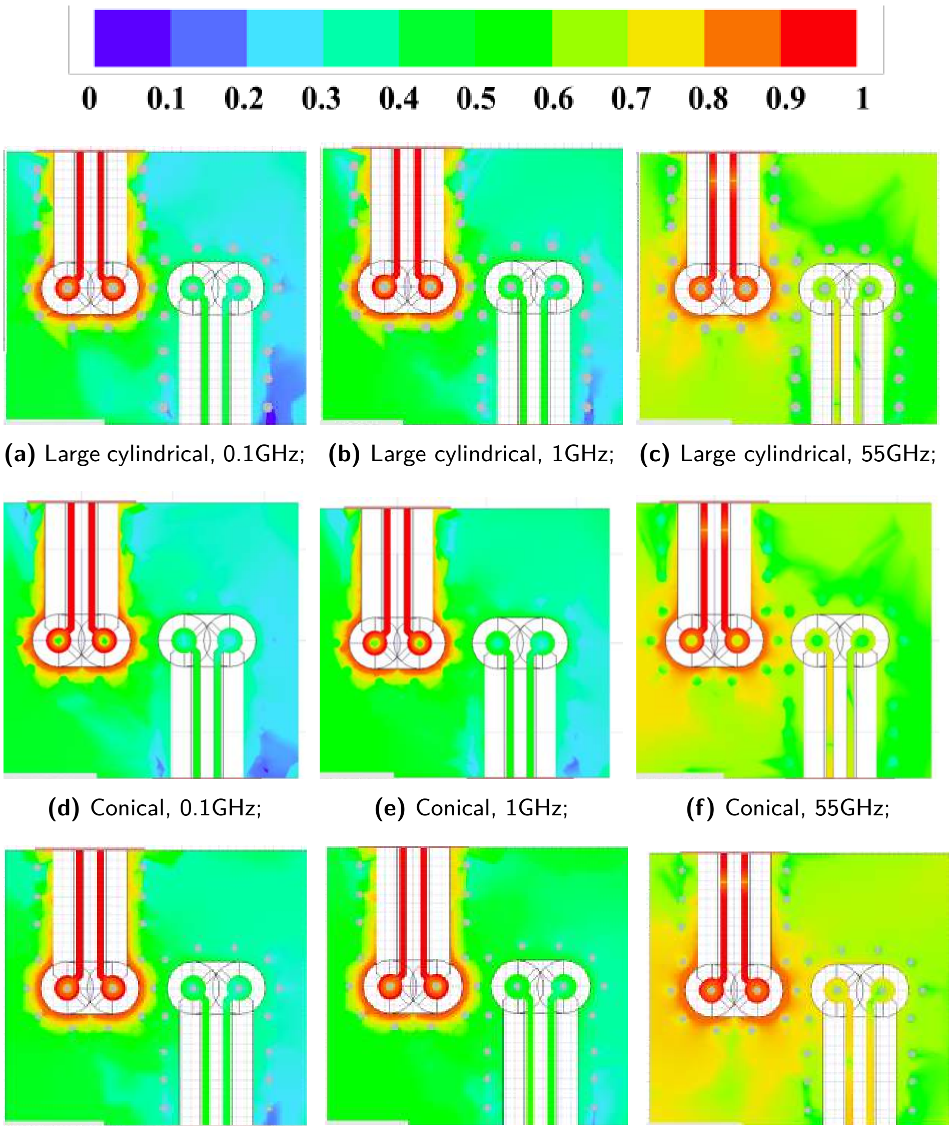

(a) Large cylindrical, 0.1GHz; **(b)** Large cylindrical, 1GHz; **(c)** Large cylindrical, 55GHz;

(d) Conical, 0.1GHz; **(e)** Conical, 1GHz; **(f)** Conical, 55GHz;

(g) Small cylindrical, 0.1GHz; **(h)** Small cylindrical, 1GHz; **(i)** Small cylindrical, 55GHz;

Figure 3.19: Electric-field distribution on Layer 15 when Port 3 (at Layer 3) is excited. The figure is used to evaluate the different-layer coupling from Port 3 to Port 1, corresponding to S_{31}.

much smaller than the dominant differential-mode reflection and transmission terms in this simulation, S_{cd11} and S_{cd21} are neglected in the loss estimation. Therefore, the estimated loss percentage is simplified as

$$\eta_{\mathrm{loss,est}} \approx 100\% \left[1 - \left(|S_{\mathrm{dd11}}|^2 + |S_{\mathrm{dd21}}|^2\right)\right]. \tag{3.9}$$

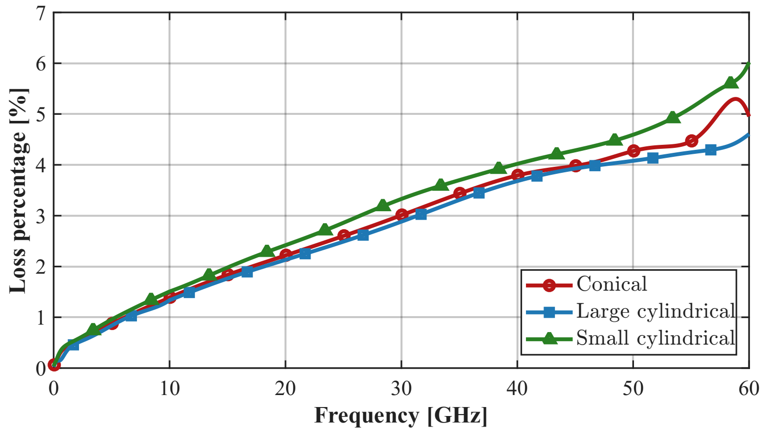

Figure 3.20: Estimated radiation-related loss percentage for the L3–L15 transition structure using different microvia geometry models.

As shown in Fig. 3.20, the estimated loss also varies with the microvia geometry model. Since the material properties, stackup, and other geometrical parameters are kept unchanged in this comparison, the difference among the curves is mainly attributed to the change in microvia geometry. It should be noted that this loss difference is not only associated with radiation-related field leakage, but may also include changes in dielectric loss, conductor loss, and mismatch behavior. Therefore, the conical microvia model affects not only the local port impedance and transmission response, but also the overall energy distribution around the via transition and the adjacent interconnect region.

Since the conical microvia model better represents the physical fabricated shape, it can provide a more realistic estimation of the total loss and, consequently, a more accurate prediction of the isolation performance. Therefore, for high-frequency and long-layer-transition structures, the conical model is more suitable than the ideal cylindrical approximation for evaluating coupling, crosstalk, and isolation.

3.7 Summary

This chapter investigated the influence of microvia vertical geometry on the signal-integrity performance of differential via transitions. The conventional polygonal cylindrical model was first used to establish baseline designs by sweeping the antipad size for different transition lengths. The results show that the short

L3–L7 transition is relatively stable, while the longer L3–L9 and L3–L15 transitions are more sensitive to antipad size, especially at high frequencies. This is because longer transitions accumulate stronger parasitic effects and are more affected by changes in the local capacitance, inductance, and return-current path.

The cylindrical and conical microvia models were then compared. For the short L3–L7 transition, the difference between the two models is small, indicating that the cylindrical approximation is acceptable when the vertical transition length is short. However, for the longer L3–L15 transition, the conical geometry produces clearer changes in return loss, TDR impedance, and the extracted intermediate impedance Z_{x}. These results show that the tapered microvia profile changes the local parasitic behavior of the transition and becomes more important for deep-layer and high-frequency interconnects.

The isolation analysis also shows that the microvia geometry affects the predicted coupling between adjacent differential channels. The conical model generally gives an intermediate coupling level between the large and small cylindrical reference models, and the electric-field distributions confirm that different geometries lead to different field confinement and leakage behavior. Therefore, using a conical microvia model can provide a more reliable prediction of coupling, radiation-related loss, and isolation performance.

Overall, the results show that the impact of microvia vertical geometry becomes more significant as the transition length and operating frequency increase. The cylindrical model is efficient and acceptable for short transitions, but the conical model is more suitable for long and high-frequency transitions. Considering the high computational cost of modeling all vias as conical structures, applying the conical geometry mainly to the signal microvias provides a practical compromise between simulation accuracy and efficiency.

Chapter 4

Impact of Manufacturing-Induced Staggering on Signal Integrity

4.1 Introduction

In the previous chapters, the microvia transition structures were mainly analyzed under ideal alignment conditions. However, in practical HDI manufacturing, the fabricated geometry may deviate from the nominal design due to process tolerances. These deviations can change the relative positions between microvias, pads, antipads, and routing traces, thereby modifying the local electromagnetic environment of the differential pair. As a result, the impedance continuity, differential-mode transmission, mode conversion, and coupling behavior of the interconnect may be affected.

In this chapter, the impact of manufacturing-induced staggering on the SI performance of differential microvia transitions is investigated. Two major types of misalignment are considered. The first type is hole misalignment, where the drilled microvia position is shifted with respect to its designed location while the surrounding metal patterns remain unchanged. This type of deviation is commonly associated with laser drilling accuracy in HDI fabrication. The second type is layer misalignment, where one or more PCB layers are shifted as a whole due to imperfect layer registration during multilayer lamination. In this case, the metal features on the shifted layer, such as pads, traces, and antipads, move together relative to the other layers.

Although hole misalignment and layer misalignment are treated separately in the following analysis for clarity, they may occur simultaneously in practical fabrication. For example, an inner layer may already be shifted during lamination, while the subsequent laser-drilled microvia may also deviate from its target position. The final fabricated structure is therefore determined by the combined effect of different tolerance sources. Separating these two mechanisms makes it possible to identify their individual contributions to SI performance degradation before considering more realistic random tolerance combinations.

The analysis in this chapter is carried out in two steps. First, several representative misalignment cases are simulated to reveal the physical influence of specific offset directions and magnitudes. These deterministic cases are useful for identifying critical misalignment scenarios and explaining how the broken geometrical symmetry affects the differential response. Then, a Monte Carlo analysis is performed to emulate the random nature of manufacturing tolerances. By statistically evaluating the variation of S-parameters and impedance responses, the robustness of the proposed microvia transition structures against fabrication-induced staggering can be assessed.

4.2 Hole Misalignment

Hole misalignment is especially important for laser-drilled microvias. Compared with conventional mechanically drilled vias, microvias have much smaller dimensions and rely strongly on optical registration during fabrication. Therefore, the available tolerance margin is limited. In stacked microvia structures, the misalignment between adjacent microvias can further accumulate, leading to imperfect vertical alignment along the signal transition path. This may introduce local impedance discontinuities, increase mode conversion, and degrade the SI performance of differential interconnects.

In this section, the impact of hole misalignment is investigated from two perspectives. First, several special misalignment cases are analyzed to clarify how different deterministic offset directions affect the differential microvia transition. Then, a Monte Carlo analysis is performed to evaluate the statistical influence of random hole-position variations caused by manufacturing tolerances.

4.2.1 Special Case Analysis

To investigate the impact of hole misalignment, several representative special cases are first considered before the statistical analysis. According to the direction of the hole offset, the misalignment cases are divided into two main groups: misalignment along the x-direction and misalignment along the y-direction. For each group, three specific cases are further defined according to the differential-pair symmetry and the orientation and sequence of the x- or y-direction hole offsets, namely X1, X2, and X-asymmetric for the x-direction group, and Y1, Y2, and Y-asymmetric for the y-direction group. In all special cases, the offset Δx_i and Δy_i is equal to 75 um. Therefore, this represents a critical state, where the larger circular edge of the tapered microvia hole with the offset is close to the edge of the pad.

In all the simulated models, the differential signal microvias are modeled using the conical microvia geometry, while the ground vias are modeled using the polygonal cylindrical geometry. The other structures remain unchanged, so that the effect of signal-hole displacement can be isolated.

4.2.1.1 x-direction hole misalignment cases.

Fig. 4.1 and Fig. 4.2 illustrate the x-direction hole-misalignment configurations considered for the differential signal microvias. The original structure without any hole offset is used as the reference case, denoted as REF. According to the differential-pair symmetry and the orientation and sequence of the lateral hole offsets, three misalignment cases are defined: X1, X2, and X-asymmetric, where X2 is the mirror configuration of X1.

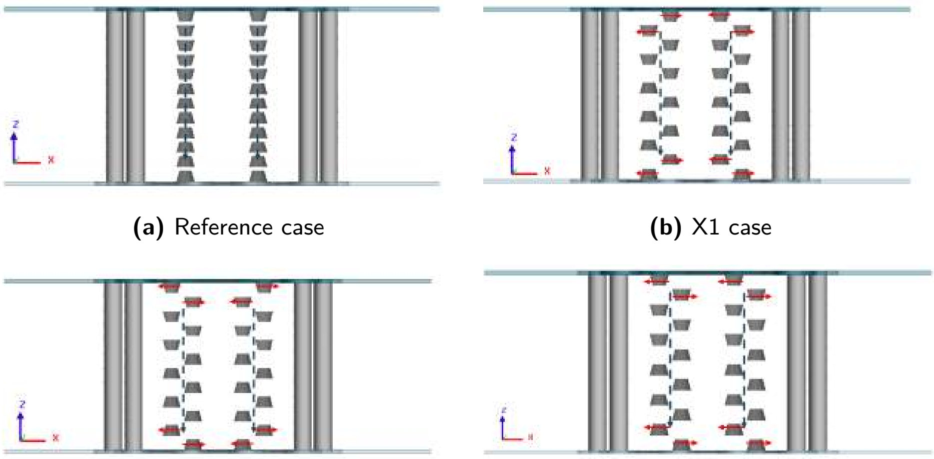

(a) Reference case

(b) X1 case

(c) X2 case, mirror of X1

(d) X-asymmetric case

Figure 4.1: Front-view cross sections of the x-direction hole misalignment cases. The ground layers are hidden for clarity. The dark-blue dashed lines indicate the original center positions of the stacked signal microvias from layer 3 to layer 15. The red arrows mark the hole offsets along the x-direction.

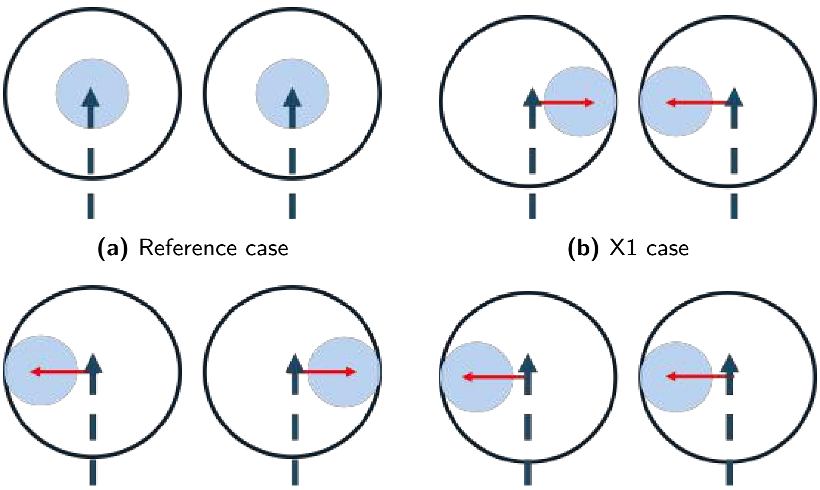

(a) Reference case

(b) X1 case

(c) X2 case, mirror of X1

(d) X-asymmetric case

Figure 4.2: Top-view illustration of the x-direction hole misalignment cases on Layer 3. The red arrows indicate the hole-offset directions on this Layer, while the blue dashed arrows indicate the routing direction of the differential transmission lines that fan in to the signal microvias.

Fig. 4.1 shows the corresponding front-view cross sections of the complete PCB transition, where the ground layers are hidden for clarity. The coordinate axes shown in the lower-left corner are from the HFSS model, where the red axis denotes the x-direction. In this view, the signal microvias are modeled using the tapered conical geometry, whereas the surrounding ground microvias are modeled using the cylindrical geometry. The dark-blue dashed lines indicate the original center positions of the stacked signal microvias from layer 3 to layer 15 in the transition structure. The red arrows mark the hole offsets along the x-direction. Therefore, this front-view figure directly shows how the x-direction hole misalignment changes the originally vertical stacked transition into laterally shifted or zigzag-like signal paths.

Fig. 4.2 gives the top-view illustrations on layer 3. In this section, only the hole misalignment of the differential signal microvias is considered. Therefore, each subfigure shows one pair of differential signal microvias. The small light-blue filled circles represent the actual hole positions, while the larger dark-blue empty circles represent the corresponding pads. In the reference case without hole misalignment, the hole and pad are concentric. When hole misalignment is introduced, the hole center is laterally shifted away from the pad center. The red arrows indicate the hole-offset directions, while the blue dashed arrows indicate the routing direction of the differential transmission lines that fan in to the signal microvias. Since the hole displacement is applied along the x-direction, the offset direction is perpendicular to the signal-propagation direction in these cases.

These two figures are used together to describe both the hole-to-pad offset in the top view and the resulting vertical transition path in the front cross-sectional view.

Reference case The Reference case is shown in Fig. 4.1(a) and Fig. 4.2(a). In this reference structure, no hole misalignment is introduced. The center of each signal microvia is aligned with the center of its corresponding pad in the top view. From the cross-sectional view, the microvias are vertically aligned from layer 3 to layer 15, forming an ideal stacked transition path.

X1 case The X1 case is shown in Fig. 4.1(b) and Fig. 4.2(b). In the top view, the hole centers of the two differential signal microvias on the same layer are shifted in opposite x-directions with respect to their fixed pad centers. More specifically, each hole center is shifted toward the other signal microvia, so that the two signal holes move closer to each other on layer 3. As a result, the spacing between the two signal-hole centers is reduced compared with the reference case. From the front-view cross section, the lateral offset direction alternates along the vertical stack, forming a zigzag-like signal transition path. Although the hole centers are no longer aligned with the pad centers, the opposite offset directions help preserve the overall differential symmetry to some extent.

X2 case The X2 case, shown in Fig. 4.1(c) and Fig. 4.2(c), is the mirror case of X1. Similar to X1, the hole centers of the two differential signal microvias on the same layer are shifted in opposite x-directions with respect to their fixed pad centers. However, in this case, the two hole centers are shifted away from each other, so that the spacing between the signal holes on layer 3 is increased compared with the reference case. Thus, the differential-pair symmetry is still largely maintained, but the relative spacing between the two signal-hole centers is changed in the opposite manner to X1. From the front-view cross section, the lateral offset direction alternates along the vertical stack, forming a zigzag-like signal transition path. Therefore, comparing X1 and X2 can be used to evaluate whether the electromagnetic response is sensitive to the mirrored sequence of the lateral hole offsets along the L3–L15 transition.

X-asymmetric case The X-asymmetric case is shown in Fig. 4.1(d) and Fig. 4.2(d). In this case, the hole centers of the two differential signal microvias on the same layer are shifted in the same x-direction with respect to their fixed pad centers. Therefore, the spacing between the two signal-hole centers on the same layer remains the same as that in the reference case. Unlike X1 and X2, this offset configuration breaks the lateral symmetry of the differential transition and may introduce an imbalance between the two signal paths. This case is therefore used to examine the effect of differential-pair asymmetry on the signal-integrity response of the transition.

From the cross-sectional views in Fig. 4.1, all three x-direction misalignment cases change the originally vertical transition path of each signal microvia into a zigzag-like path. This is because the x-direction hole offset alternates between adjacent layers along the vertical stack. Since the same offset magnitude is applied, the additional geometrical path length introduced by the lateral displacement is similar among the 3 cases. However, their electromagnetic responses can still be different because the relative positions between the two signal microvias, the pads, and the surrounding reference structures are different. Therefore, these special cases are useful for separating the effects of offset direction and differential-pair symmetry.

4.2.1.2 y-direction hole misalignment cases.

Fig. 4.3 and Fig. 4.4 illustrate the y-direction hole-misalignment configurations considered for the differential signal microvias. The original structure without any hole offset is used as the reference case, denoted as REF. According to the differential-pair symmetry and the orientation and sequence of the y-direction hole offsets, three misalignment cases are defined: Y1, Y2, and Y-asymmetric, where Y2 is the mirror configuration of Y1.

Fig. 4.3 shows the corresponding three-dimensional dimetric views of the complete PCB transition, where the ground layers are hidden for clarity. The coordinate axes shown in the lower-left corner are from the HFSS model. In this view, the signal microvias are modeled using the tapered conical geometry, whereas the surrounding ground microvias are modeled using the cylindrical geometry. The dark-blue dashed lines indicate the original center positions of the stacked signal microvias from layer 3 to layer 15 in the transition structure. The dark-blue solid lines indicate the fan-in and fan-out routing directions on layers 3 and 15, respectively. The green arrows mark the hole offsets along the y-direction. Compared with the x-direction cases, the dimetric view is used here to make the

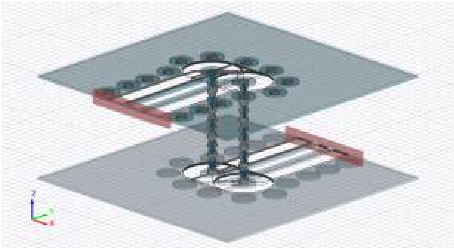

(a) Reference case

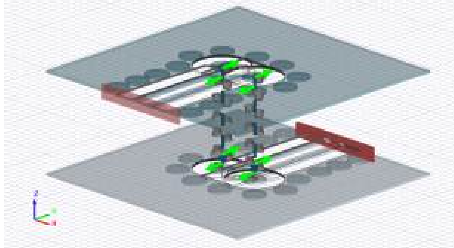

(b) Y1 case

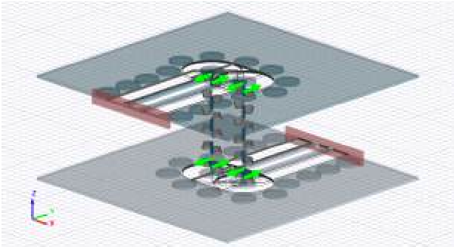

(c) Y2 case

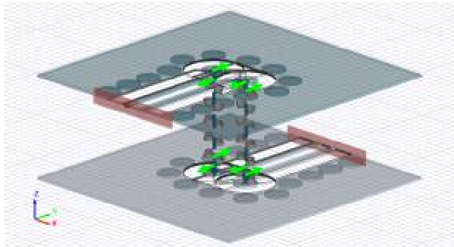

(d) Y-asymmetric case

Figure 4.3: Three-dimensional dimetric views of the y-direction hole misalignment cases. The ground vias and ground layers are hidden for clarity. The dark-blue solid lines show the fan-in and fan-out directions on layers 3 and 15. The green arrows mark the hole offsets along the y-direction.

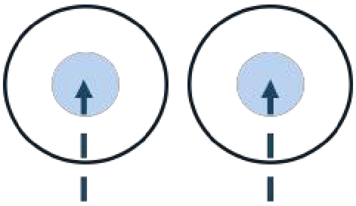

(a) Reference case

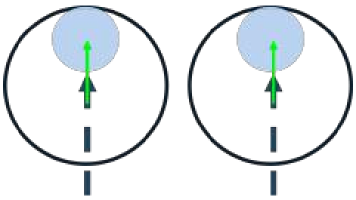

(b) Y1 case

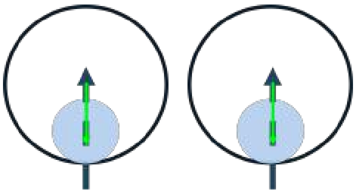

(c) Y2 case

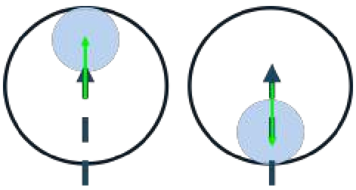

(d) Y-asymmetric case

Figure 4.4: Top-view illustration of the y-direction hole misalignment cases on Layer 3. The red arrows indicate the hole-offset directions on this Layer, while the blue dashed arrows indicate the routing direction of the differential transmission lines that fan in to the signal microvias.

y-direction hole offsets more visible. Therefore, this figure directly shows how the y-direction hole misalignment changes the originally vertical stacked transition into laterally shifted or zigzag-like paths.

Fig. 4.4 gives the top-view illustrations on layer 3. In this section, only the hole misalignment of the differential signal microvias is considered. Therefore, each subfigure shows one pair of differential signal microvias. The small light-blue filled circles represent the actual hole positions, while the larger dark-blue empty circles represent the corresponding pads. In the reference case without hole misalignment, the hole and pad are concentric. When hole misalignment is introduced, the hole center is shifted away from the pad center along the y-direction. The green arrows indicate the hole-offset directions on layer 3, while the blue dashed arrows indicate the routing direction of the differential transmission lines that fan in to the signal microvias. Since the hole displacement is applied along the y-direction, the offset direction is parallel to the routing direction of the fan-in transmission lines feeding the signal microvias.

These two figures are used together to describe both the hole-to-pad offset in the top view and the resulting vertical transition path in the 3D dimetric view.

Reference case The Reference case is shown in Fig. 4.3(a) and Fig. 4.4(a). In this reference structure, no hole misalignment is introduced. The center of each signal microvia's hole is aligned with the center of its corresponding pad in the top view. From the 3D view, the microvias are vertically aligned from layer 3 to layer 15, forming an ideal stacked transition path.

Y1 case The Y1 case is shown in Fig. 4.3(b) and Fig. 4.4(b). In this case, the hole centers of the two differential signal microvias on the same layer are shifted in the same y-direction with respect to their fixed pad centers. Since the offset is applied along the y-direction, the spacing between the two signal-hole centers along the x-direction remains the same as that in the reference case. On layer 3, the hole offsets are in the same direction as the fan-in routing direction. On layer 15, the offset direction is opposite to the fan-out routing direction. From the three-dimensional dimetric view, the y-direction hole offset alternates between adjacent layers along the vertical stack, forming a zigzag-like signal transition path. Because the two signal-hole centers on the same layer are shifted in the same direction, the differential-pair symmetry is still largely preserved.

Y2 case The Y2 case, shown in Fig. 4.3(c) and Fig. 4.4(c), is the mirror case of Y1. Similar to Y1, the hole centers of the two differential signal microvias on the same layer are shifted in the same y-direction with respect to their fixed pad centers. Therefore, the spacing between the two signal-hole centers along the x-direction remains unchanged compared with the reference case. However, the offset direction is reversed compared with Y1. On layer 3, the hole offsets are opposite to the fan-in routing direction, whereas on layer 15, the offset direction is the same as the fan-out routing direction. From the three-dimensional dimetric view, this offset arrangement also forms a zigzag-like signal transition path, because the y-direction hole offset alternates between adjacent layers. Therefore, comparing Y1 and Y2 can be used to evaluate whether the electromagnetic response is sensitive to the mirrored sequence of the y-direction hole offsets along the L3–L15 transition. Since the two signal holes on the same layer are shifted together, the differential-pair symmetry is still largely maintained.

Y-asymmetric case The Y-asymmetric case is shown in Fig. 4.3(d) and Fig. 4.4(d). In this case, the hole centers of the two differential signal microvias on the same layer are shifted in opposite y-directions with respect to their fixed pad centers. On layer 3, one signal hole is shifted forward along the fan-in routing direction, while the other is shifted backward. Although the spacing between the two signal-hole centers along the x-direction remains the same as that in the reference case, their relative positions along the y-direction become different. Unlike Y1 and Y2, this offset configuration breaks the symmetry of the differential pair along the transmission-line direction and may introduce an imbalance between the two signal paths. This case is therefore used to examine the effect of y-direction differential-pair asymmetry on the signal-integrity response of the transition.

From the three-dimensional views in Fig. 4.3, all three y-direction misalignment cases change the originally vertical transition path of each signal microvia into a zigzag-like path. This is because the y-direction hole offset alternates between adjacent layers along the vertical stack. Since the same offset magnitude is applied, the additional geometrical path length introduced by the in-plane displacement is similar among the three cases. However, their electromagnetic responses can still be different because the y-direction offset changes the relative positions between the signal-hole centers, the fixed pads, the fan-in and fan-out transmission lines, and the surrounding reference structures. In particular, Y1 and Y2 preserve the differential-pair symmetry on each layer but have mirrored offset sequences, whereas the Y-asymmetric case breaks the differential-pair symmetry along the transmission-line direction. Therefore, these special cases are useful for separating the effects of offset sequence and differential-pair symmetry for y-direction hole misalignment.

4.2.1.3 Results for hole misalignment.

Fig. 4.5 compares the simulated signal-integrity responses of the special hole-misalignment cases in the x- and y-directions. The conical reference case is used as the main baseline for evaluating the hole-misalignment effect, while the cylindrical reference case is included as an additional reference to compare the relative influence of the nominal microvia geometry.

TDR The TDR responses of the special hole-misalignment cases are shown in Figs. 4.5a and 4.5b. For both the x- and y-direction cases, the differences among the curves are mainly confined to the initial 0–50 ps region, which corresponds to the local microvia transition.

In Fig. 4.5a, the cylindrical reference case shows the deepest initial impedance dip, reaching approximately 75.5 Ω. The conical reference case has a shallower minimum of about 77.5 Ω. In comparison, the three misaligned conical cases, X1, X2, and Xasy, only drop to around 79.5–81 Ω in the same time region. Therefore, the hole offset raises the minimum TDR impedance by roughly 2–3.5 Ω compared

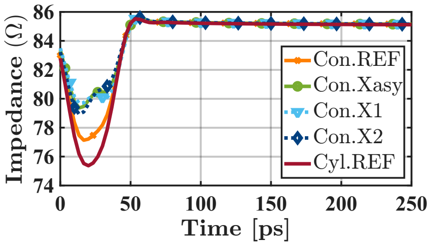

(a) TDR for x-direction cases

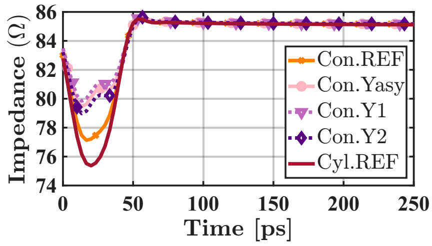

(b) TDR for y-direction cases

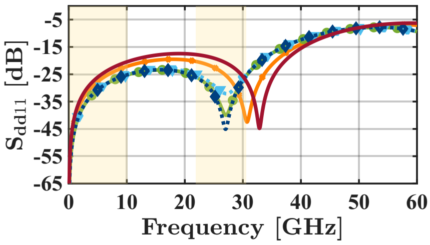

(c) S_{dd11} for x-direction cases

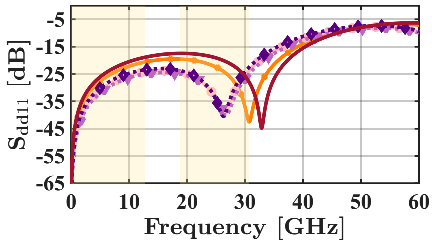

(d) S_{dd11} for y-direction cases

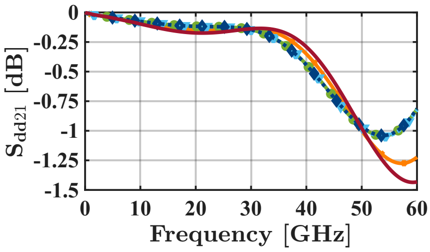

(e) S_{dd21} for x-direction cases

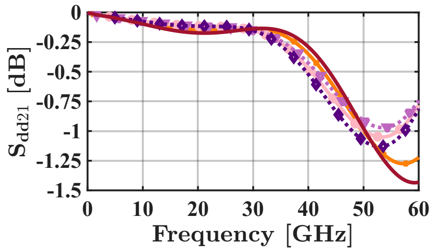

(f) S_{dd21} for y-direction cases

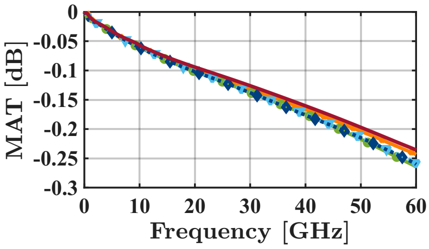

(g) MAT for x-direction cases

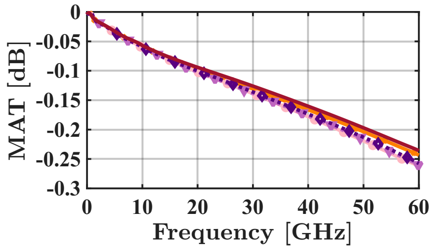

(h) MAT for y-direction cases

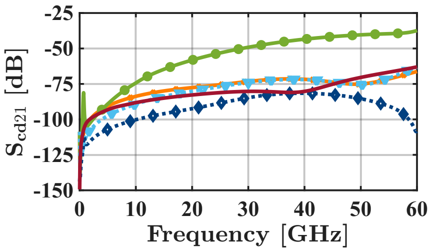

(i) S_{cd21} for x-direction cases

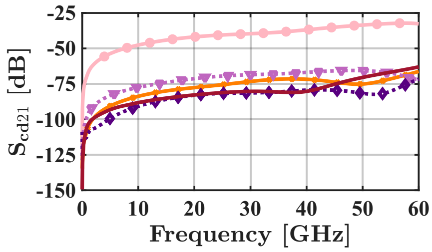

(j) S_{cd21} for y-direction cases

Figure 4.5: Simulated signal-integrity responses of the special hole-misalignment cases in the x- and y-directions.

with the conical reference case, and by about 4–5.5 Ω compared with the cylindrical reference case. The X1 and X2 curves are almost overlapped, and the Xasy curve is also very close to them.

A similar tendency can be observed in Fig. 4.5b. Compared with the x-direction cases, however, the separation among the y-direction curves is slightly more visible. The Y1 and Y2 curves are distributed around the Yasy case, with a difference of approximately 1–2 Ω in the initial 0–50 ps region. This suggests that the TDR response is slightly more sensitive to the y-direction offset than to the x-direction offset.

The shallower impedance dip indicates that the offset slightly shifts the initial TDR response closer to the target differential impedance of 85 Ω. One possible reason is that the displaced microvia introduces a slightly zigzag-like transition path, which increases the effective current path length and may enhance the local inductive contribution. This additional inductive effect can push the local impedance upward and reduce the depth of the initial capacitive dip.

$\boldsymbol{S}_{\mathbf{dd11}}$ The differential return-loss responses of the special hole-misalignment cases are shown in Figs. 4.5c and 4.5d. For both the x- and y-direction cases, the main reflection dip of S_{dd11} shifts toward lower frequencies if with hole misalignment. In the reference cases, the dominant dip appears at approximately 31–32 GHz. After hole misalignment, the dip moves to around 27–28 GHz.

The three misaligned cases in each direction have nearly the same dip frequency. For the x-direction cases in Fig. 4.5c, X1, X2, and Xasy all show the main dip around 27–28 GHz. A similar trend is observed for the y-direction cases in Fig. 4.5d, where Y1, Y2, and Yasy also dip in approximately the same frequency range. This indicates that the dip-frequency shift is mainly caused by a common geometrical change shared by all three misalignment cases, rather than by the detailed offset sequence. The most likely reason is that the hole displacement introduces a zigzag-like microvia transition, which increases the effective current path length and therefore adds local inductance. With a larger effective inductance, the dominant impedance discontinuity is shifted to a lower resonant frequency.

The shaded regions in Figs. 4.5c and 4.5d indicate the frequency ranges where the misaligned cases approximately satisfy $S_{\mathrm{dd11}} < -25$ dB. For the x-direction cases in Fig. 4.5c, this low-reflection region appears in two separate bands: approximately 0–10 GHz and 22–30.5 GHz. For the y-direction cases in Fig. 4.5d, the corresponding shaded regions are slightly wider, covering approximately 0–13 GHz and 19–30.5 GHz. This indicates that the y-direction offset provides a broader frequency range with $S_{\mathrm{dd11}} < -25$ dB than the x-direction offset.

$\boldsymbol{S}_{\mathbf{dd21}}$ The differential insertion-loss responses are shown in Figs. 4.5e and 4.5f. For both the x- and y-direction cases, S_{dd21} exhibits a trend consistent with that of S_{dd11}, as shown in Figs. 4.5c and 4.5d. In particular, two transition points are observed in S_{dd11} at approximately 30 GHz and 50 GHz, respectively. Since S_{dd21} includes both the intrinsic transmission loss and the mismatch caused by the via transition, therefore these variations are closely related to the return-loss behavior. In the frequency regions where S_{dd11} is below approximately -25 dB, the corresponding S_{dd21} curves remain relatively flat and close to 0 dB, indicating that good impedance matching leads to small reflection and low transmission degradation. However, after approximately 40 GHz, S_{dd11} gradually increases, suggesting a stronger mismatch at the via transition. Correspondingly, S_{dd21} starts to decrease more noticeably, which indicates that a larger portion of the incident differential power is not transmitted to the output port.

MAT The corresponding MAT responses are shown in Figs. 4.5g and 4.5h. The MAT metric is used as a mismatch-corrected transmission metric to evaluate the maximum available transmission capability of the interconnect. Compared with S_{dd21}, the MAT curves are much closer to each other, showing that the available transmission capability is only slightly affected by hole misalignment. This is mainly because the misaligned microvias introduce a small additional geometrical path length along the vertical transition. The associated extra loss is weak at low frequencies but becomes more visible at higher frequencies, as transmission loss generally increases with frequency.

The magnified MAT results further show that all misaligned cases have nearly the same MAT response for the same offset magnitude Δx or Δy. This indicates that the slight MAT reduction is primarily caused by the increased path length introduced by the misalignment, rather than by the detailed offset configuration. Therefore, the larger variations observed in S_{dd21} are mainly related to impedance mismatch and local reflection, while the intrinsic available transmission capability is only mildly reduced by the additional path length of the misaligned vias.

S_{cd21} The mode-conversion responses of the special hole-misalignment cases are shown in Figs. 4.5i and 4.5j. Unlike S_{dd11}, S_{dd21}, MAT, and TDR, the S_{cd21} responses show a strong dependence on the specific misalignment configuration. The asymmetric cases, Con.Xasy and Con.Yasy, cause the most significant increase in S_{cd21}, indicating that asymmetric hole misalignment strongly enhances the differential-to-common-mode conversion.

This increase is caused by the imbalance between the two conductors of the differential pair. When the two signal vias experience different local electromagnetic environments, their effective capacitance, inductance, and coupling are no longer identical. Consequently, the differential symmetry is broken, and part of the differential-mode energy is converted into common-mode energy. This also explains why the cases with the same offset magnitude Δx or Δy do not necessarily overlap in the S_{cd21} plots: the mode conversion is governed not only by the offset magnitude, but also by the detailed offset pattern.

Furthermore, the y-direction asymmetric case shows stronger mode conversion than the x-direction asymmetric case at high frequencies. In particular, especially above approximately 40 GHz, the S_{cd21} level of the y-direction asymmetric case is about 5 dB higher than that of the x-direction asymmetric case, as shown in Fig. 4.5j. This indicates that the asymmetric offset along the routing direction has a more pronounced effect on differential-to-common-mode conversion.

Overall, the special hole-misalignment results indicate that the impact of the offset depends strongly on the evaluated signal-integrity metric. The S_{dd11} results show that both x- and y-direction offsets shift the main reflection dip to lower frequencies and broaden the return-loss response. The variations in S_{dd21} become more evident at high frequencies, while the MAT curves remain close to each other, suggesting that the insertion-loss changes are mainly caused by impedance mismatch rather than a significant reduction in the intrinsic available transmission capability. In contrast, S_{cd21} is highly sensitive to the detailed offset configuration. In particular, the asymmetric cases produce much stronger mode conversion, showing that differential symmetry can be severely degraded even when the differential-mode responses and TDR are only moderately affected. Therefore, S_{cd21} provides the most critical indicator for identifying the signal-integrity risk caused by asymmetric hole misalignment.

4.2.2 Monte Carlo Analysis

In practical HDI fabrication, signal microvias may deviate from their nominal positions due to drilling, laser-via formation, or registration tolerances. Such hole misalignment changes the local geometry of the differential via transition and may introduce impedance discontinuity, imbalance between the two conductors, and additional mode conversion. Therefore, a Monte Carlo analysis is performed to evaluate the statistical influence of random hole-position errors on the signal-integrity performance of the investigated structure.

In the Monte Carlo simulations, this model is applied to the stacked microvia transition from L3 to L15. Since the transition consists of several cascaded signal microvias, each signal microvia is assigned an independent random in-plane offset. For the i-th microvia in the stack, the nominal position (x_i, y_i) is therefore shifted to

$$(x_i, y_i) \to (x_i + \Delta x_i,\ y_i + \Delta y_i). \tag{4.1}$$

The random variables Δx_i and Δy_i are independently sampled for different microvias and for the two in-plane directions. This produces a randomly staggered stacked-microvia configuration, instead of simply translating the entire stack by the same amount.

The random deviations are assumed to follow independent zero-mean Gaussian distributions,

$$\Delta x_i \sim \mathcal{N}(0, \sigma_x^2), \qquad \Delta y_i \sim \mathcal{N}(0, \sigma_y^2). \tag{4.2}$$

In the Monte Carlo setup, the same standard deviation is used for the two in-plane directions,

$$\sigma_x = \sigma_y = 25\ \mu\text{m}. \tag{4.3}$$

The zero-mean assumption represents an unbiased fabrication tolerance, where the microvia positions fluctuate around their nominal design locations without a systematic shift.

A cutoff probability of 0.0027 is used, corresponding approximately to a $\pm 3\sigma$ truncation of the Gaussian distribution in each direction. In total, 200 Monte Carlo samples are used in this analysis, with each sample corresponding to one randomly staggered stacked-microvia configuration. Therefore, most random samples are confined within the range of approximately $\pm 75\ \mu$m along both the x- and y-directions. Each signal microvia is assigned independent random offsets Δx_i and Δy_i in the Monte Carlo analysis. This represents the case where the positioning error of each microvia is dominated by local drilling or via-formation uncertainty rather than a systematic displacement of the entire structure.

It should be noted that this hole-misalignment model only perturbs the positions of the signal microvias, while the surrounding pads, anti-pads, reference planes, and routing structures remain at their nominal positions. This is different from layer misalignment, where the copper features on an entire layer are shifted together.

Results for analysis. The Monte Carlo results of hole misalignment are summarized in Figs. A.1–A.4. The differential return loss in Fig. A.1 shows a noticeable statistical spread, indicating that random hole-position errors can affect the local impedance matching of the via transition. In comparison, the differential insertion loss in Fig. A.2 remains more concentrated, with the spread becoming more visible only at high frequency. The MAT distribution in Fig. A.3 is even narrower, suggesting that the maximum available transmission capability is only weakly affected by random hole misalignment. Therefore, the variation observed in S_{dd21} is mainly related to mismatch and local reflection rather than a significant degradation of the intrinsic transmission capability.

In contrast, the mode-conversion coefficient in Fig. A.4 exhibits the largest statistical variation. This indicates that S_{cd21} is much more sensitive to random hole-position errors than the differential-mode metrics. Although the differential-mode transmission remains relatively stable, random hole misalignment can strongly disturb the symmetry of the differential via pair and lead to large uncertainty in differential-to-common-mode conversion. Therefore, mode conversion is the most critical response for evaluating the signal-integrity risk caused by random hole misalignment.

As discussed in Section 3.2.3, very small mode-conversion coefficients may approach the numerical convergence level of the full-wave simulation. Therefore, the absolute values of S_{cd21} at very low levels should be interpreted with caution, and the results are mainly used to compare relative trends and statistical variations.

4.3 Layer Misalignment

Layer misalignment refers to the positional offset between different PCB layers caused by manufacturing registration errors during the multilayer lamination process. Unlike hole misalignment, where only the drilled microvia position is shifted with respect to the designed location, layer misalignment affects all geometrical features located on the shifted layer. Therefore, both signal and ground microvias, as well as the associated pads and traces on the misaligned layer, are displaced together. Besides its direct impact on SI performance, layer misalignment may also modify the copper distribution, local electric-field distribution, and thermal/mechanical paths in the three-dimensional PCB interconnect structure, thereby reducing the overall interconnect reliability.

In this section, the impact of layer misalignment on the considered differential microvia transition is investigated. Similar to the hole-misalignment analysis, several representative deterministic misalignment cases are first studied to reveal the underlying physical mechanisms. Afterwards, a Monte Carlo analysis is performed to evaluate the statistical influence of random layer-to-layer registration errors.

For the layer-misalignment analysis, all microvias in the transition structure are modeled as conical microvias, including both signal and ground microvias. This is different from the hole-misalignment analysis, where only the signal microvias were replaced by conical models to reduce the simulation cost, while the ground microvias were kept as cylindrical models. Therefore, the reference case denoted as Con-REF corresponds to the fully conical microvia model without any layer misalignment.

4.3.1 Special case analysis

In this section, several special cases of layer misalignment are investigated. Unlike the hole-misalignment analysis, where only the signal microvias are modeled with a conical geometry to reduce the simulation cost, all microvias in the layer-misalignment models are replaced by conical microvias, including both signal and ground microvias. Therefore, the reference case denoted as Con-REF corresponds to the fully conical microvia model without any layer misalignment. In all special cases, the offset Δx_l and Δy_l is equal to 94.4 um. Therefore, this represents a critical state, where the small circular edge of the tapered microvia hole with the offset is close to the edge of the pad on next layer.

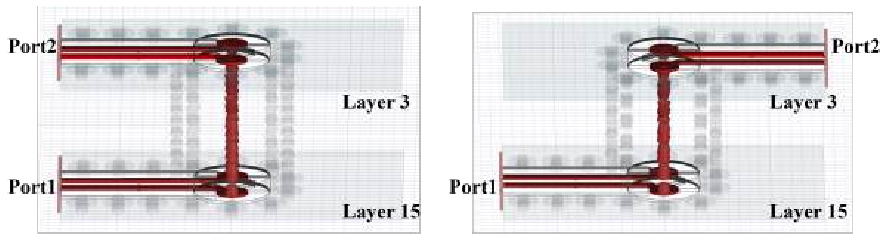

Figure 4.6: Comparison of two routing configurations after the microvia layer transition. Left: opposite fan-out transition. Right: same-direction fan-out transition.

The labels Same and Opp denote the same-direction and opposite-direction fan-out transitions, respectively. As shown in Fig. 4.6, in the same-direction fan-out transition, the upper and lower traces extend toward the same lateral direction. In the opposite-direction fan-out transition, the upper and lower traces extend toward opposite lateral directions. For each fan-out configuration, layer misalignment is applied along both the x- and y-directions. The investigated layer-misalignment cases are illustrated in Fig. 4.7. The red arrows indicate the layer displacement in the x-direction, while the green arrows indicate the layer displacement in the y-direction.

Two representative layer-misalignment cases are considered. Case 1 represents the misalignment of the signal layers only. Case 2 represents a staggered

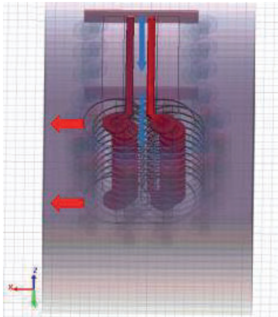

(a) Same.1dx

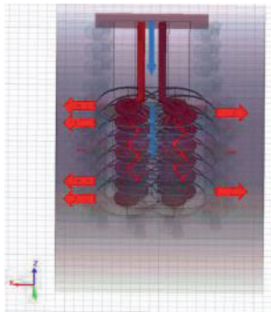

(b) Same.2dx

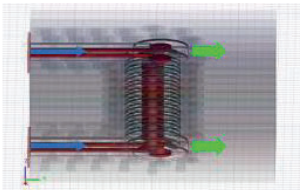

(c) Same.1dy

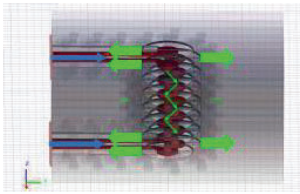

(d) Same.2dy

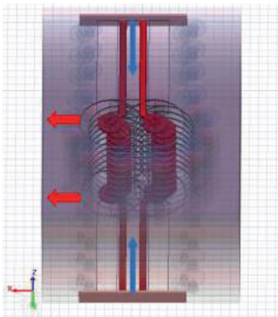

(e) Opp.1dx

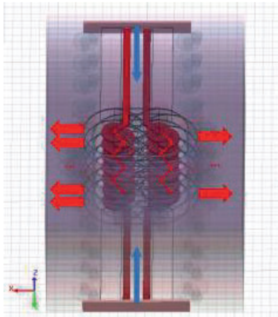

(f) Opp.2dx

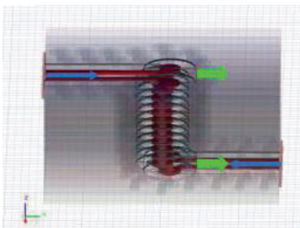

(g) Opp.1dy

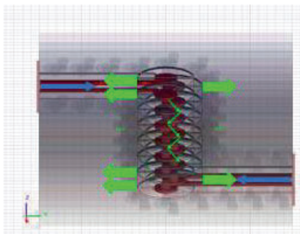

(h) Opp.2dy

Figure 4.7: Three-dimensional geometrical models of the investigated layer-misalignment cases, where Same and Opp denote same-direction and opposite-direction fan-out transitions, respectively. Case 1 includes only signal-layer misalignment, while Case 2 includes staggered misalignment of both signal and ground layers, forming a zigzag-like transition.

misalignment of all layers, including both signal and ground layers. This produces a zigzag-like transition geometry, where the signal and ground microvia stacks are displaced in a staggered manner. Therefore, Case 2 introduces a stronger perturbation to both the differential signal path and the return-current path.

Results for layer misalignment.

TDR For the TDR results, Case 1 and Case 2 exhibit different levels of sensitivity to layer misalignment, as shown in Fig. 4.8a and Fig. 4.8b. In Case 1, only the signal layers are shifted, so the additional routing path introduced by the misalignment is relatively short. As a result, the TDR curves remain very close to the conical reference case. The minimum impedance is approximately 76.5–77.5 Ω, while the reference case has a minimum impedance of about 77 Ω. Therefore, the variation of the minimum TDR impedance in Case 1 is less than approximately 1 Ω. This indicates that shifting only the signal layers introduces only a weak local impedance perturbation.

In contrast, Case 2 shows a much stronger TDR variation because the relative shift is introduced between every layer. This results in a longer additional signal path and a larger accumulated geometrical discontinuity along the vertical transition. The minimum impedance decreases to approximately 73–74 Ω, depending on the misalignment configuration. In particular, the Same.2dx case gives the lowest impedance, around 73 Ω, corresponding to a reduction of about 4 Ω compared with the conical Con.REF case. The Same.2dy case and Opp.2dx case show a clear impedance reduction, with a minimum value of approximately 73 Ω. By comparison, the Same.2dy and Opp.2dy cases remain closer to the Same.2dy case and Opp.2dx case response, with minimum impedances around 74 Ω. The deeper impedance dip in Case 2 confirms that misalignment between multiple layers has a stronger cumulative effect than shifting only the signal layers.

$\boldsymbol{S_{\mathrm{dd11}}}$ As shown in Fig. 4.8c and Fig. 4.8d, the effect of layer misalignment on S_{dd11} is generally small. Although variations appear at some frequencies, the overall reflection responses remain close to the Con.REF structure, indicating that the transition has a certain tolerance to layer misalignment.

If the two cases are compared in more detail, Case 1 produces only a weak perturbation because only the signal layers are shifted, whereas Case 2 shows slightly larger variations due to the accumulated layer-to-layer displacement.

In the frequency range from 0 to 30 GHz, the 4 misaligned cases in Case 2 show an approximately 3–5 dB degradation in S_{dd11} compared with the Con.REF case.

However, the trend becomes different above approximately 45 GHz. In Case 1, all 4 misaligned cases show a degradation of about 1–3 dB compared with the Con.REF case. In contrast, in Case 2, the 4 misaligned cases exhibit better S_{dd11} performance than the Con.REF case in this high-frequency region. The maximum improvement occurs near 60 GHz, where the best misaligned case improves the return loss by approximately 8 dB. This improvement also leads to a corresponding improvement in S_{dd21}, especially because the return-loss level above 45 GHz is

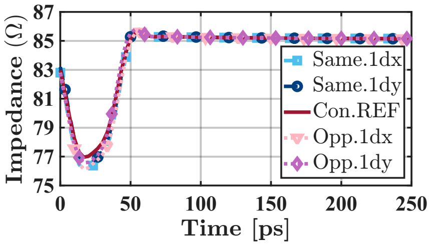

(a) TDR for Case 1

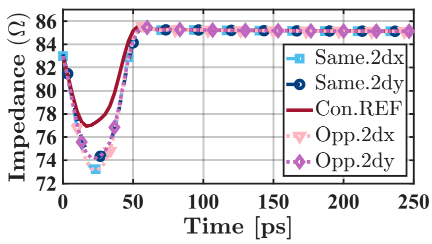

(b) TDR for Case 2

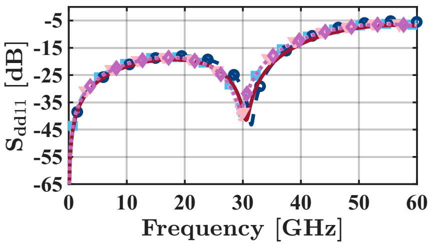

(c) S_{dd11} for Case 1

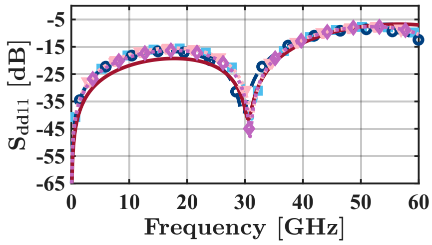

(d) S_{dd11} for Case 2

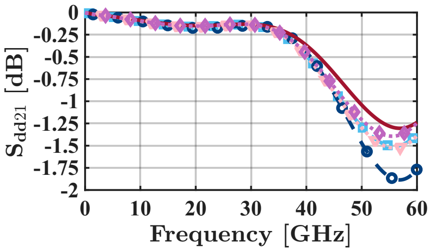

(e) S_{dd21} for Case 1

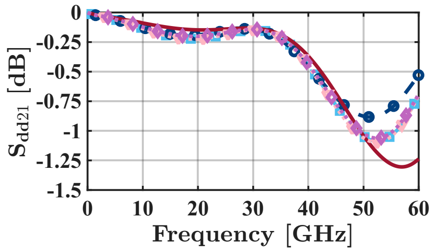

(f) S_{dd21} for Case 2

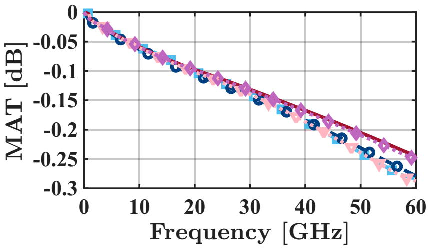

(g) MAT for Case 1

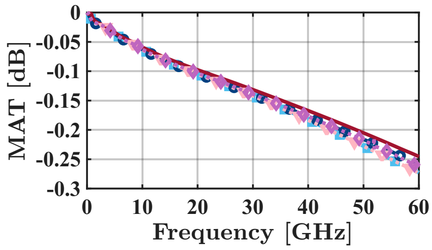

(h) MAT for Case 2

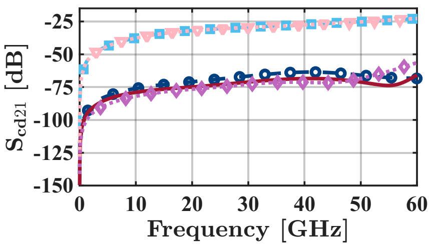

(i) S_{cd21} for Case 1

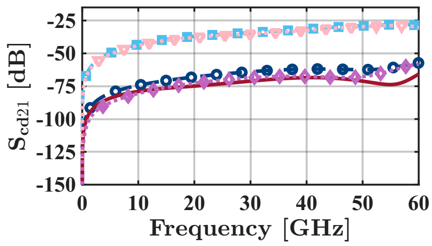

(j) S_{cd21} for Case 2

Figure 4.8: Simulated signal-integrity responses of the special hole-misalignment cases in the x- and y-directions.

relatively poor and is mostly higher than −10 dB. Therefore, in this frequency range, the transmission response is strongly affected by the mismatch condition.

S_{dd21} As shown in Fig. 4.8e and Fig. 4.8f, the S_{dd21} results show that the influence of layer misalignment is mainly visible above 40 GHz.

For Case 1 shown in Fig. 4.8e, the curves are almost identical below 35 GHz, with S_{dd21} remaining within about 0 to −0.25 dB. At 55–60 GHz, the Con.REF case is around −1.3 dB, while the other 4 misaligned cases decrease to approximately -1.4 to −1.9 dB.

For Case 2, shown in Fig. 4.8f, the 4 misaligned cases remain very close to the Con.REF response below 45 GHz, with a difference generally within about 0.1 dB. Above 45 GHz, the 4 misaligned cases become better than the Con.REF case. At 60 GHz, the Con.REF case is approximately −1.25 dB, whereas the best misaligned case is around −0.5 dB, corresponding to an improvement of about 0.7 dB.

Above 45 GHz, the Con.REF case suffers from relatively poor matching, which causes a larger portion of the incident power to be reflected. In contrast, the 4 misaligned structures in Case 2 slightly improve the matching condition, thereby reducing the reflected power and allowing more power to be transmitted through the transition. As a result, an apparent improvement in S_{dd21} is observed.

MAT The corresponding MAT responses are shown in Figs. 4.8g and 4.8h. Since MAT is a mismatch-corrected transmission metric, it is less affected by the reflection behavior than S_{dd21}, and therefore better reflects the intrinsic available transmission capability of the microvia transition.

For both cases, the MAT curves are almost identical below approximately 35 GHz. This is because the additional path length introduced by layer misalignment is electrically small compared with the guided wavelength in this frequency range. Therefore, its influence on the intrinsic transmission capability is negligible.

At higher frequencies, small but visible differences appear. In Case 1, the Con.REF case and Opp.1dy remain almost the same at high frequencies, reaching approximately −0.25 dB at 60 GHz. In contrast, the other misaligned cases decrease to about −0.28 dB, corresponding to an additional degradation of approximately 0.03 dB. This difference can be explained by the effective path length. For Opp.1dy, the fan-in and fan-out directions are opposite, so the path-length change introduced by the layer shift is largely compensated. As a result, its effective path length remains close to that of the Con.REF case. The other misaligned cases introduce a small net increase in path length, leading to slightly lower MAT values.

For Case 2, the 4 misaligned cases are very close to each other over the whole frequency range. At 60 GHz, they are mainly around −0.27 dB, while the reference case is slightly higher, around −0.24 dB. This indicates that when the relative shift is introduced between every layer, the accumulated additional path lengths of the misaligned configurations become similar, so their MAT responses almost overlap.

Overall, for the layer-misalignment cases studied here, the small differences in MAT are mainly associated with the change in effective path length. Since MAT is a mismatch-corrected metric, the influence of input reflection is reduced. Moreover, the material properties, via dimensions, and stack-up remain unchanged among these 8 cases. Therefore, the remaining difference in the intrinsic available transmission capability is mainly caused by the small change in the effective signal path length.

S_{cd21} In both Case 1 and Case 2 shown in Figs. 4.8i and 4.8j, the x-direction misalignment cases produce a much higher S_{cd21} than the Con.REF structure, showing that this direction more strongly breaks the symmetry of the differential transition. In contrast, the y-direction misalignment cases remain closer to the Con.REF response, indicating a weaker influence on differential-to-common-mode conversion.

Moreover, the curves with the same misalignment direction are similar for the same-direction and opposite-direction fan-out cases. This suggests that the mode-conversion level is mainly governed by the misalignment direction, while the fan-out direction plays a secondary role. Therefore, x-direction layer misalignment is the more critical condition for S_{cd21}.

Overall, layer misalignment perpendicular to the routing direction has a stronger impact on mode conversion because it more directly breaks the geometrical and electrical balance of the differential pair. This imbalance causes the two conductors to experience different local discontinuities, thereby increasing the conversion from differential mode to common mode.

4.3.2 Monte Carlo Analysis

In multilayer PCB fabrication, layer misalignment may occur during the lamination and registration process. Different layers may not be perfectly aligned with respect to each other, which changes the relative positions between signal pads, traces, antipads, reference-plane openings, and microvia landing structures. As a result, the local electromagnetic environment of the differential via transition can be modified, leading to impedance mismatch, transmission degradation, and possible mode conversion. Therefore, a Monte Carlo analysis is performed to evaluate the statistical influence of random layer misalignment on the signal-integrity performance of the investigated structure.

In this work, the signal layers L3 and L15 are kept fixed in the simulation coordinate system and are used as reference layers. The other layers in the PCB stackup are allowed to have arbitrary in-plane positional deviations with respect to these reference layers. For the (l)-th misaligned layer, the layer displacement is described by two lateral offset components, Δx_l and Δy_l. Therefore, for a nominal position ((x,y)) on layer (l), the shifted position is written as

$$(x, y) \rightarrow (x + \Delta x_l, y + \Delta y_l), \tag{4.4}$$

where Δx_l and Δy_l denote the layer-level misalignment in the (x)- and (y)-directions, respectively.

The misalignment components are modeled as independent zero-mean Gaussian random variables,

$$\Delta x_l \sim \mathcal{N}(0, \sigma_x^2), \qquad \Delta y_l \sim \mathcal{N}(0, \sigma_y^2). \tag{4.5}$$

In this analysis, $\sigma_x = \sigma_y = 25\ \mu$m is used. The zero-mean assumption represents an unbiased manufacturing tolerance, where the layer position fluctuates around its nominal location without a systematic offset. A cutoff probability of 0.0027 is applied to the Gaussian distribution, which corresponds approximately to a $\pm 3\sigma$ truncation. Therefore, most random samples are confined within approximately $\pm 75\ \mu$m in each direction. In total, 200 Monte Carlo samples are used in this analysis, with each sample corresponding to one randomly generated layer-misalignment configuration.

It should be emphasized that the layer misalignment is applied at the layer level. All relevant geometrical features on the same misaligned layer share the same displacement values Δx_l and Δy_l. Therefore, the whole layer is translated as a rigid body in the lateral plane. This is different from the hole-misalignment case, where only the signal microvia positions are perturbed independently.

Results for analysis. Monte Carlo analysis is performed to evaluate the statistical robustness of the transition under random layer misalignment caused by fabrication tolerances. Compared with deterministic misalignment cases, it provides the distribution, mean value, and variation range of the signal-integrity metrics. Therefore, it can be used to determine whether the transition is sensitive to random misalignment and whether the same-direction or opposite-direction fan-out configuration shows better tolerance.

As shown in Fig. A.5, the distributions of S_{dd11} for the Same and Opp fan-out configurations largely overlap at 5, 25, and 60 GHz. Their mean values and 3σ ranges are very close, indicating that the fan-out direction has little influence on the statistical variation of the differential-mode reflection coefficient. A similar trend is observed for S_{dd21}, as shown in Fig. A.6. The two fan-out configurations exhibit nearly the same transmission-loss distributions, suggesting comparable robustness in terms of differential-mode transmission.

The MAT results in Fig. A.7 further confirm this observation. The Same and Opp distributions are very close at all selected frequencies, which indicates that the maximum achievable transmission capability is only weakly affected by random layer misalignment. Therefore, no clear statistical advantage of either fan-out direction can be identified from the reflection, transmission, or MAT results.

For the mode-conversion coefficient S_{cd21}, shown in Fig. A.8, the distributions are wider than those of the other metrics, especially at higher frequencies. This suggests that differential-to-common-mode conversion is more sensitive to random layer misalignment because it is directly related to the geometrical imbalance of the differential transition. Nevertheless, the Same and Opp distributions still largely overlap, indicating that the fan-out direction is not the dominant factor for the statistical mode-conversion behavior.

Overall, the Monte Carlo results indicate that the same-direction and opposite-direction fan-out configurations show very similar statistical performance under random layer misalignment. No consistent superiority is observed for either fan-out direction. The investigated transition therefore shows reasonable tolerance to random layer misalignment, while mode conversion is identified as the most sensitive metric among the considered signal-integrity responses.

4.4 Summary

This chapter investigated the impact of manufacturing-induced staggering on the SI performance of differential microvia transitions. Two types of fabrication tolerances were considered: hole misalignment and layer misalignment. For each case, deterministic offset cases were first analyzed to identify the physical mechanisms, followed by Monte Carlo analysis to evaluate the statistical influence of random manufacturing variations. Overall, the results show that manufacturing-induced staggering affects mode conversion more strongly than differential-mode reflection and transmission.

The differential return loss S_{dd11} shows a shifted and broadened reflection dip. The insertion loss S_{dd21} varies mainly at high frequencies, while the MAT curves remain close to each other, indicating that the degradation is mainly caused by impedance mismatch rather than a significant reduction in intrinsic transmission capability. Among all metrics, S_{cd21} is the most sensitive to hole misalignment, especially for asymmetric offsets that break the balance of the differential pair.

For layer misalignment, shifting only the signal layers has a limited impact on the overall signal-integrity response, whereas staggered misalignment involving both signal and ground layers causes more visible local impedance variations. However, S_{dd11}, S_{dd21}, and MAT remain relatively stable, showing that the investigated transition has reasonable tolerance to random layer misalignment. The mode-conversion response is again more sensitive, especially for x-direction layer misalignment. The same-direction and opposite-direction fan-out configurations show no clear statistical difference in the investigated cases. Therefore, S_{cd21} should be carefully evaluated together with conventional metrics such as S_{dd11}, S_{dd21}, MAT, and TDR.

Chapter 5

Conclusion and Future Work

5.1 Conclusions

This thesis investigated the impact of microvia vertical geometry and manufacturing-induced staggering on the SI performance of high-speed differential interconnects in multilayer PCB structures. The study was motivated by the fact that practical microvias are affected by fabrication-related non-idealities, including tapered via profiles, hole-position errors, and layer-to-layer registration errors. To support the analysis, the theoretical background of microvias, transmission-line behavior, mixed-mode S-parameters, TDR, isolation, MAT, and power-balance-based loss estimation was first introduced. These quantities were then used as the main evaluation metrics throughout the simulation study.

In Chapter 3, the influence of microvia vertical geometry was investigated. First, the conventional polygonal cylindrical microvia model was analyzed under different transition lengths and antipad sizes. The results show that shorter transitions exhibit smoother and more stable broadband responses, whereas longer transitions show stronger high-frequency variation and higher sensitivity to antipad size. The TDR results also show that the antipad size changes the local impedance profile in the microvia-transition region. These results provide a baseline for understanding the behavior of the conventional cylindrical approximation before comparing it with more realistic microvia geometries.

The cylindrical microvia model was then compared with conical microvia models. Three cases were considered: the default cylindrical reference model, the model with only conical signal microvias, and the model with both signal and ground microvias represented by conical geometries. The comparison shows that the three models have similar differential insertion-loss behavior at low and middle frequencies, but visible differences appear in return loss, mode conversion, TDR, impedance, and isolation, especially at higher frequencies and for longer layer transitions. The port-impedance analysis further shows that the extracted intermediate impedance Z_x is affected by the microvia geometry, and the difference becomes more noticeable as the transition length increases. The isolation analysis also shows that different microvia geometries lead to different predicted coupling levels and radiation-related loss. Therefore, the conical microvia model provides a more realistic representation for deep-layer and high-frequency interconnects. At the same time, the computational-cost comparison shows that modeling all vias as conical structures is significantly more expensive. As a practical compromise, applying the conical geometry mainly to the signal microvias can be used for a preliminary signal-integrity estimation with reduced simulation cost. However, this simplified model is not suitable when the isolation performance is of primary interest, because the coupling behavior is also influenced by the geometry of the surrounding ground microvias.

In Chapter 4, the impact of manufacturing-induced staggering was studied. Two types of misalignment were considered: hole misalignment and layer misalignment. For hole misalignment, several deterministic offset cases were first analyzed in both the x- and y-directions. The differential return loss S_{dd11} shows that hole misalignment shifts the main reflection features toward lower frequencies and broadens the frequency range where $S_{\mathrm{dd11}} < -25$ dB. The differential insertion loss S_{dd21} shows more visible variation at higher frequencies, while MAT remains relatively stable. This indicates that the overall available transmission capability is only weakly affected by the investigated hole-position variations. In contrast, the mode-conversion coefficient S_{cd21} is much more sensitive to the detailed offset configuration. In particular, asymmetric hole-misalignment cases produce a larger increase in differential-to-common-mode conversion. The Monte Carlo analysis further confirms this trend: S_{dd11}, S_{dd21}, and MAT show relatively limited statistical variation, whereas S_{cd21} has a much wider distribution.

Layer misalignment was also analyzed through deterministic cases and Monte Carlo simulations. In the deterministic study, two representative cases were considered. Case 1 involves the misalignment of the signal layers only, while Case 2 includes staggered misalignment of both signal and ground layers. The results show that Case 1 has only a limited influence on the overall response, whereas Case 2 produces more visible local impedance variation and high-frequency differences. For the differential-mode quantities, S_{dd11}, S_{dd21}, and MAT remain relatively close to the reference case, indicating that the investigated transition is reasonably robust in terms of differential-mode reflection and transmission. However, S_{cd21} again shows stronger sensitivity, especially for the x-direction layer misalignment, where the layer offset is perpendicular to the differential-pair routing direction. The comparison between same-direction and opposite-direction fan-out configurations shows no clear statistical advantage for either case. Their Monte Carlo distributions largely overlap, indicating that the fan-out direction is not the dominant factor in the investigated layer-misalignment cases.

Overall, this thesis shows that microvia vertical geometry and manufacturing-induced staggering can both influence the signal-integrity prediction of high-speed differential interconnects, especially for long-layer transitions and high-frequency operation. Simplified cylindrical models and ideal-alignment assumptions can be used for preliminary differential-mode analysis, but more realistic geometry and misalignment modeling are needed for long transitions and high-frequency operation, especially when TDR variation, isolation, and mode conversion are of interest.Therefore, S_{dd11}, S_{dd21}, MAT, and TDR should be evaluated together with S_{cd21}, which is more sensitive to geometrical asymmetry. These findings provide practical guidance for microvia modeling, tolerance evaluation, and robust SI design in high-speed HDI PCB interconnects.

5.2 Future Work

Although extensive simulations and theoretical analyses have been carried out in this thesis, experimental validation and comparative measurements have not yet been performed due to limitations in time. Therefore, future work could be directed toward prototype fabrication and physical testing to further verify the simulation results presented in this work.

In addition, the manufacturing-induced staggering considered in this thesis is modeled using simplified hole-misalignment and layer-misalignment assumptions. In practical fabrication, these two effects may occur simultaneously and may also be correlated with other process variations. Therefore, future work could further investigate more realistic tolerance models, including combined hole and layer misalignment, systematic process offsets, and different statistical distributions of manufacturing errors.

Furthermore, to simplify the analysis, this study only considers conical microvias with a specific taper angle. In practical manufacturing, however, via geometry can be affected by many factors, including the aspect ratio of the hole, the material properties of the dielectric and metal, and the details of the fabrication process. Different geometrical variations may lead to different levels of impact on SI performance. Recent studies have also investigated void defects formed inside via holes during fabrication, as well as the influence of their geometrical characteristics [39]. These topics provide valuable directions for future research and could contribute to a more comprehensive understanding of the relationship between fabrication-induced geometrical variations and SI performance.

Appendix A

Monte Carlo Results for Staggering

Figs. A.1–A.4 show the Monte Carlo results for the L3–L15 transition with random hole misalignment, including S_{dd11}, S_{dd21}, MAT, and S_{cd21}. Figs. A.5–A.8 show the Monte Carlo results for the same L3–L15 transition with random layer misalignment. These figures are used to evaluate the statistical influence of layer shifts and fan-out configurations on the same performance metrics.

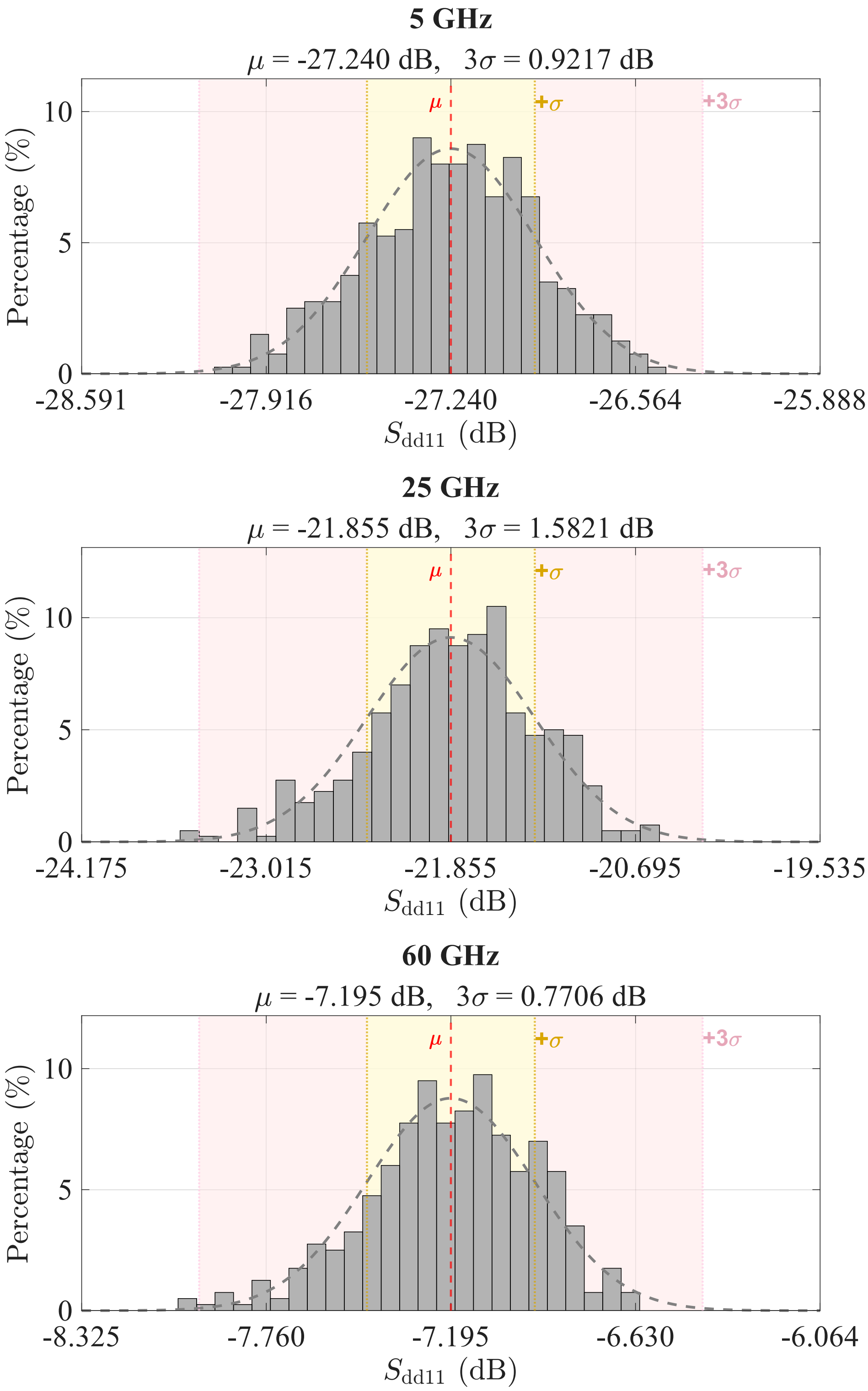

Figure A.1: Monte Carlo distribution of the differential return loss S_{dd11} at 5, 25, and 60 GHz under hole misalignment.

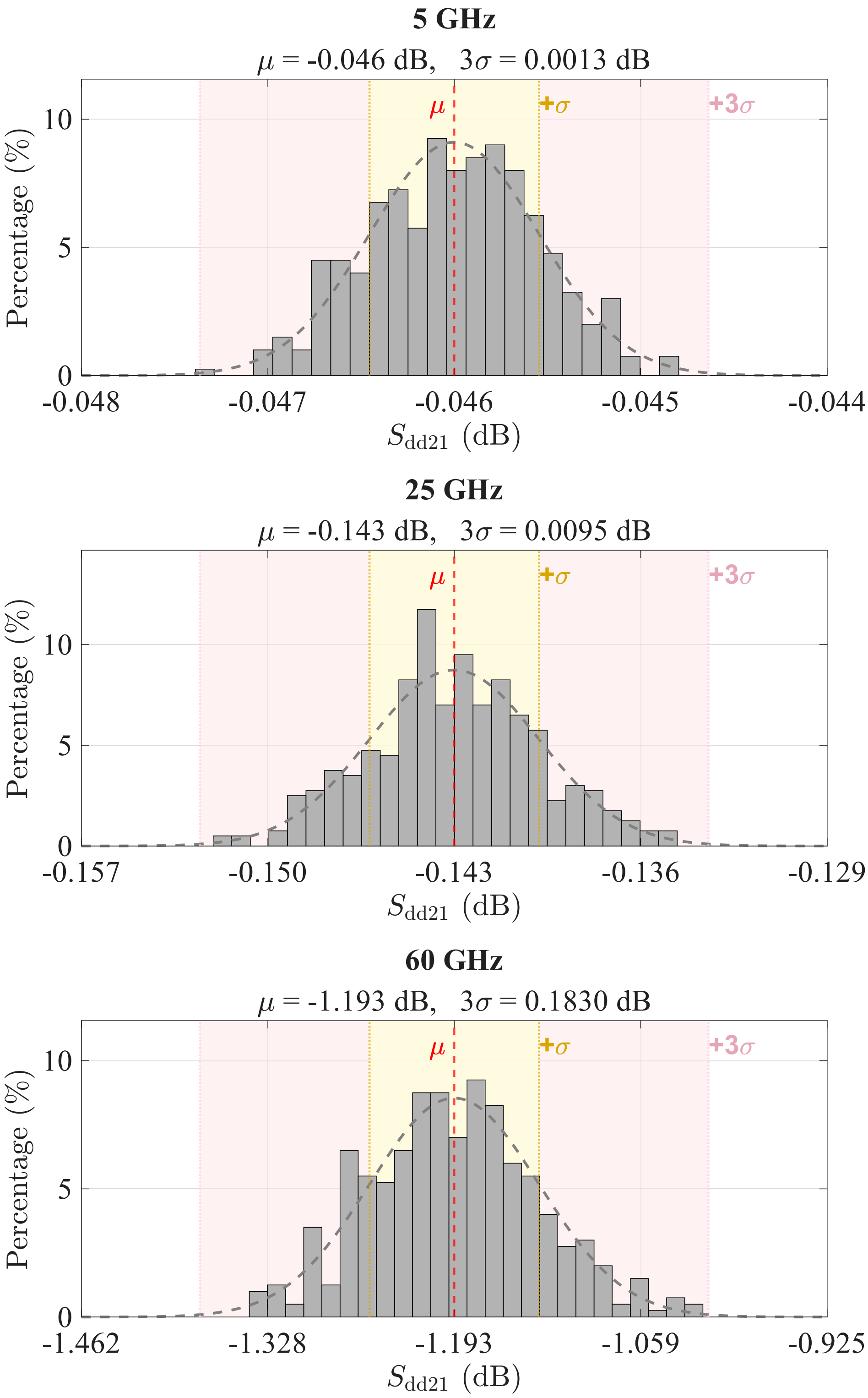

Figure A.2: Monte Carlo distribution of the differential insertion loss S_{dd21} at 5, 25, and 60 GHz under hole misalignment.

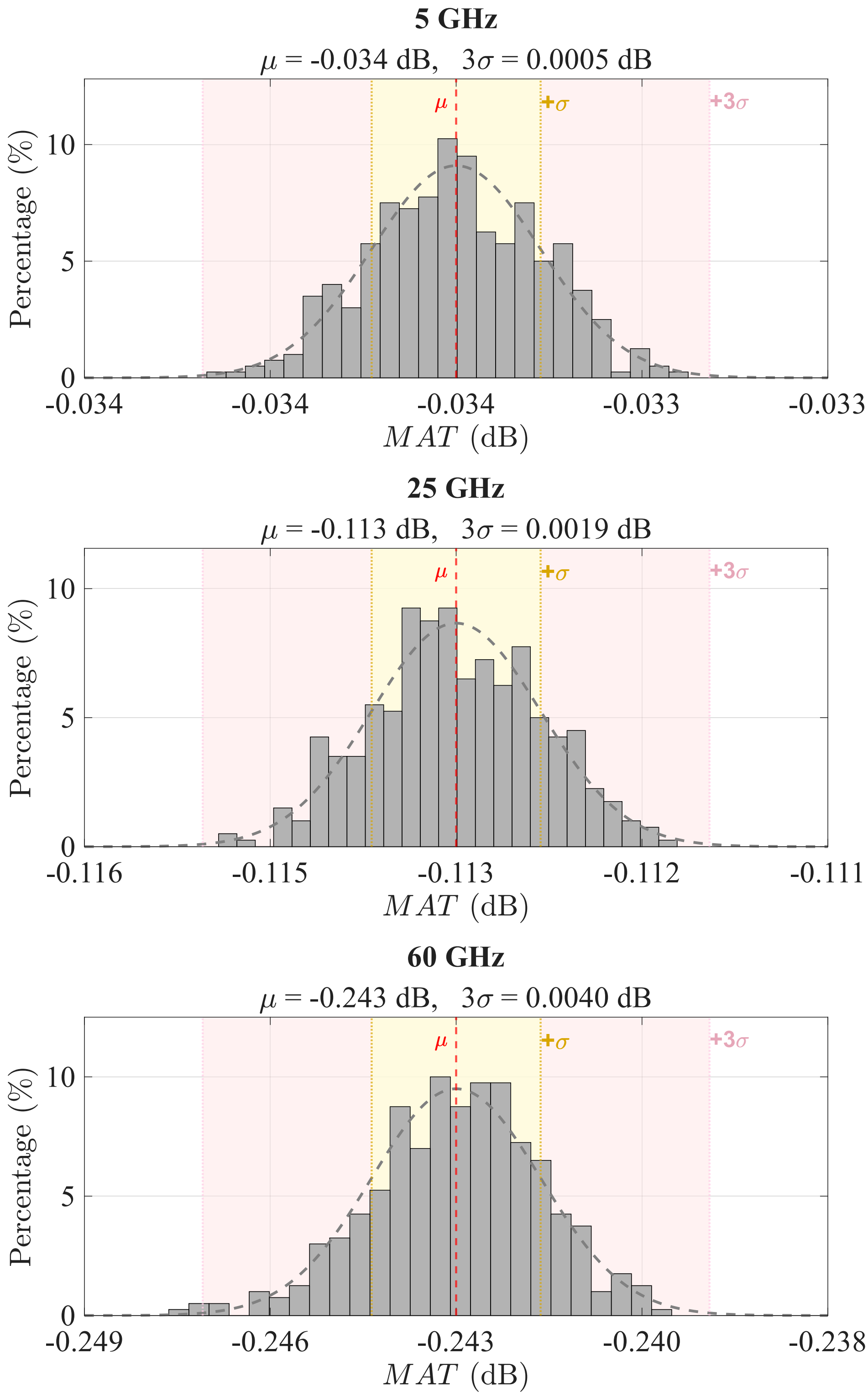

Figure A.3: Monte Carlo distribution of the maximum achievable transmission (MAT) at 5, 25, and 60 GHz under hole misalignment.

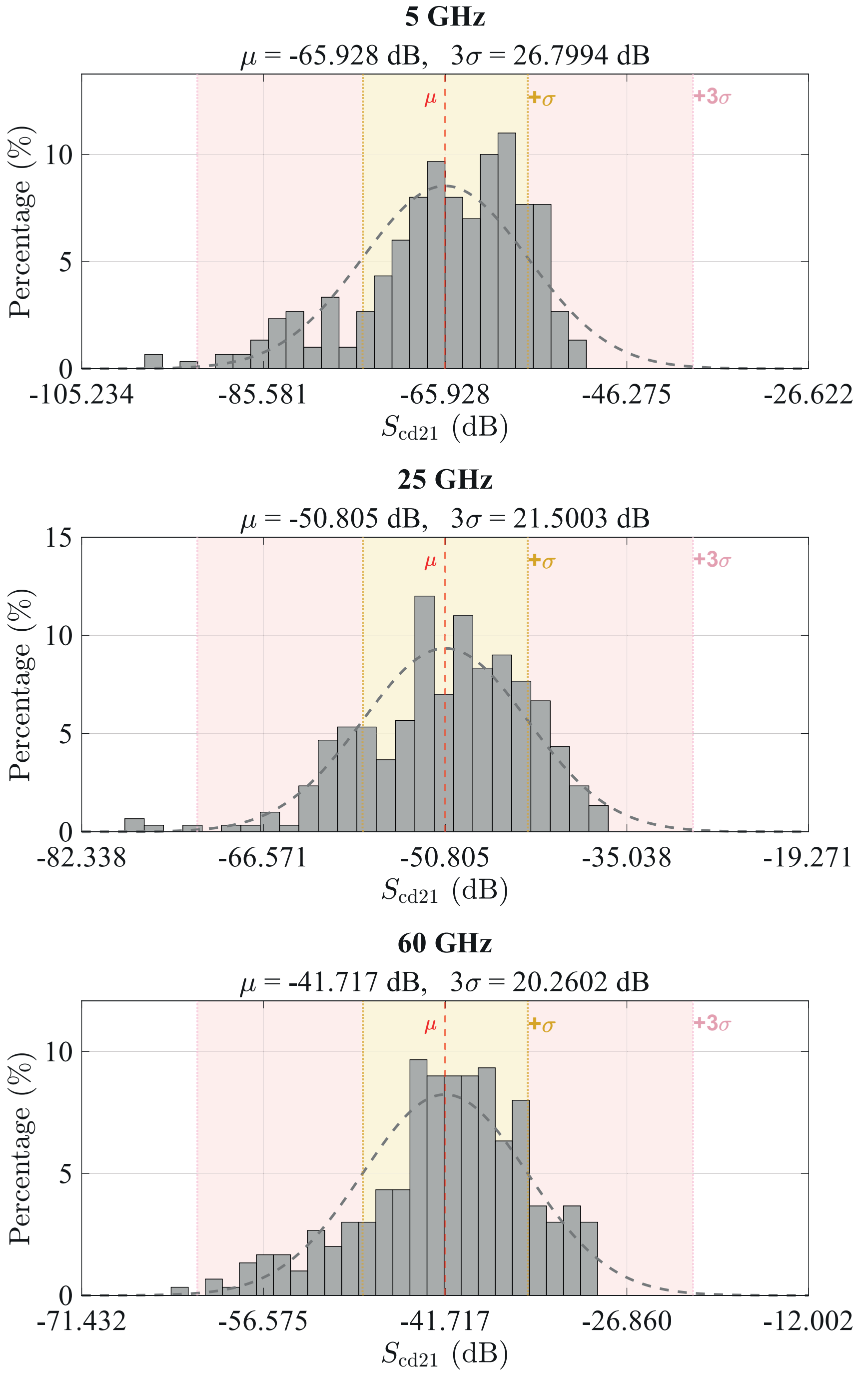

Figure A.4: Monte Carlo distribution of the differential-to-common-mode conversion coefficient S_{cd21} at 5, 25, and 60 GHz under hole misalignment.

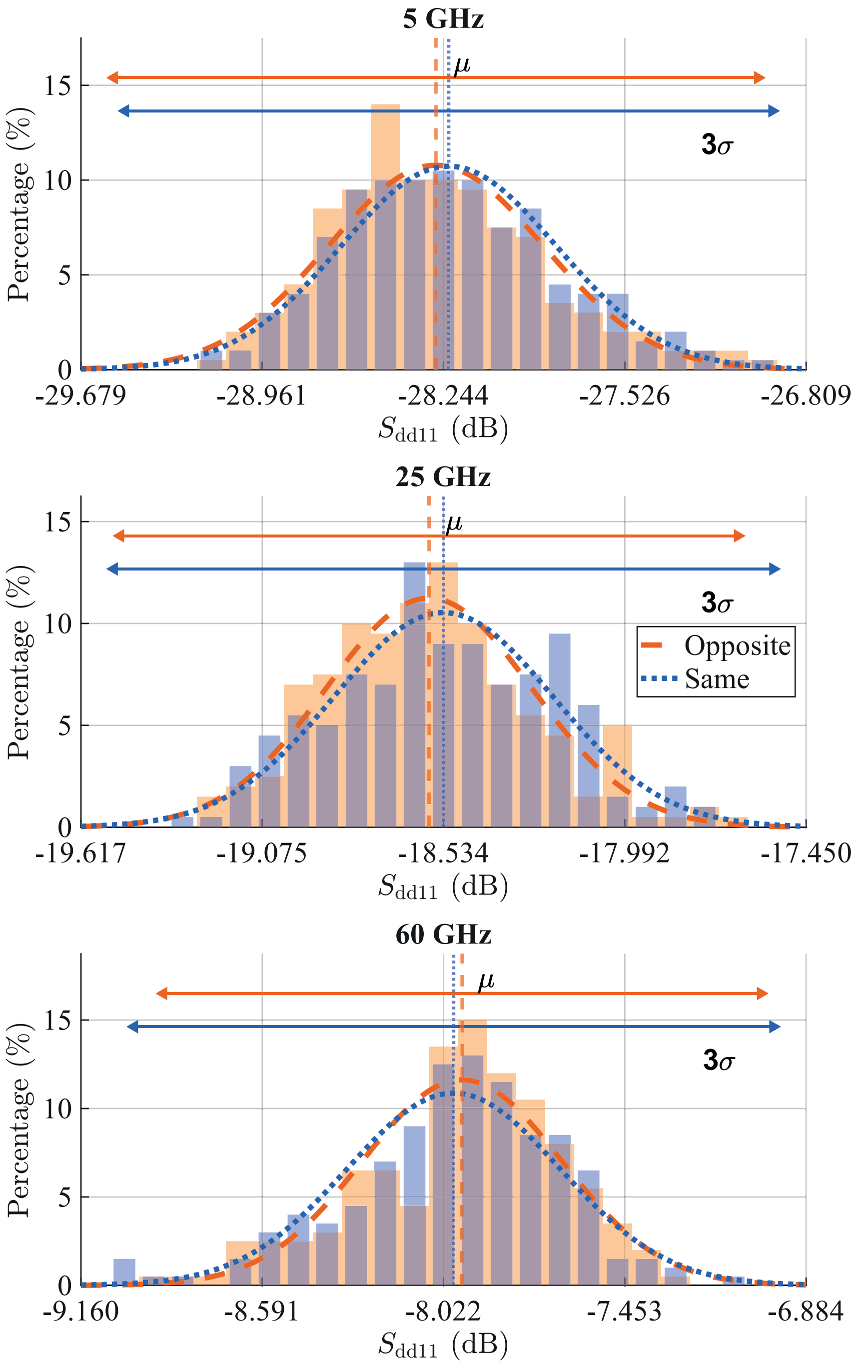

Figure A.5: Monte Carlo distribution of the differential-mode reflection coefficient S_{dd11} at 5, 25, and 60 GHz under layer misalignment for different fan-out directions.

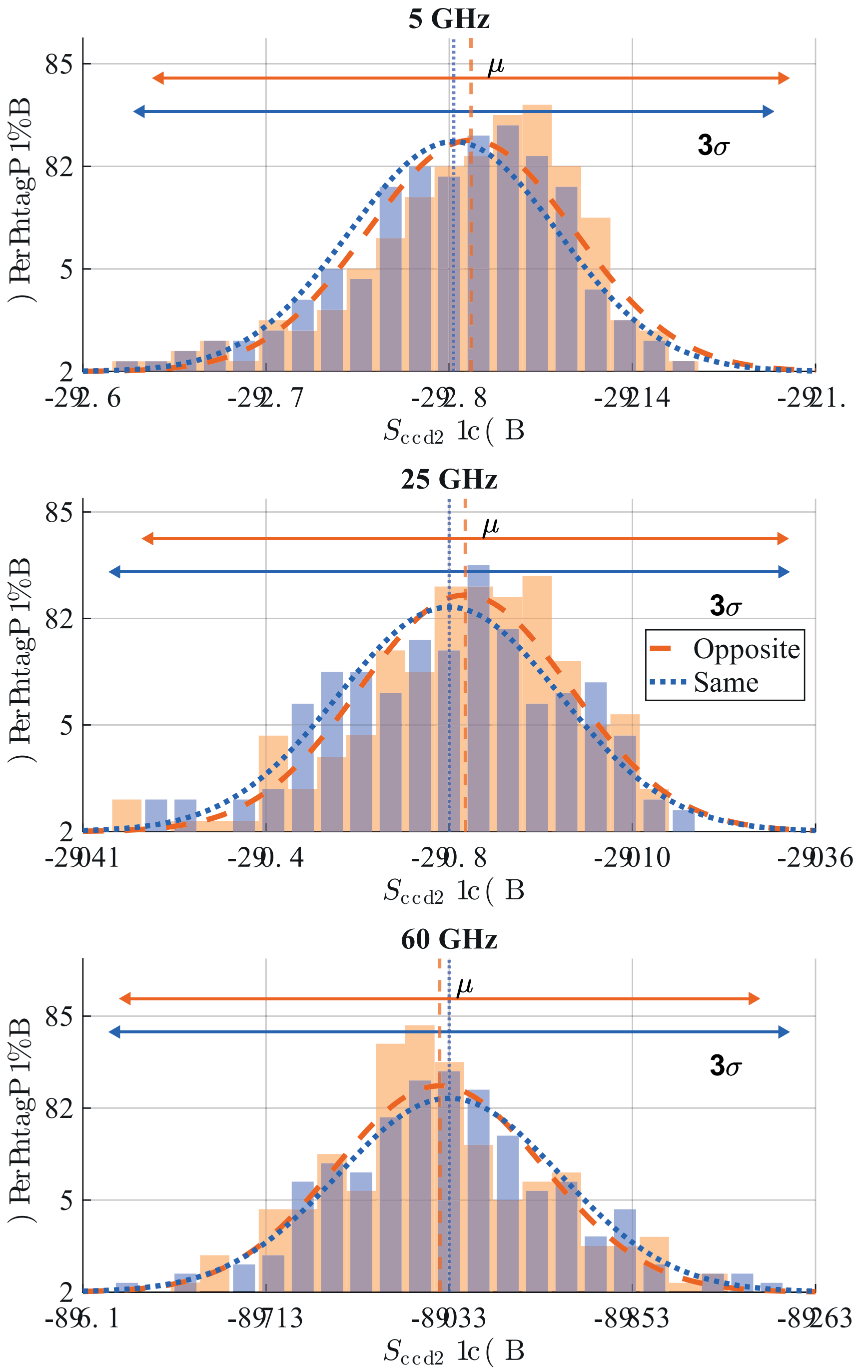

Figure A.6: Monte Carlo distribution of the differential-mode transmission coefficient S_{dd21} at 5, 25, and 60 GHz under layer misalignment for different fan-out directions.

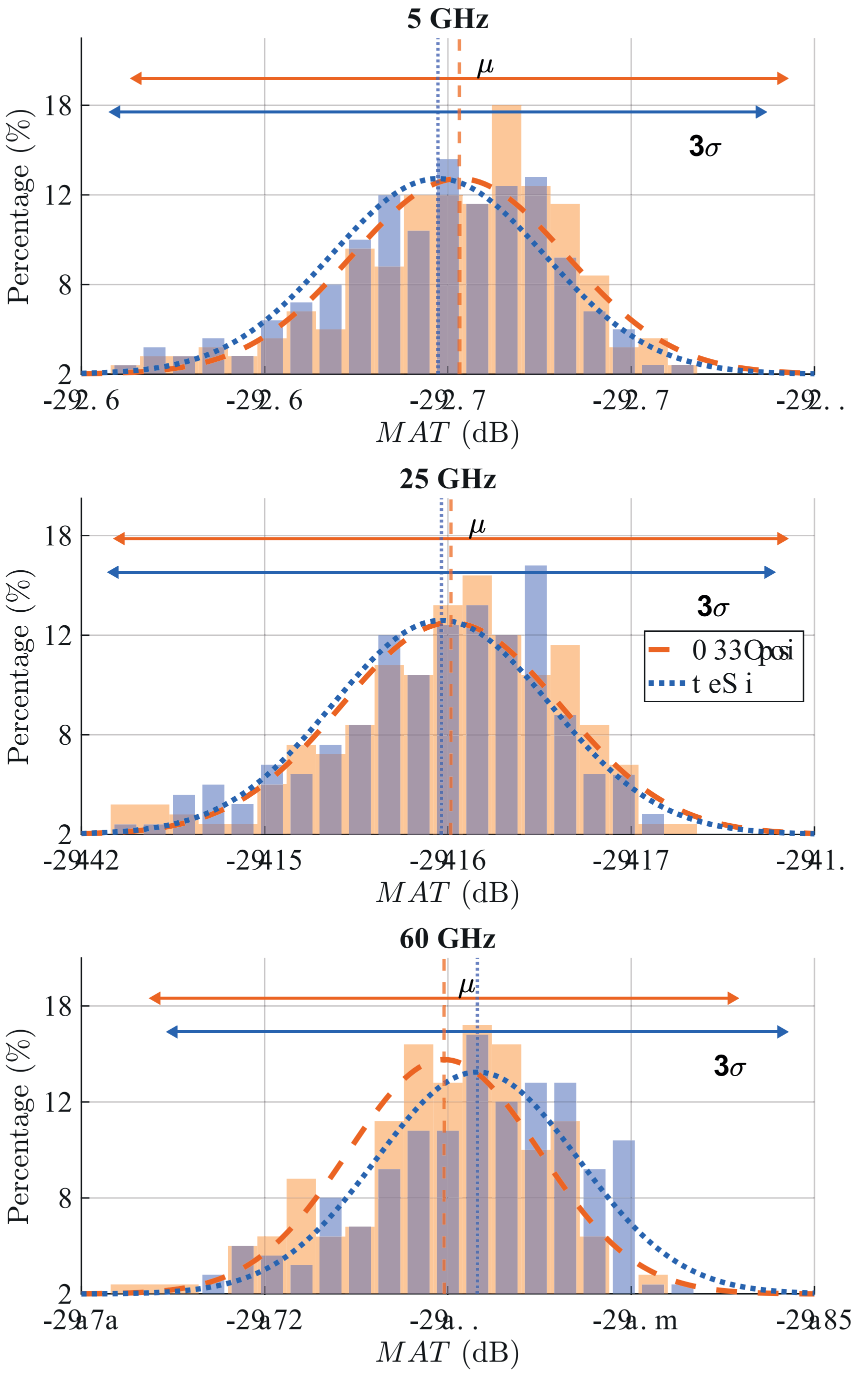

Figure A.7: Monte Carlo distribution of the maximum achievable transmission (MAT) at 5, 25, and 60 GHz under layer misalignment for different fan-out directions.

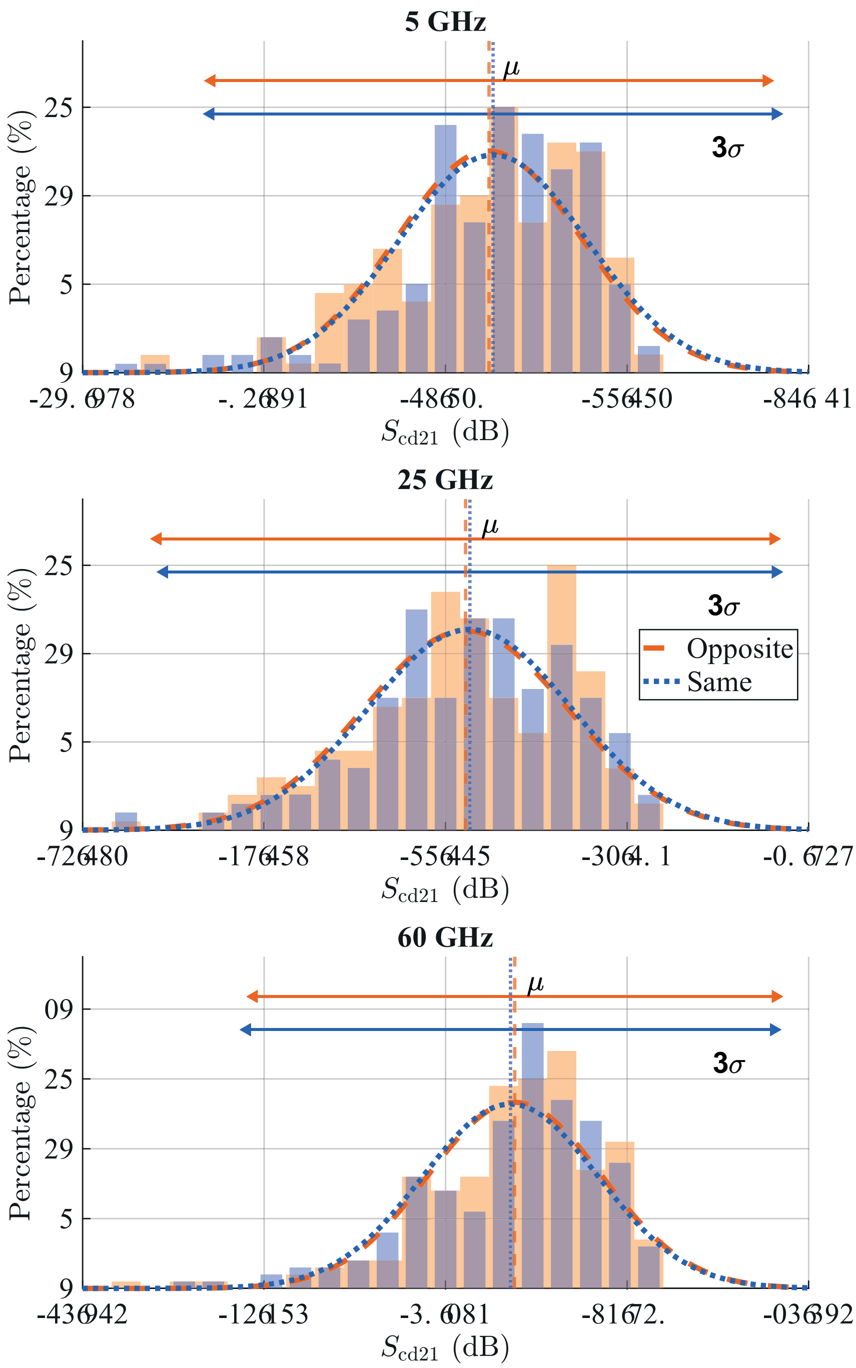

Figure A.8: Monte Carlo distribution of the differential-to-common-mode conversion coefficient S_{cd21} at 5, 25, and 60 GHz under layer misalignment for different fan-out directions.

Bibliography

[1] Fuhan Liu et al. “Reliability assessment of microvias in HDI printed circuit boards”. In: *IEEE Transactions on Components and Packaging Technologies* 25.2 (2002), pp. 254–259.

[2] John H Lau and Chris Chang. “An overview of microvia technology”. In: *Circuit World* 26.2 (2000), pp. 22–32.

[3] Pratik Nimbalkar et al. “Reliability Modeling of Micro-vias in High-Density Redistribution Layers”. In: *2021 IEEE 71st Electronic Components and Technology Conference (ECTC)*. IEEE. 2021, pp. 983–988.

[4] Happy Holden. “Microvias effect on high-frequency signal integrity”. In: *Circuit World* 28.3 (2002), pp. 10–21.

[5] Armin Tajalli, Ali Hormati, and Amin Shokrollahi. “Chord signaling for high-speed data movement: Employing advanced communication and circuit techniques to augment data-transfer bandwidth”. In: *IEEE Solid-State Circuits Magazine* 11.2 (2019), pp. 78–85.

[6] Aaron D Brovont and Andrew N Lemmon. “Common-mode/differential-mode interactions in asymmetric converter structures”. In: *2017 IEEE Electric Ship Technologies Symposium (ESTS)*. IEEE. 2017, pp. 84–90.

[7] W Fan et al. “Mixed-mode S-parameter characterization of differential structures”. In: *Proceedings of the 5th Electronics Packaging Technology Conference (EPTC 2003)*. IEEE. 2003, pp. 533–537.

[8] Ludovica Illiano et al. “Review of mode conversion and modal analysis in electromagnetic compatibility”. In: *IEEE Access* 12 (2024), pp. 65513–65529.

[9] Gianfranco Avitabile et al. “An Optimization Framework for the Design of High-Speed PCB VIAs”. In: *Electronics* 11.3 (2022). ISSN: 2079-9292. DOI: 10.3390/electronics11030475. URL: https://www.mdpi.com/2079-9292/11/3/475.

[10] G Antonini et al. “Characterization of via holes on printed circuit boards”. In: *Proceedings. 8th IEEE Workshop on Signal Propagation on Interconnects*. IEEE. 2004, pp. 211–214.

[11] Wojciech Falinski and Grazyna Koziol. “Applying of stacked microvias in printed circuit board”. In: *2006 29th International Spring Seminar on Electronics Technology*. IEEE. 2006, pp. 411–415.

[12] Bo Tan and Krishnan Venkatakrishnan. “Nd-YAG laser microvia drilling for interconnection application”. In: *Journal of Micromechanics and Microengineering* 17.8 (2007), pp. 1511–1517.

[13] Zhihua Tao et al. “Evaluating the via filling performance with thin surface Cu by the synergistic effect of different additives”. In: *Thin Solid Films* 757 (2022), p. 139390. ISSN: 0040-6090. DOI: https://doi.org/10.1016/j.tsf.2022.139390. URL: https://www.sciencedirect.com/science/article/pii/S0040609022003042.

[14] Bill Birch. “Reliability testing for microvias in printed wire boards”. In: *Circuit World* 35.4 (2009), pp. 3–17.

[15] GA Kouzaev et al. “Influence of eccentricity on the frequency limitations of circular-pad via-holes”. In: *IEEE microwave and wireless components letters* 14.6 (2004), pp. 265–267.

[16] Ahmet C Durgun and Kemal Aygün. “Low Loss Skip Layer Transmission Lines With Common Mode Filtering for Packages”. In: *IEEE Transactions on Components, Packaging and Manufacturing Technology* 12.5 (2022), pp. 839–846.

[17] Stan Heltzel et al. “Advanced PCB technologies for space and their assessment using up-to-date standards”. In: *CEAS Space Journal* 15.1 (2023), pp. 89–100.

[18] Matteo Cocchini et al. “Differential vias transition modeling in a multilayer printed circuit board”. In: *2008 IEEE International Symposium on Electromagnetic Compatibility*. IEEE. 2008, pp. 1–7.

[19] MADPCB. *Microvia*. 2026. URL: https://madpcb.com/microvia/.

[20] Zachariah Peterson. *Everything You Need to Know About Microvias in Printed Circuit Design*. Updated: 2025-07-18. May 23, 2017. URL: https://resources.altium.com/p/everything-you-need-know-about-microvias-printed-circuit-design.

[21] ALLPCB. *Through-Hole Via Filling and Plugging: When and Why?* June 2025. URL: https://www.allpcb.com/allelectrohub/through-hole-via-filling-and-plugging-when-and-why.

[22] Stephen C Thierauf. *Understanding signal integrity.* Artech House, 2011.

[23] D.E. Bockelman and W.R. Eisenstadt. "Combined differential and common-mode scattering parameters: theory and simulation". In: *IEEE Transactions on Microwave Theory and Techniques* 43.7 (1995), pp. 1530–1539. DOI: 10.1109/22.392911.

[24] Eric Bogatin. *Signal and Power Integrity: Simplified.* 2nd ed. Prentice Hall, 2010.

[25] Mario Pérez-Escribano and Enrique Márquez-Segura. "Performance Evaluation of Broadband Characterization of Coupled Transmission Lines Even- and Odd-Mode Propagation Constants Using Differential and Common Mode S-Parameters". In: *IEEE Journal of Microwaves* 3.2 (2023), pp. 676–686. DOI: 10.1109/JMW.2022.3232306.

[26] James R. Andrews. "Time Domain Reflectometry". In: *Symposium and Workshop on Time Domain Reflectometry in Environmental, Infrastructure, and Mining Applications.* USBM Special Publication SP 19-94. Available online. Washington, DC: U.S. Bureau of Mines, 1994, pp. 4–13. URL: https://pe2bz.philpem.me.uk/Comm01/-%20TestEquip/-%20TDR/Info-907-Theory/P2/pico.html (visited on 06/03/2026).

[27] Huibin Zhu, Allen R Hefner, and J-S Lai. "Characterization of power electronics system interconnect parasitics using time domain reflectometry". In: *IEEE Transactions on Power Electronics* 14.4 (1999), pp. 622–628.

[28] Mike Resso and Eric Bogatin. *Signal integrity characterization techniques.* Intl. Engineering Consortiu, 2009.

[29] Christoph Mittermayer and Andreas Steininger. "On the determination of dynamic errors for rise time measurement with an oscilloscope". In: *IEEE Transactions on Instrumentation and Measurement* 48.6 (1999), pp. 1103–1107.

[30] TDA Systems, Inc. *TDR Test.* Application note, originally published in *Printed Circuit Design Magazine*, April 2002. Available from Tektronix. Accessed: 2026-06-03. 2002. URL: https://www.tek.com/en/documents/primer/tdr-test.

[31] Guillermo Gonzalez. *Microwave Transistor Amplifiers: Analysis and Design.* 2nd ed. Upper Saddle River, NJ: Prentice Hall, 1997.

[32] Ansys. *Maximum Delta S*. Accessed: 2026-05-28. 2024. URL: https://ansyshelp.ansys.com/public/Views/Secured/Electronics/v242/en/Subsystems/HFSS/Content/HFSS/MaximumDeltaS.htm.

[33] Ansys. *Setting the Maximum Delta S Per Pass*. Accessed: 2026-05-28. 2025. URL: https://ansyshelp.ansys.com/public/Views/Secured/Electronics/v251/en/Subsystems/HFSS/Content/HFSS/SettingtheMaximumDeltaSPerPass.htm.

[34] Peng Zhou et al. "Impact of Anti-resonance Caused by Via Structure on Signal Integrity in High-Speed Circuits". In: *2019 IEEE 3rd Advanced Information Management, Communicates, Electronic and Automation Control Conference (IMCEC)*. 2019, pp. 867–871. DOI: 10.1109/IMCEC46724.2019.8984048.

[35] Ansys, Inc. *HFSS Setup: Advanced Meshing Tab*. https://ansyshelp.ansys.com/public/Views/Secured/Electronics/v251/en/Subsystems/HFSS/Content/3DLayout/HFSSSetupAdvancedMeshingTab.htm. Ansys Electromagnetics Suite 2025 R1, accessed: 2026-05-31. 2025.

[36] Zachariah Peterson. *PCB and Package Design for 224G PAM-4 Channels*. Altium Resources. Created: July 3, 2023; Updated: August 27, 2025. 2023. URL: https://resources.altium.com/p/pcb-and-package-design-224g-pam-4-channels.

[37] Leon Bruckman et al. *224G Electrical Link Bandwidth Considerations*. IEEE 802.3df Task Force, July 2022 Plenary. July 2022. URL: https://www.ieee802.org/3/df/public/22_07/bruckman_3df_01a_2207.pdf.

[38] Signal Integrity Journal. *How to Stop Your Differential Vias from Leaking*. Accessed: 2026-05-22. 2020. URL: https://www.signalintegrityjournal.com/articles/1918-how-to-stop-your-differential-vias-from-leaking.

[39] Yan Ning, Michael H Azarian, and Michael Pecht. "Effects of voiding on thermomechanical reliability of copper-filled microvias: Modeling and simulation". In: *IEEE Transactions on Device and Materials Reliability* 15.4 (2015), pp. 500–510.

Printed by Tryckeriet i E-huset, Lund 2025

Series of Master's theses
Department of Electrical and Information Technology
LU/LTH-EIT 2026-1164
http://www.eit.lth.se